Ion-trap cavity QED system for probabilistic entanglement

Nicolas R. Seymour-Smith

Submitted for the degree of Doctor of Philosophy
University of Sussex
September 2011

Declaration

I hereby declare that this thesis has not been and will not be submitted in whole or in part to another University for the award of any other degree.

Signature:

Nicolas R. Seymour-smith

UNIVERSITY OF SUSSEX

Nicolas R. Seymour-Smith, Doctor of Philosophy

Ion-trap cavity QED system for probabilistic entanglement

Summary

Laser systems and a linear radiofrequency (rf) Paul trap with an integrated co-axial cavity have been developed for experiments in cavity QED and probabilistic entanglement.

Single $^{40}Ca^{+}$ ions and large Coulomb crystals have been trapped routinely and laser cooled with long trapping lifetimes. A technique to achieve precise overlap of the pseudopotential minimum of the rf-field with the cavity mode has been implemented through variable capacitors in the resonant rf-circuit used to drive the trap. Three-dimensional micromotion compensation has been implemented.

An 894 nm laser has been frequency stabilised to a Pound-Drever-Hall cavity which is in turn stabilised to atomic Cs using polarisation spectroscopy. The Allan variance of the error signal has been reduced to less than a kilohertz on timescales greater than a second. A novel implementation of the scanning cavity transfer lock has been developed to transfer the stability of the 894 nm laser to the 397 nm ion cooling and 866 nm repumping lasers. The bandwidth of the system has been increased to 380 Hz and the Allan variance of the error signal has been reduced to less than ten kilohertz on timescales of greater than a second.

The pseudopotential minimum of the rf field has been overlapped optimally with the optical cavity mode through mapping of the fluorescence from cavity-field repumped ions as a function of their displacement. Coupling to the cavity mode has been confirmed by observation of resonant fluorescence into the cavity mode using the cavity-assisted Raman transition process.

The thesis demonstrates that the setup is ready for the controlled production of single photons with pre-determined polarisation states, and progression onto new schemes to entangle multiple ions that are coupled to the optical cavity mode.

Acknowledgements

This thesis is based on my work, accomplished during the last four years in the Ion-Trap Cavity QED (ITCQ) group at the Department of Physics and Astronomy in the University of Sussex, under the supervision of Dr. Matthias Keller and Prof. Wolfgang Lange.

The work presented could not have been possible without the collaborative work of former and present group members of ITCQ and the technical staff at the University of Sussex.

To begin with, three senior Postdocs that were active on the project during my research period deserve special thanks. Dr. Peter Blythe and Dr. Anders Mortensen, who were working in the group when I first started, freely provided guidance and support throughout their stay in the group. The work done on the atomic reference presented in this thesis was first implemented by Peter Blythe, before it was modified and characterised by me. Peter was also responsible for trapping with the very first iteration of this trap design, (which was designed by Matthias Keller), and thus credit goes to him for narrowing down the wavelength ranges needed for trapping, and programming much of the original computer interface for the trap systems. Dr. Dan Crick worked extensively with me on the project throughout my third year, contributing significantly to the design of the optical cavity mounts, feedback electronics and computer interfaces used in the project. Dan was also a never-ending source of new ideas and discussion.

To the rest of the Postdocs, graduate students and undergraduate students in the group I wish to extend my thanks for discussions and assistance. They are: Lizzie Brama, Andrew Riley-Watson, Kevin Sheridan (of the molecular ion trapping group), Alex Wilson, Hiroki Takahashi, Fedja Orucevic, Valentina Ruseva, Jennifer Hide, Kari Härkönen and Carlos Delgado.

An extremely important contribution to the work presented in this thesis has been made by the technical staff at the university. The expertise and dilligence of Alan Butler, John Knight and Alan Meyers in particular have made much of the work accomplished possible.

Most importantly I would like to extend my gratitude to my supervisors, Matthias Keller and Wolfgang Lange, for their help and guidance at every stage of the project, their never-ending enthusiasm, and their invaluable contributions to my development as a graduate researcher.

Finally my thanks go out to my friends (including everyone mentioned above) and family for personal support during my studies.

Dedicated to the memory of Professor Wolfgang Lange
12 April 1962 - 3 April 2012

Professor Lange's influence on this work and my development can not be measured. His exceptional skill, his unquenchable thirst for understanding, his refined appreciation of the arts, and the levity and good humour with which he went about his work made every encounter with him a pleasant and valuable adventure, of which I was privileged and honoured to take part. I hope to be able to take just some of his incredible character with me through my life.

Contents

List of Tables

List of Figures

Chapter 1

Introduction

A major challenge in quantum physics is to manipulate and fully control individual quantum systems at the single quantum level and combine them into larger systems of increased complexity. These systems allow us to investigate fundamental quantum phenomena such as superposition, entanglement and coherence. Although quantum mechanical theories have been used to describe observed natural phenomena since the early parts of the 20^{th} century, the technologies needed to manipulate single quantum systems have become available only recently.

This development has opened up many new fields of physics. The field of quantum information processing (QIP) is one such field that has been the subject of much interest in the last decade. The ultimate goal of this field being to exploit the properties of quantum mechanics for communication and computation purposes and tackle problems that are difficult, or impossible, to solve classically.

Currently, one of the most succesful approaches to implement quantum systems for computation are ions trapped in radiofrequency traps. The unparalleled control over their motion, localisation and their internal states makes them ideal quantum bits (qubits). In these systems, the entanglement of multiple ions has been demonstrated [1, 2, 3, 4, 5, 6], quantum gates have been implemented [7, 8] and quantum error correction [9, 10] has been shown.

Recent proposals for QIP require the capability to deterministcally address, manipulate and couple individual components of a quantum network [11]. A quantum network combines some form of stationary quantum register (e.g. ions) with non-stationary, or 'flying' quantum bits (qubits) for communication between systems, typically photons. Combin-

ing an ion trap with an optical cavity is currently considered one of the best systems to accomplish this.

This thesis is concerned with the manipulation and interaction of these two fundamentally quantum mechanical objects: ions and the quantised field inside a cavity. Individual trapped ions in an ion-trap and cavity system can provide the stationary qubits of a quantum network, using the ions' internal states for information storage. The interfacing to a flying qubit can be addressed through cavity quantum electrodynamics (CQED) i.e. the interaction between matter (the ions) and the cavity field. I present a specific design of a linear Paul trap for trapping ions within the mode of a co-linear high-Q optical cavity. The system can be used for investigations of entanglement between multiple ions trapped inside the cavity mode, and can be interfaced to other quantum nodes in a network.

One of the major challenges in the field of experimental CQED is to reach a regime where the coherent interaction between the matter and light systems is faster than the dissipative processes. For a two-level atom or ion in a cavity field this is known as the strong coupling regime. It is reached when the rate of coherent exchange of excitations between the ion and cavity g exceeds both the atomic spontaneous emission rate Γ, and the cavity field decay rate κ. The strong coupling regime has been realised with atoms in microwave and optical cavities. Many of the first CQED experiments, single-photon sources, were based on atoms interacting with a high-Q optical cavity in the strong coupling regime [12, 13]. However, precise localisation of atoms is difficult, and trapping times are limited due to their weak interactions with electric and magnetic fields. Ions, however, interact strongly with electric fields and can be easily trapped and well localised for very long periods.

In the latter experiments, ultra-high finesse cavities with very small mode-volumes are required to achieve strong coupling with the neutral atoms. With ions however, the presence of the mirror surfaces near the trapping region presents a significant challenge to obtaining sufficiently small cavity mode-volumes, due to perturbations of the radio-frequency trapping field caused by the presence of the dielectric mirrors. Thus, the strong coupling regime has not yet been realised for single-ion interactions.

A linear Paul trap with large co-linear cavity has been used in Aarhus to couple an ensemble of $N = 500$ identical ions to the cavity mode [14]. This has enabled them to realise the *collective* strong coupling regime, where the collective coupling g_N, which

scales as $\sqrt{N}$, exceeds the dissipative rates of the system. This allows the ensemble to be used as an interfaceable quantum light memory, in which a photon can be stored for later extraction.

In contrast to this approach, we are interested in the coupling to small numbers of ions, so that they can be individually addressed and brought into an entangled state for QIP. We have developed a co-linear trap design to avoid perturbations of the trapping field by shielding the trapping region from the mirrors using the dc-endcap electrodes. However, with the mirrors resting behind the dc-endcap electrodes, the cavity mode-volume is relatively large, and the strong coupling regime remains difficult to realise.

However, we can work around the problem of weak coupling by using probabilistic or "heralded" entanglement of ion pairs in the same cavity mode. The process is also known as measurement-based entanglement [15]. The ions are projected into an entangled state by coincident detection of orthogonally polarised photons emitted into the cavity. The entanglement can be measured by individually addressing the ions with pulses designed to rotate the population between the qubit states, and then measuring the correlation of the populations between the two ions.

Creating entangled states in such a simple way is an important technology for quantum information processing. The method is not limited to the pairwise entanglement of ions. If two ions, each of which is a partner of a separate entangled pair of ions, are subjected to a Raman pulse generating a photon polarisation-entangled to the electronic state of the ion, subsequent measurement of two orthogonally polarised photons "fuses" the entangled pairs together [16]. In this way a highly entangled state of 4 ions is created, a so-called cluster state. The method can be applied repeatedly, generating cluster states of size 4, 8, 16, etc. Cluster states are a valuable resource for quantum information processing. They are the basis of one-way quantum computation [17]: Once the initial highly entangled state is generated, computation proceeds by sequential measurement of the qubits in different bases, chosen according to the results of previous measurements. The experiments described in this thesis provide a foundation for the generation of highly entangled cluster states in an ion-cavity system.

The thesis is structured into six major chapters. This first chapter introduces the theoretical background for the basic technologies used in the experiment, ion trapping, Doppler cooling and the manipulation of the ion and cavity's quantum states. Chapter two

presents the linear Paul trap used for the experiment, and the optics used for manipulating trapped $^{40}Ca^{+}$. The coherent control of quantum states of calcium ions requires a large number of laser systems. Chapters three and four present the work done to stabilise these lasers to the accuracy required. Chapter five discusses the properties of the optical cavity that was set up for the experiment and presents measurements of the cavity-ion interaction that was succesfully established in the system. Chapter six presents a summary and outlook for the next stages of the experiment's development.

Chapter 2

Theory

2.1 Linear Paul Trap

The linear Paul trap is a device designed to confine charged particles with radiofrequency (rf) electric fields. The design is derived from the quadrupole mass filter invented by Wolfgang Paul in the 1950s. In contrast to the hyperbolic Paul trap, rf confinement is only necessary in two dimensions, and confinement in the axis of the trap is created by endcap electrodes using a static (dc) potential.

The trap design used in this thesis is shown in Fig. 2.1. It consists of four blade-shaped electrodes arranged with their pointed edges on a square centred on the trapping region. These electrodes carry the rf potential used to trap particles in the radial direction. At either end of the linear trap are endcap electrodes that carry the dc potentials used to trap the particles in the axial direction.

2.1.1 Basic trapping theory

Charged particles are trapped in the device by their interaction with the electric fields generated by the trapping structure. Earnshaw's theorem states that it is not possible to confine a charged particle in three dimensions using only a static potential. Instead an alternating rf potential is used for trapping in two dimensions whilst the third is taken care of by a dc potential.

The rf potentials applied to the rf electrodes can be written as $U(t) = U_{\mathrm{rf}} \cos(\Omega_{\mathrm{rf}} \cdot t)$, where U_{rf} is the peak-to-peak voltage of the rf potential and Ω_{rf} is its angular frequency. This potential is applied to two opposite electrodes, whereas the negative of this potential

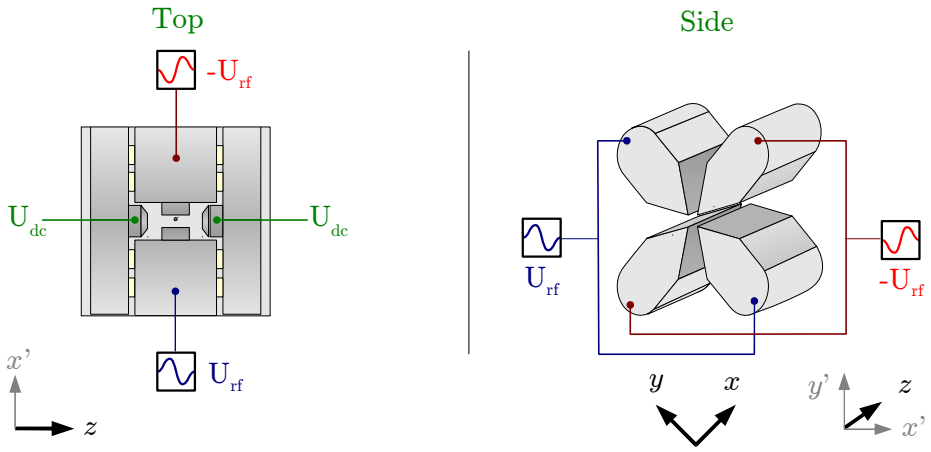

Figure 2.1: Linear Paul trap electrode configuration. Voltage $U_{\rm dc}$ is applied to both endcaps for axial confinement (shown in left diagram). Voltage $\pm U_{\rm rf}$ is applied to the rf-electrodes for radial confinement (shown in left and right diagrams). x, y and z vectors shown make up the principle axes of the trap, while x' and y' are the natural axes defining the horizontal ($y' = 0$) and vertical ($x' = 0$) planes. The radial centre-point of the four electrodes is commonly referred to as the trap axis.

$(-U(t))$ is applied to the other pair.

For parabolic-shaped trap electrodes, the radial trapping potential generated by the rf electrodes is given by $U(x,y) = -\frac{1}{2}U_{\rm rf}\cos(\Omega_{\rm rf}\cdot t)\left[\frac{x^2-y^2}{r_0^2}\right]$. The total electric potential, including contribution from the dc electrodes, is

$$\phi(x,y,t) = -\frac{1}{2}U_{\rm rf}\cos(\Omega_{\rm rf}\cdot t)\left[\frac{x^2-y^2}{r_0^2}\right] - \frac{1}{2}\eta U_{\rm dc}\left[\frac{x^2+y^2}{z_0^2}\right], \tag{2.1}$$

where $2z_0$ is the distance between the endcaps, r_0 is the distance from ion to electrode, and η is a geometric factor related to the shape of the dc electrodes and the amount of electromagnetic shielding from the rf electrodes. In the axial direction the trapping potential is $\phi(z) = \eta U_{\rm dc}\frac{z^2}{z_0^2}$.

From these equations we can derive the equation of motion of a particle of charge Q and mass m inside the trapping potential. In the x-direction

$$\ddot{x} + \frac{Q}{m}\frac{\partial\phi(x,y,t)}{\partial x} = 0, \tag{2.2}$$

substituting $\tau = \frac{\Omega_{\rm rf}t}{2}$, gives

$$\frac{d^2x}{d\tau^2} + \frac{4Q}{m\Omega_{\rm rf}^2}\frac{\partial\phi(x,y,\tau)}{\partial x} = 0, \tag{2.3}$$

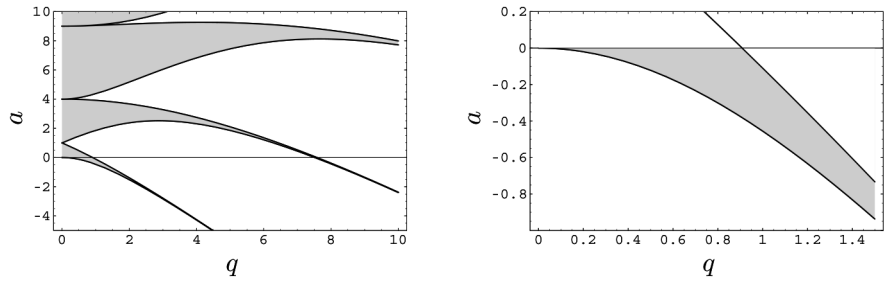

Figure 2.2: Mathieu function stability regions in q and a, marked in grey. Right is the region of stability for a particle in the linear Paul trap.

and with

$$q = \frac{2QU_{\mathrm{rf}}}{m\Omega_{\mathrm{rf}}^2 r_0^2}, \tag{2.4}$$

$$a = \frac{-4\eta QU_{\mathrm{dc}}}{m\Omega_{\mathrm{rf}}^2 z_0^2}, \tag{2.5}$$

we find

$$\frac{d^2x}{d\tau^2} + (a - 2q\cos 2\tau)x = 0. \tag{2.6}$$

Similarly for the y-direction:

$$\frac{d^2y}{d\tau^2} + (a + 2q\cos 2\tau)y = 0. \tag{2.7}$$

Equations 2.6 and 2.7 are Mathieu equations with known stable solutions. The stability range for small values of q and a is shown in Fig. 2.2 [18]. These regions correspond to values of q and a where the particle is stably trapped in the radial direction. For small q and small excursions of the particle from the trap centre, the solution can be approximated by

$$x(t) = x_0(1 - q\cos\Omega_{rf}t)\cos\omega_r t, \tag{2.8}$$

$$y(t) = y_0(1 - q\cos\Omega_{rf}t)\cos\omega_r t, \tag{2.9}$$

where ω_r is known as the radial secular frequency

$$\omega_{\mathrm{r}} = \frac{\sqrt{q^2/2 + a}}{2}\Omega_{\mathrm{rf}}. \tag{2.10}$$

Equations 2.9 and 2.8 describe the radial motion at two distinct frequencies. One fast frequency Ω_{rf}, driven directly by the rf drive, known as the micromotion, and one much slower frequency ω_{r} known as the secular motion, with amplitude x_0, y_0, associated with the time-averaged radial trapping potential.

In the axial direction, the trapping potential is given by

$$\phi(z) = \eta U_{\mathrm{dc}} \frac{z^2}{z_0^2}, \tag{2.11}$$

Which leads to an equation of motion for the z-direction

$$\ddot{z} + \frac{a}{2}\Omega_{\mathrm{rf}}^2 z = 0, \tag{2.12}$$

with the solution

$$z(t) = z_0 \cos(\omega_{\mathrm{z}} t), \tag{2.13}$$

$$\omega_{\mathrm{z}} = \sqrt{\frac{-a}{2}}\Omega_{\mathrm{rf}}, \tag{2.14}$$

describing a simple-harmonic motion in the z-direction with frequency ω_{z}.

If we average out the fast micromotion in the radial direction we can construct a 'pseudopotential' equation describing the motion of the charged particle in three dimensions:

$$\Phi(r, z) = \frac{1}{2} m(\omega_{\mathrm{r}}^2 r^2 + \omega_{\mathrm{z}}^2 z^2),\ r^2 = x^2 + y^2, \tag{2.15}$$

which we can immediately identify as a three-dimensional simple harmonic potential well, with frequencies ω_{r} for x and y directions and ω_{z} for the z direction.

The trap depth of the system is defined as the height of the potential barrier provided by the rf and dc trapping fields. For typical trapping parameters, finite-element modelling simulations give a depth of $\sim$9 eV.

2.2 Doppler laser cooling

Ions created inside the linear Paul trap will be trapped as long as they have less kinetic energy than the trap depth. In order to localise ions and minimise the variation in coupling between ions and the experimental optical cavity, the ions must be significantly cooler.

For this purpose, we use the Doppler cooling technique. Doppler cooling is based on absorption and emission of photons by an ion in a laser field, and the Doppler shift of the resonance frequency of the ion as it moves through that laser field.

In order to understand the principle of laser cooling we must first characterise the interaction between an atom and a classical laser light field.

We start with the Hamiltonian of a two-level system, with an excited state $|b\rangle$ and energy $\hbar\omega_b$, and a ground state $|a\rangle$ with energy $\hbar\omega_a$. The Hamiltonian of the free system is

$$H_0 = \hbar\omega_a|a\rangle\langle a| + \hbar\omega_b|b\rangle\langle b|. \tag{2.16}$$

The laser interaction Hamiltonian is given by

$$H_I = -(\sigma_+ + \sigma_-)\mu_{ab}E, \tag{2.17}$$

where $\sigma_+ = |a\rangle\langle b|e^{i\omega_{ab}t}$, $\sigma_- = |b\rangle\langle a|e^{i\omega_{ab}t}$, $\omega_{ab} = \omega_b - \omega_a$, and μ_{ab} is the atomic transition dipole moment.

The electric field of the laser light is

$$E = \frac{1}{2}(e^{-i\omega t} + e^{i\omega t})E_0, \tag{2.18}$$

where $\omega = \frac{2\pi c}{\lambda}$ for wavelength λ of the laser. We define the 'Rabi frequency' Ω of the system as $\Omega = \mu_{ab}E_0/\hbar$. This gives

$$H_I = -\frac{\hbar}{2}(\sigma_+ + \sigma_-)(e^{-i\omega t} + e^{i\omega t})\Omega, \tag{2.19}$$

or under the rotating wave approximation,

$$H_I = -\frac{\hbar\Omega}{2}(\sigma_+ e^{-i\Delta t} + \sigma_- e^{i\Delta t}), \tag{2.20}$$

where $\Delta = \omega - \omega_{ab}$ and $\omega_{ab} = \omega_a - \omega_b$. The total Hamiltonian H is

$$H = H_0 + H_I. \tag{2.21}$$

To include the effect of spontaneous emission, the system can be described by the density matrix. The time evolution is then given by the master equation

$$\frac{d}{dt}\rho = \frac{1}{i\hbar}[H,\rho] + \Lambda\rho, \tag{2.22}$$

$$\Lambda\rho = -\frac{\Gamma}{2}[\sigma_+\sigma_-\rho - 2\sigma_-\rho\sigma_+ + \rho\sigma_+\sigma_-], \tag{2.23}$$

where $\Gamma = \omega_{ab}^3\mu_{ab}^2/\pi\epsilon_0\hbar c^3$ is the spontaneous decay rate. From this expression the time evolution of the individual elements of the density matrix are

$$\begin{aligned}
\frac{d}{dt}\rho_{aa} &= \Gamma\rho_{bb} - \frac{i\Omega}{2}(\tilde{\rho}_{ba} - \tilde{\rho}_{ab}), \\
\frac{d}{dt}\rho_{bb} &= -\Gamma\rho_{bb} + \frac{i\Omega}{2}(\tilde{\rho}_{ba} - \tilde{\rho}_{ab}), \\
\frac{d}{dt}\tilde{\rho}_{ab} &= \left(i\delta - \frac{\Gamma}{2}\right)\tilde{\rho}_{ab} + \frac{i\Omega}{2}(\rho_{bb} - \rho_{aa}),
\end{aligned} \tag{2.24}$$

where $\tilde{\rho}_{ab} = e^{i\omega t}\rho_{ab}$ and $\delta = \omega - \omega_{ab}$. These equations are known as the optical Bloch equations for a two-level atom, and they describe fully the interaction between a laser and an atom with spontaneous decay.

The steady state solution to these equations gives an upper state population of [19]

$$\rho_{bb} = \frac{s_0/2}{1 + s_0 + (2\delta/\Gamma)^2}, \tag{2.25}$$

with $s_0 = 2\Omega^2/\Gamma^2$, known as the on-resonance saturation parameter.

From the above equations we can calculate the force generated by a laser with wave-vector $\vec{k}$ and angular frequency $\omega_l = (\omega_{ab} + \delta)$, impinging on an atom.

When a photon from the laser is absorbed by the atom, the atom obtains a momentum kick of $\vec{p} = \hbar\vec{k}$. Photons subsequently emitted by the atom through stimulated emission return that momentum to the laser mode and leave the atom with zero net momentum transfer. Spontaneously emitted photons, however, are emitted isotropically so that if we average over many cycles their total momentum transfer is zero, and the net transfer of the process is in the direction $\hat{k}$ of the resonant laser beam.

In this model we can say that every spontaneous decay event transfers on average the momentum of a single photon from the laser field to the atom. The rate of momentum transfer can then be determined by the steady-state population of the excited state and

the rate of spontaneous decay. This is known as the 'scattering rate' γ:

$$\gamma = \Gamma \rho_{aa}. \tag{2.26}$$

The force felt by the atom from the laser is given by the momentum transfer per photon and γ

$$\vec{F} = \frac{d\vec{p}}{dt} = \hbar\vec{k} \cdot \gamma, \tag{2.27}$$

where $\hbar\vec{k}$ is the momentum of a single photon. Using Eqn. 2.25 this can be written as

$$\vec{F} = \hbar\vec{k} \cdot \frac{s_0\Gamma/2}{1 + s_0 + (2\delta/\Gamma)^2}. \tag{2.28}$$

Now we take into account the Doppler shift of the laser, with frequency ω_l seen by an atom moving with velocity $v_k = \vec{v} \cdot \hat{k}$ in the direction of the laser. The Doppler shifted frequency ω is

$$\omega = \left(1 + \frac{v_k}{c}\right)\omega_l, \tag{2.29}$$

or in terms of δ

$$\delta \to \delta + |\vec{k}|v_k. \tag{2.30}$$

Substituting this into equation 2.28 yields

$$\vec{F}(v_k) = \hbar\vec{k} \cdot \frac{s_0\Gamma/2}{1 + s_0 + \left(\frac{2(\delta + |\vec{k}|v_k)}{\Gamma}\right)^2}. \tag{2.31}$$

For small velocity the force can be approximated by a Taylor expansion around $v_k = 0$

$$\vec{F}(v_k) = \vec{F_0} + \vec{\beta}v_k, \tag{2.32}$$

$$\vec{F_0} = \frac{\hbar\vec{k}s_0\Gamma/2}{1 + s_0 + (\frac{2\delta}{\Gamma})^2}, \tag{2.33}$$

$$\vec{\beta} = -\frac{4\hbar|\vec{k}|\delta}{\Gamma} \cdot \frac{s_0\vec{k}}{\left(1 + s_0 + (\frac{2\delta}{\Gamma})^2\right)^2}. \tag{2.34}$$

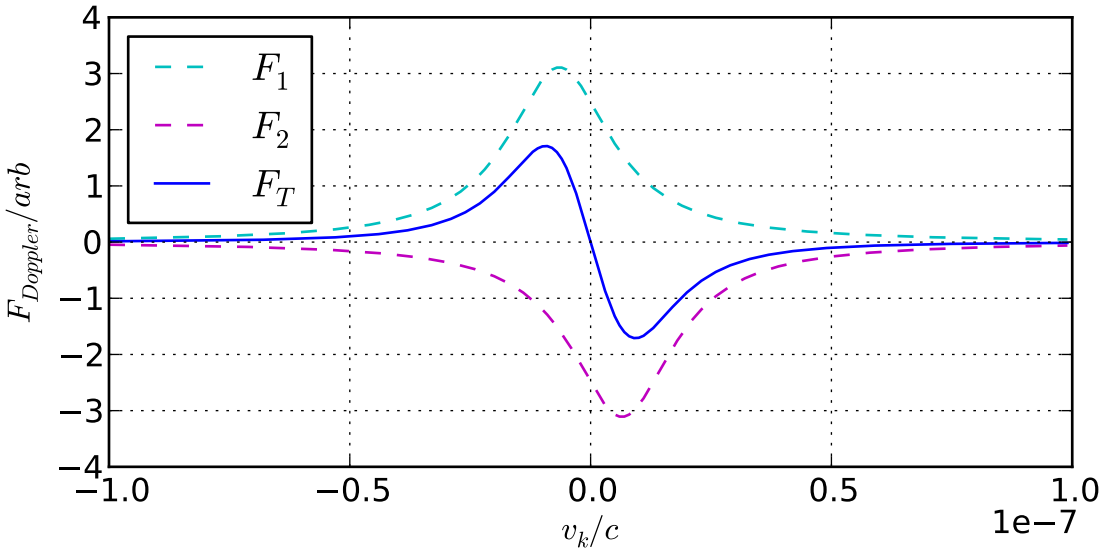

Figure 2.3: Doppler cooling force profile F_T for counter-propagating beams with contributions F_1 and F_2.

That is, for small v_k the laser contributes two components of force: a constant force $\vec{F_0}$ that acts even whilst the atom is still, and a velocity dependent component $\vec{\beta}v_k$. Since $\vec{\beta}$ is anti-parallel with $\vec{v}$ and linear with v_k, this component acts as a viscous damping force that cools motion of the atom in the direction of the laser's propagation.

The constant component $\vec{F_0}$ is the radiation pressure and is typically balanced out by a second, counter-propagating laser which also provides cooling power in the opposite direction. The combined cooling force $\vec{F_T}$ for counter-propagating beam forces $\vec{F_1}$ and $\vec{F_2}$ (with direction $\hat{k}$ and $-\hat{k}$ respectively) and $\delta < 0$ (i.e. red-detuned laser) is shown in Fig. 2.3.

The total slope of the force around $v_k = 0$ has magnitude $2|\vec{\beta}|$. The total cooling power (or cooling rate) is given by $P_c = \langle \vec{F_T} \cdot \vec{v} \rangle = 2|\vec{\beta}|\langle v_k^2 \rangle$. It can be shown from equation 2.34 that $\vec{\beta}$ and therefore $\vec{F_T}$ is maximised for laser detuning $\delta = \pm\Gamma/2$. We require however that the force is damping, and so $\delta = -\Gamma/2$ is used.

In order to work out the theoretical temperature limit of Doppler cooling we must look again at the spontaneously emitted photons. Because the photons are emitted isotropically, over a number of cycles the net momentum transfer from these processes is zero. However the momentum transfer per individual photon is finite and each emission creates a heating effect by the recoil it produces. The kinetic energy each photon imparts to the atom is $(\hbar k)^2/2m$, at a rate of γ per laser, giving a total heating rate of $P_H = \gamma(\hbar k)^2/m$.

For these expressions of P_c and P_H we find the average kinetic energy of the ion in equilibrium is $E_k = \hbar\Gamma/8$. Defining the temperature according to this energy we find a lower temperature limit T_{lim}:

$$T_{lim} = \frac{\hbar\Gamma}{8k_B}. \tag{2.35}$$

For trapping a neutral atom in free space we would need a pair of lasers for each direction, for a total of six. In contrast to this, in an ion trap it is possible to direct a single cooling laser such that the cooling direction has a component in all of the principal axes of motion of the ion, effectively cooling motion in all three dimensions at once. A counter propagating laser is not needed either, as the ion changes direction after every half-cycle of its harmonic motion in the trapping potential.

2.3 Cavity QED

Individual trapped ions in an ion-trap and cavity system can provide the stationary qubits of a quantum network, using the ions' internal states for information storage. The interfacing to a flying qubit can be addressed through cavity quantum electrodynamics (CQED) i.e. the interaction between matter (the ions) and the cavity field. Since optical cavities are an essential part of every stage of this experiment, a brief introduction to their properties is given, followed by a short description of cavity-atom interactions and the schemes required to generate entanglement between ions.

2.3.1 Fabry-Pérot cavities

The basic configuration of a Fabry-Pérot optical cavity is shown in Fig. 2.4. It consists of two highly reflective mirrors with radius of curvature R, placed a distance l apart from each other.

The mirrors of the optical cavity provide boundary conditions to an electromagnetic field within the mirrors, such that only specific field resonances or *modes* can build up inside it. In most cavity types, the spatial configurations of these resonant modes are Hermite-Gaussian modes. The spatial distribution of the E-field of these modes is

$$E_{nm}(r,z) = E_0\Psi_n(x,z)\Psi_m(y,z)\Phi(x,y,z), \tag{2.36}$$

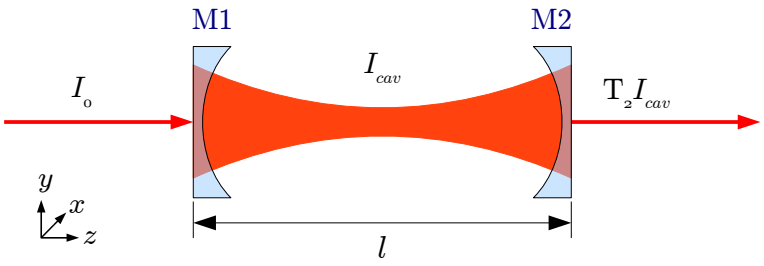

Figure 2.4: Dynamics of a Fabry-Pérot cavity resonator formed by mirrors M1 and M2 with transmissivities T_1 and T_2, and absorption losses A_1 and A_2. The mirrors have radius of curvature r. The resonant input intensity I_0 is coupled through M1 and I_{cav} is the steady state intracavity intensity.

with the amplitude of the electric field E_0. The distribution is decomposed into two transverse functions, $\Psi_n(x,z)$ and $\Psi_m(y,z)$, and a longitudinal function, $\Phi(x,y,z)$. The Transverse ElectroMagnetic modes (TEM) of the cavity are denoted as TEM_{nm}, and defined by the transverse functions above, given non-negative indices n and m. The functions themselves are given by

$$\Psi_n(u,z) = \sqrt{\frac{w_0}{w(z)}} H_n\left(\frac{\sqrt{2}u}{w(z)}\right) \exp\left(-\frac{u^2}{w(z)^2}\right), \qquad (2.37)$$
$$(u = x, y),$$

where H_n is the n-th Hermite polynomial, $w(z) = w_0\sqrt{1+(\frac{z}{z_R})^2}$ is the radius of the spatial distribution, w_0 is the minimum radius or *waist* of the cavity mode and $z_R = \frac{\pi w_0}{\lambda}$ is the so-called Rayleigh range for light of wavelength λ.

The zeroth order Hermite polynomial ($H_0(x) = 1$) gives the fundamental TEM_{00} mode the form

$$\Psi_{00}(x,y,z=0) = \exp\left(-\frac{x^2+y^2}{w_0^2}\right). \qquad (2.38)$$

This mode has a cylindrically symmetric Gaussian field distribution in the radial directions, and has maximum field intensity at the centre of the cavity mode ($r^2 = x^2 + y^2 = 0$). The radial distributions of this mode and a few higher order modes are shown in Fig. 2.5.

For an electromagnetic field with frequency ν, the resonance condition of a stable cavity mode is that the phase gained by the light field as it traverses one round trip of the cavity must be an integer multiple of 2π, so that successive round-trips through the cavity interfere constructively. From this we can define the corresponding resonance condition

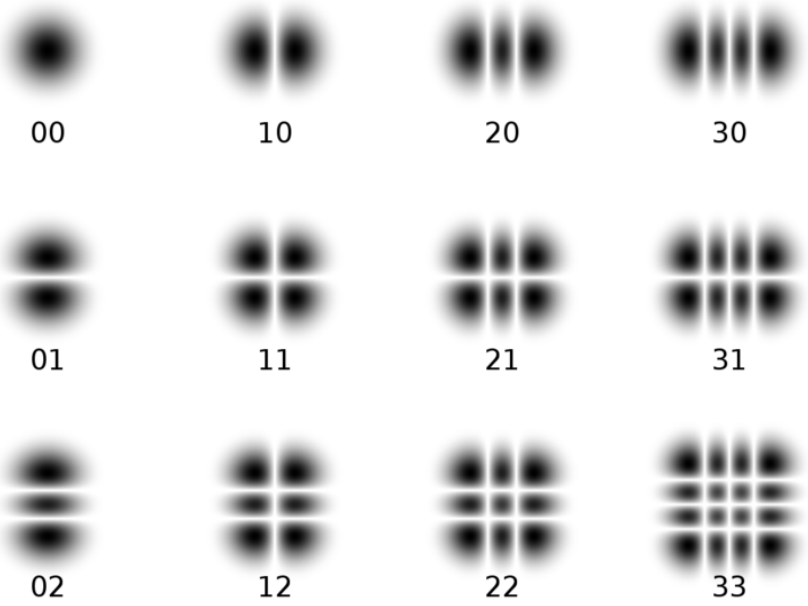

Figure 2.5: The TEM_{nm} Hermite-Gaussian modes with indices $n, m = 0, 1, 2, 3$. Cc-by-sa-3.0,2.5,2.0,1.0, http://en.wikipedia.org/wiki/File:Hermite-gaussian.png

$\nu = \nu_{nmq}$ for a mode characterised by the transverse mode indices n and m and an axial mode number q, which is a positive integer [20]

$$\nu_{nmq}/\nu_{\mathrm{FSR}} = (q+1) + \frac{1}{\pi}(m+n+1)\arccos(1-l/r), \tag{2.39}$$

where r is the radius of curvature of the mirrors and ν_{FSR} is the Free Spectral Range (FSR) of the cavity. The FSR corresponds to the frequency spacing of axial mode resonances, given by $\nu_{\mathrm{FSR}} = \frac{c}{2l}$.This is identified with the inverse cavity-round-trip time for the field, $1/\tau$.

A special case worth noting is the confocal condition, where $l = r$. Under this condition we can see that transverse modes with either odd or even $k = m+n$ have degenerate resonance frequencies, and odd k mode-frequencies are separated from even k mode-frequencies by $\frac{\nu_{\mathrm{FSR}}}{2}$.

2.3.2 Atoms interacting with a cavity field

When the electric field inside the cavity is quantised, the Hamiltonian resembles that of a quantum harmonic oscillator. Generally, the cavity state vector is a superposition of the number states $|n\rangle$, and for n photons in the mode the total energy is $\hbar\omega_c(n+\frac{1}{2})$. Photon

creation and annihilation operators, $\hat{a}^\dagger$ and $\hat{a}$, are used to express the Hamiltonian of the cavity

$$H_C = \hbar\omega_c(\hat{a}^\dagger\hat{a} + \frac{1}{2}). \tag{2.40}$$

The interaction between a two-level atom and the quantised field inside the cavity can then be described by the Jaynes-Cummings Hamiltonian. For the following model we assume that the atom is coupled to the TEM_{00} Hermite-Gaussian mode of the cavity with angular resonance frequency ω_c, and that there are no losses from spontaneous emission or cavity field decay through the mirrors.

The two-level atom, with excited state $|b\rangle$ and ground state $|a\rangle$ separated by frequency ω_A, has a Hamiltonian that reads

$$H_A = \hbar\omega_A\sigma_+\sigma_-. \tag{2.41}$$

The strength of coupling of the atom to the field mode of the cavity is expressed by the atom-cavity coupling constant [21]

$$g = g_0\Psi_{00}(\mathbf{r}), \tag{2.42}$$

$$g_0 = \sqrt{(\mu_{ab}^2\omega_c)/(2\hbar\epsilon_0 V)}, \tag{2.43}$$

where μ_{ab} is the dipole matrix element of the atomic transition and V is the cavity mode volume. In a system without losses, a change in the atom's internal state must correspond to a change of the cavity photon number n. Thus the interaction Hamiltonian of the atom-cavity system is given by

$$H_{int} = -\hbar g(\sigma_+\hat{a} + \hat{a}^\dagger\sigma_-). \tag{2.44}$$

For a given number of photons in the cavity n, the states $|b, n\rangle$ and $|a, n-1\rangle$ are coupled by equation 2.44. On resonance, the population oscillates with the Rabi frequency $\Omega_C = 2g\sqrt{n+1}$ between these states, in a manner analogous to undamped Rabi oscillations of an atom interacting with a laser. Phenomenologically, the cavity field stimulates emission from an excited atom into the cavity, de-exciting the atom and increasing the photon

number by one. Following this the atom is re-excited by absorbing a photon from the cavity field, and the cycle continues. Of particular significance is that an excited atom and a cavity containing *no* photons are sufficient to begin oscillation between $|a, 0\rangle$ and $|b, 1\rangle$, due to the vacuum fluctuations. The frequency of these 'vacuum-Rabi oscillations' is given by $2g$.

2.3.3 Cavity coupling regimes

So far we have neglected losses in the system. In reality the rate of spontaneous emission into free space Γ, and the cavity field decay rate κ, both result in damping of vacuum-Rabi oscillations, and thus contribute to the atom-cavity coupling dynamics.

Two regimes are typically identified when considering the effects of these losses. Firstly the "strong-coupling regime", with $g \gg \kappa, \Gamma$. In this regime damping rates have a small effect on the coherent evolution of the system, and vacuum-Rabi oscillations can be observed. Secondly the "bad-cavity regime", with $\kappa \gg g \gg \Gamma$. In this regime cavity field decay prevents re-absorption of the photon by the atom, and this results in strong damping of the evolution of the quantum states of the system so that no vacuum-Rabi oscillations can occur. However, the bad-cavity regime can be of benefit in extracting photons from the cavity for measurement or communication between quantum devices.

For any given value of Γ, only cavity parameters distinguish these regimes: the atom-cavity coupling g, which is proportional to $V^{-1/2}$ or $l^{-3/4}$ (i.e. the dimensions of the cavity mode), and the cavity damping rate κ, which can be characterised through the cavity finesse $\mathcal{F} = \frac{\omega_{\mathrm{FSR}}}{2\kappa}$, with $\omega_{\mathrm{FSR}} = 2\pi\nu_{\mathrm{FSR}}$. The finesse corresponds to the number of round trips a photon makes in the cavity on average before it is lost by transmission through one of the mirrors, and depends solely on the reflectivity of the cavity mirrors. The cavity decay rate κ increases with $1/(\mathcal{F} \cdot l)$ and so there is a trade-off when deciding the cavity geometry for a particular coupling regime – for very small cavities only a high finesse will keep κ low enough for strong coupling.

2.3.4 Single photon generation scheme

One of the goals of this experiment is to deterministically generate a sequence of single-photon pulses with pre-determined polarisation state that propagates from the cavity output mirror. Such a sequence could be used as the bit-stream of a quantum modem,

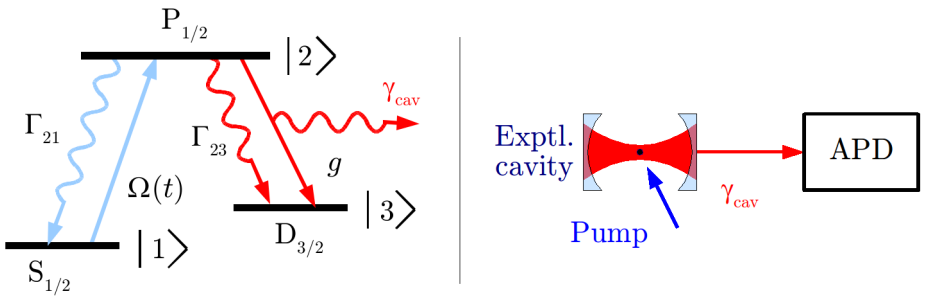

Figure 2.6: Energy level diagram for $^{40}Ca^{+}$ lambda-type system used for single photon generation. The ion interacts with a laser field $\Omega(t)$ and the quantised field g from the cavity. Photons emitted into the cavity mode can be detected by avalanche photodiodes (APDs) or photomultiplier tubes (PMTs).

used to communicate between nodes of a network, and is also an important test of the cavity-ion interaction.

The scheme required for this experiment is based on a scheme proposed by C.K. Law and H. J. Kimble in [22], originally for experiments using slow neutral atoms in transit through the optical resonator. The scheme utilises a three-level or 'lambda'-type system (Fig. 2.6) with two stable ground states ($|1\rangle$ and $|3\rangle$ in the diagram), and an excited state ($|2\rangle$). The atom is placed inside an optical cavity resonant with the transition between states $|2\rangle$ and $|3\rangle$, and addressed by a laser, resonant with the transition between states $|1\rangle$ and $|2\rangle$, with Rabi frequency $\Omega(t)$. In our experiment the lambda level structure of trapped $^{40}Ca^{+}$ is used.

If we prepare the system in state $|1\rangle$, with no photon in the cavity, then a sudden excitation process, e.g. a pulse of the laser field $\Omega(t)$ drives the system into the excited state $|2\rangle$. Subsequently a photon is emitted into the cavity mode through the atom-cavity coupling g. In the bad-cavity regime the photon escapes the cavity without interacting with the ion again. Using this scheme we can generate at most one photon because state $|3\rangle$ is assumed to be stable on the time scale of the experiment, and there is no other mechanism to recycle the population back to $|1\rangle$.

In a regime where spontaneous decay rates are large compared to g and κ, we can still maintain efficient photon generation by detuning both the laser field and cavity by frequency Δ from the atom transition ω_A. In this case the system undergoes a stimulated Raman transition between the two atomic ground states, emitting a photon into the cavity mode in the process. This process avoids putting population into the excited level and thereby reduces losses due to spontaneous emission into free space. Although the effective

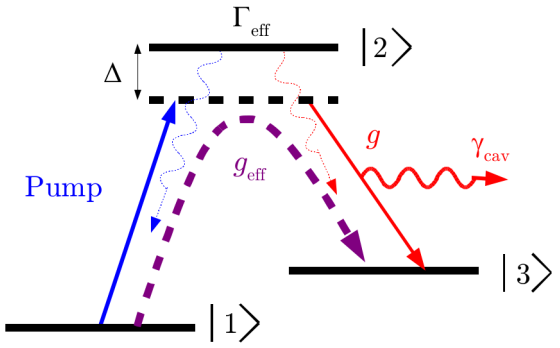

Figure 2.7: Raman transition scheme. The pump and cavity are resonantly detuned from the excited state by frequency Δ. States $|1\rangle$ and $|3\rangle$ are then directly coupled by $g_{\text{eff}} \propto 1/\Delta$. The effective rate of spontaneous decay from state $|2\rangle$, Γ_{eff} is proportional to $1/\Delta^2$.

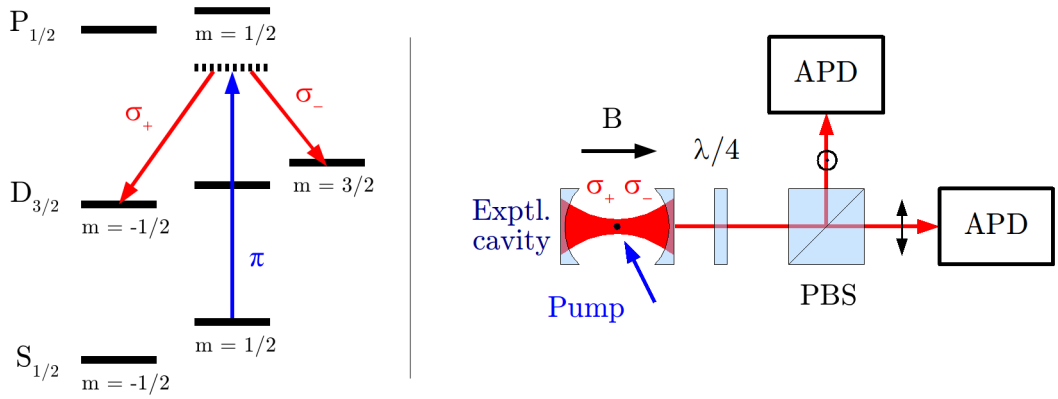

Figure 2.8: Polarised single photon generation with a strong B-field.

coupling g_{eff} between states $|1\rangle$ and $|3\rangle$ in this process is proportional to $\frac{\Omega g}{2\Delta}$, the effective decay rate from the excited state Γ_{eff} is proportional to $\frac{\Omega^2}{\Delta^2} \cdot \Gamma$, so that we still gain overall by increasing Δ. The resulting absolute decrease in g_{eff} can also be used to obtain the bad cavity regime, so that photons generated by the cavity can be extracted and interfaced with other systems. The cavity-assisted Raman transition scheme was succesfully demonstrated as a source of single photons generated from ions trapped in a transverse optical cavity by Keller et al. [23].

We can obtain selectivity of the polarisation of the emitted photon by applying a strong magnetic field in the direction of the cavity axis. This lifts the degeneracy of the Zeeman levels of the atom, and the cavity can then be tuned to drive a Raman transition between different m-levels (Fig. 2.8). Although a useful system in itself, the experiment can also be used to probe for significant birefringence in the cavity, which would need to be accounted for to determine the fidelity of heralded entanglement schemes that rely on the polarisation of detected photons (section 2.3.5).

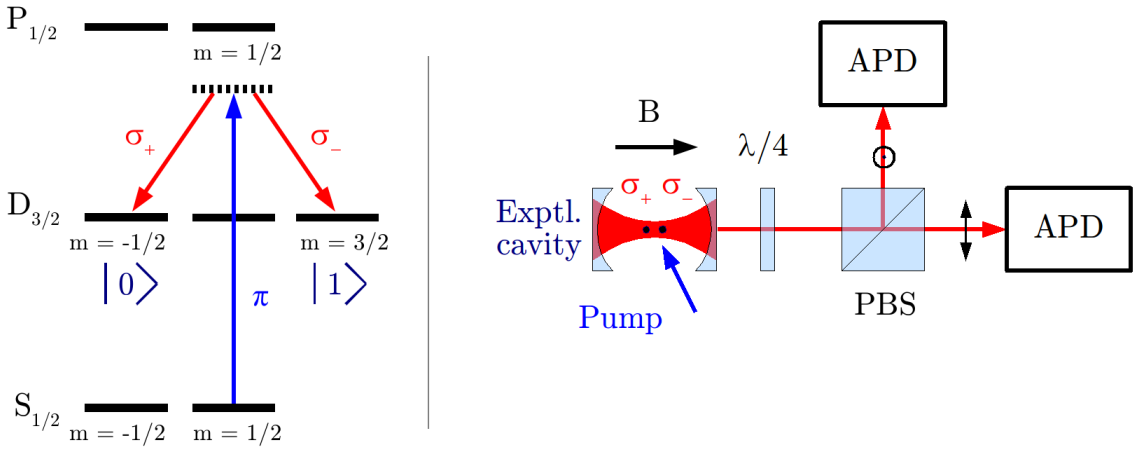

Figure 2.9: Probabilistic entanglement generation between two ions stored inside the same cavity mode, under a weak B-field

2.3.5 Probabilistic entanglement scheme

Entanglement of two fixed ion qubits coupled to a cavity in the weak coupling regime can be achieved using probabilistic entanglement. Figure 2.9 shows the relevant level structure and entanglement process. A pair of identical trapped ions undergo a cavity-assisted Raman transition from the $S_{1/2}$ to the $D_{3/2}$ state. In this process both ions are pumped by the same π-polarised laser. A small magnetic field provides the quantisation axis for definition of the emitted photon polarisation, and for definition of the internal Zeeman sub-levels of the final states, which are used as qubits. If the magnetic field is sufficiently small that the Zeeman sub-levels are not split beyond the cavity linewidth, then the ions will emit either a σ_- or σ_+ photon as they undergo a transition to either the $m = -1/2$ or $m = +3/2$ sub-level, denoted $|0\rangle$ and $|1\rangle$ in the diagram above.

The generated photons escape from the cavity mode into the photon-detector setup shown in Fig 2.9. A quarter waveplate converts the polarisation of the photons into orthogonal linear polarisations, and these channels are separated by a polariser. When photons of both polarisations are detected coincidently after a driving pulse, all that is known is that the two ions are in different states, but there is no knowledge of which ion is in which state, because all information about which ion any photon comes from is erased by the cavity. Therefore, the ions are projected into an entangled state $|0\rangle_1|1\rangle_2 + |1\rangle_1|0\rangle_2$.

Once entanglement is generated, the entanglement can be measured by individually addressing the ions with pulses designed to rotate the population between sub-levels, and then measuring the correlation of the populations between the two ions.

Chapter 3

Trap and lasers

3.1 The experimental trap

The trap used in this experiment is a linear Paul trap, with four blade-shaped stainless steel rf electrodes tapered to points on the corners of a square of side 0.66 mm. The characteristic radius r_0 of the trap is the distance from the rf centre of the trap to the electrodes and is $r_0 = 0.465$ mm. The distance between the endcaps, which provide dc confinement along the z-axis, is $2z_0 = 5$ mm.

The blade-shaped design of the rf electrodes allows for relatively small electrode spacing, thus a steeper trapping potential for the same rf-drive ($q \propto 1/r_0^2$), and improved optical access over similar sized rod-shaped or hyperbolic-shaped electrode designs.

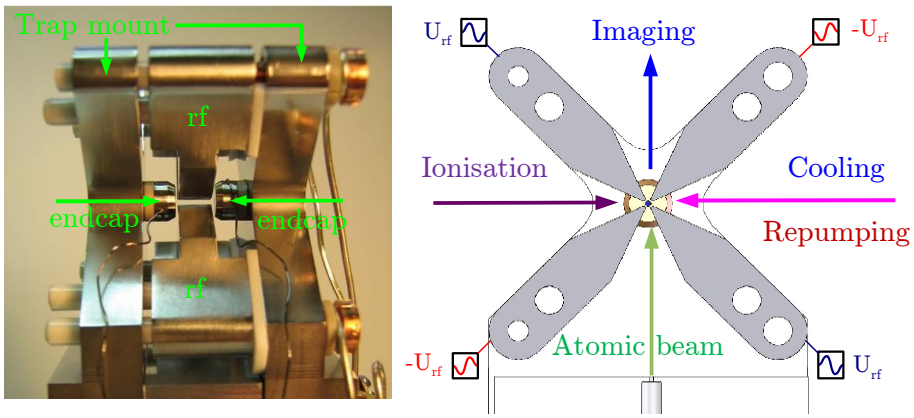

Figure 3.1: The trap (left) and optical access schematics (right). Rf is applied to the blade-shaped electrodes and dc to the cylindrical electrodes on either side of the trapping region.

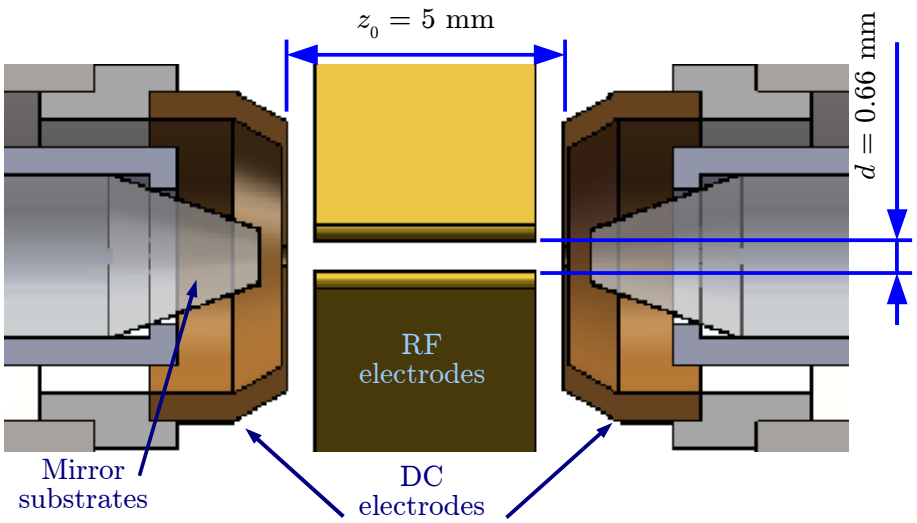

Figure 3.2: Close-up of the trapping region showing the spacing between dc electrodes (z_0) and the spacing between rf electrodes ($d = \sqrt{2}r_0$). Optical cavity mirrors are housed behind the dc electrodes in order to shield the ions from the mirrors' dielectric surfaces.

3.1.1 Trap design and construction

Each of the rf electrodes is held in place using a pair each of ceramic insulating dowell pins, slotted through the trap-mount and into the electrodes. Whereas many other blade-shaped electrode trap designs must have the electrode spacing adjusted manually – with the aid of a microscope – in order to maintain radial symmetry and even spacing, proper alignment in our design is ensured by the machining method.

The trap mount and electrodes are machined together from a single block of stainless steel. The holes for the mounting dowells are drilled *before* the mount and electrodes are finally separated. This ensures that when the trap is reassembled, the dowell pins hold the electrodes equidistant from the trap axis, and that this axis is aligned with the centre of the dc endcap-electrodes.

This method is made possible by the electrical discharge machining (EDM) technique used to machine the trap. EDM is a fully automated and computer programmable technique that can cut intricate contours from hard, conductive materials such as steel. The precision of the trap alignment depends only on this process.

Each rf electrode is insulated from the trap mount by a thin MACOR (a machineable glass-ceramic material) spacer that ensures they are centred in the z-axis, equidistant from the dc electrodes either side (Fig. 3.3). This spacer also provides a guide for a thin copper screw, in the place of one of the mounting dowell pins, and in contact with the

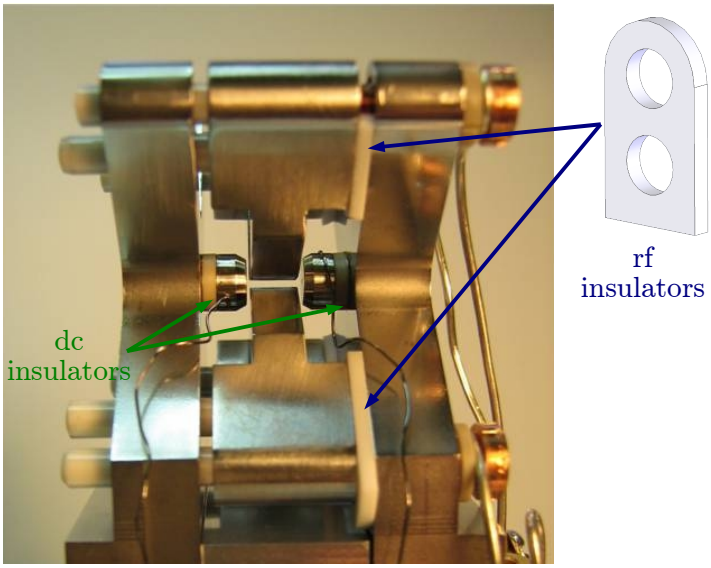

Figure 3.3: Rf and dc insulators isolate the trap mount from rf and dc voltages used for trapping.

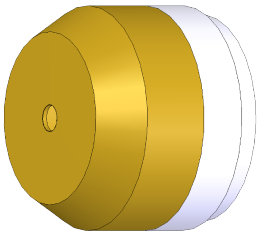

Figure 3.4: Dc electrode and PEEK insulator

rf electrode. The screw fastens down onto a ceramic washer, insulating it from the trap mount, and fixing the copper feedthrough wire that provides rf to the electrode from outside the vacuum chamber.

The dc electrodes are steel, hollow, flattened domes (Fig. 3.4). They are glued, using Ultra-High Vacuum (UHV) compatible glue, to insulating PEEK (UHV compatible, machineable plastic) spacers. These constructs are mounted inside holes in the centre of the trap mount that are aligned with the axis of the rf electrodes. The dc electrodes have 1 mm holes drilled in their centres to give the optical cavity mirrors access to the trapping region. Spot-welded tantalum wires provide dc voltage to the electrodes via feedthroughs to the outside of the vacuum chamber.

There is a large space beneath the trapping region left for the atomic oven mounting fixtures. In between the trapping region and these fixtures rests a long rectangular steel block, with a 0.5 mm hole drilled through its centre (Fig. 3.5). This block acts both as a

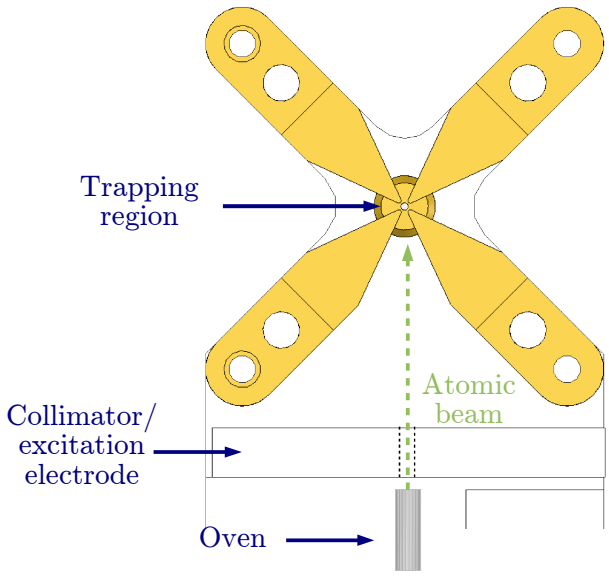

Figure 3.5: Oven collimator and excitation electrode.

collimator for the atomic oven effusion, and as an independent 'excitation' electrode with which to probe the secular frequency of trapped ions (section 3.4). The position of the block is manually adjusted with a magnifying lens so that the collimating hole lies directly beneath the trapping region. The block is then fastened in place using a steel screw. The block is electrically insulated from the trap mount and screw by 1 mm thick Kapton film (Kapton is an insulating, UHV compatible film that is stable up to 400°C). A copper wire is fastened to the block by a screw, and provides the excitation voltage via a feedthrough in the vacuum chamber.

3.1.2 Optical cavity mounting

The trap is integrated with a high-Q optical cavity for single photon and entanglement generation experiments. The cavity is aligned colinearly with the trap axis in order to couple with multiple ions for entanglement.

The mirror substrates are shown in Fig. 3.6, together with the trap electrodes to demonstrate their orientation. The mirror surface lies at the centre of the tapered end of the substrate. The surfaces of the two mirrors face each other through the 1 mm holes in the centre of the trap's dc electrodes. The substrates are mounted on piezo-electric transducers (PZTs) with a travel range of $\sim$3 μm. This allows for precision control of the cavity resonance frequency and adjustment over several FSRs.

The cavity mirrors are held in place using the collet, PZT and trap-mount arrangement

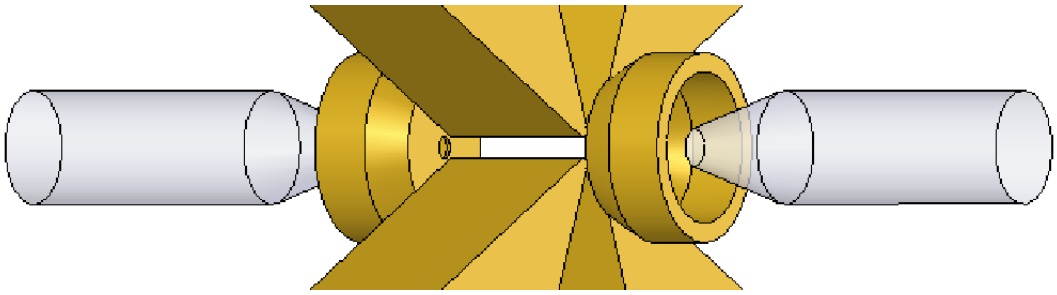

Figure 3.6: Orientation of the mirror substrates in the trap.

shown in Fig. 3.7. A soft, hollow PEEK screw holds the mirror in place inside the collet and allows optical access to the mirror surfaces from the outside. The collet, PZT and collet-mount are glued together using UHV compatible glue. The 1 mm diameter holes in the dc electrodes give the mirrors line-of-sight to the trapping region. The electrodes also shield the ions from field perturbations emanating from the dielectric mirrors.

For cavity-trap axis alignment, the mirror-mount arrangement is first attached to the trap-mount at only two diagonally opposite mounting points using a pair of steel screws. The other mounting holes in the trap-mount and mirror-mounts are left undrilled. The screws can be fastened so that the mirror-mount cannot move, but significant clearance between the screw body and the hole in the mirror-mount allows the position of the mirror surfaces to be adjusted first, until the cavity mode is determined to be coaxial with the trapping axis.

The position of the cavity axis is measured using a hypodermic needle mounted on a two-dimensional micrometer translation stage and a photodiode monitoring the transmission amplitude of a cavity-coupled 866 nm laser. The needle point is scanned in the radial plane between the rf electrodes, equidistant from the dc endcaps, where we expect ions to be trapped. The x-y position at which the resonant cavity transmission is only just blocked is taken to be the approximate centre of the cavity mode. The x-y positions of the electrodes are measured by lining the needle up to them using a x5 magnifying objective. When the cavity mode is found off centre from the trap axis, the mounting screws are loosened and the position of the mirror-mounts are adjusted to compensate, before the laser is recoupled to the cavity for another measurement.

Once the correct alignment is found, the mounting screws are fastened tightly. Whilst the arrangement is still well-aligned, additional holes are drilled in the trap-mount and mirror-mounts at the mounting points. Steel dowell pins are then inserted snugly into the

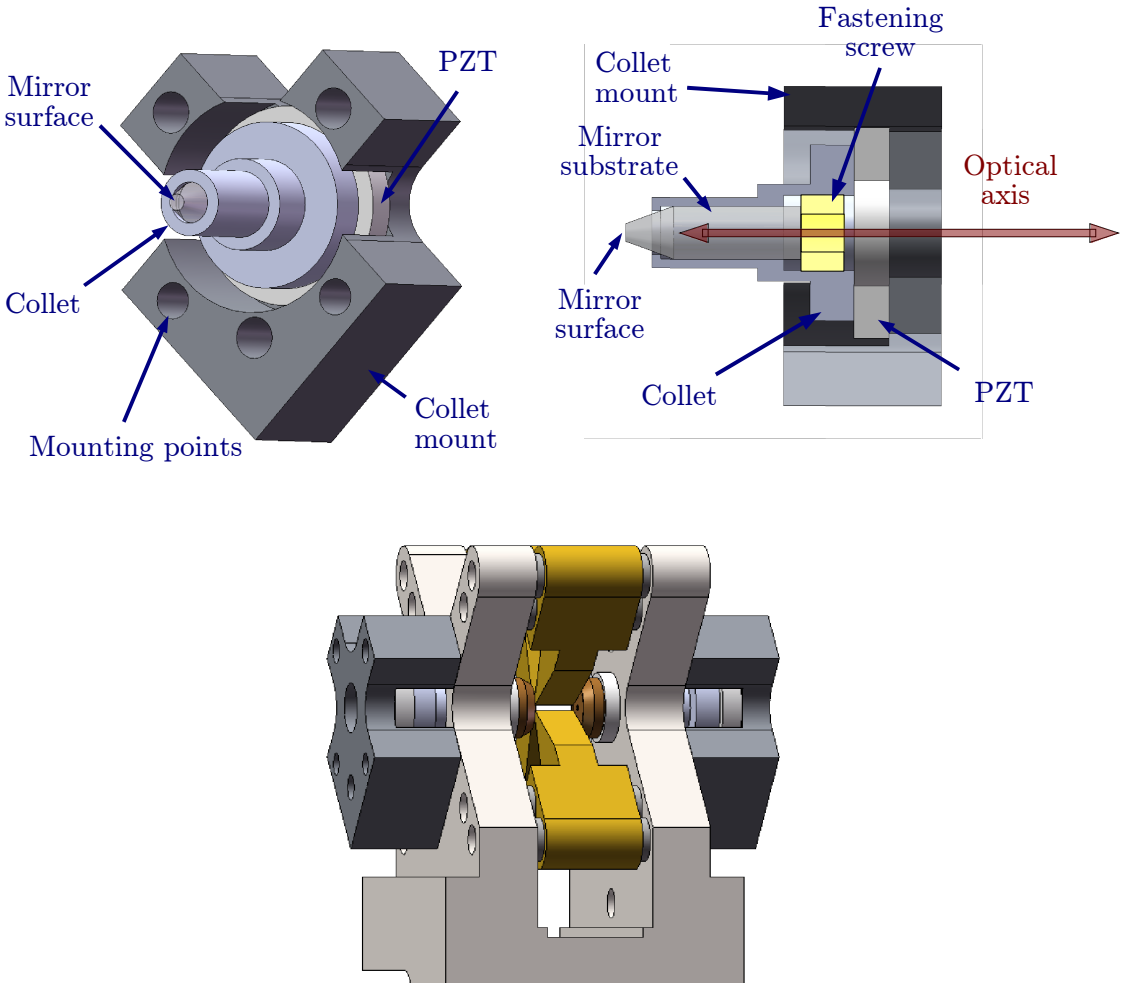

Figure 3.7: Mirror mounting assembly, showing the side facing the DC electrodes and trap (top-left) and cross section through the mirror (top-right). The cavity mirrors are held inside the collet using a soft, hollow teflon screw tightened from behind. Holes in the the collet-mount are used to secure the structure to the trap. The complete trap and cavity system is shown in the bottom panel.

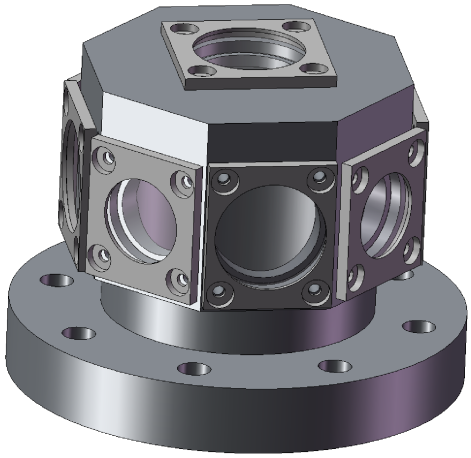

Figure 3.8: The octagonal vacuum chamber. Optical access from all angles with small angle of incidence to the windows is possible, maximising AR-coating performance and minimising polarisation distortion.

new mounting holes.

This procedure allows the mirror-mounts to be removed so that the mirrors can be replaced, whilst maintaining cavity alignment with the trap axis when they are reinstalled.

Once the trap is under vacuum and ions are held stably for long periods of time, we can make adjustments to the trap axis position on the micrometer scale by adjusting the amplitude of rf potential on the rf electrodes individually, using the rf resonator's variable capacitors (section 3.1.4). This is necessary to optimise the cavity-trap axis alignment, which must have a precision on the μm scale given the cavity-mode waist of 36 μm.

3.1.3 Vacuum chamber

The vacuum chamber that houses the trap and cavity setup is shown in Fig. 3.8. The octagonal chamber has a diameter of 20 cm, and is set with 1.5" diameter UV and IR anti-reflection coated windows in each side and the top. The windows are set into the chamber with brass clamps and indium seals for Ultra-High Vacuum (UHV) compatibility. The chamber geometry allows for excellent optical access from all directions whilst keeping the angle of incidence of the lasers on the windows relatively small and thereby optimising anti-reflection coating efficiency and minimising the distortion of the polarisation.

All the materials of the trap components are chosen for their stability at high temperature and resistance to 'out-gassing' – the process of evaporation from the surface of a material under low pressure conditions. Before the trap is assembled, every part is

cleaned for twenty minutes in an ultrasound bath. The trap is assembled with surgical gloves, using only tools that have also undergone ultrasound cleaning.

The vacuum chamber is bolted to an elbow on which are installed twelve UHV-compatible electrical feedthroughs for rf, dc, atomic oven and cavity-PZT control. An ion getter pump and UHV valve are attached to the this setup via a T-piece. All flanges are bolted together using CF-40 standard copper gasketts for UHV quality seals.

UHV is obtained by heating the chamber to 100°C and the ion pump and valve to 200°C for about a week, whilst pumping out gas and residual contaminants with a turbo-pump attached via the open valve. When the pressure is sufficiently low, the valve is closed and the turbo-pump is detached. The vacuum is then maintained by the ion getter pump and monitored via an integrated display that is calibrated to the amount of current across the pump electrodes.

Normal pressure under operating conditions is in the range of 10^{-11} mbar to 10^{-10} mbar, with the higher pressures occuring during operation of the atomic oven.

3.1.4 Rf resonant driving circuit

The rf circuit used to power the rf electrodes is shown in Fig. 3.9. This setup amplifies the voltage applied at the input using a voltage transformer stage. The secondary coil is centre tapped to the common ground of all of the trap systems. Either terminal of the secondary coil provides an rf voltage that is in anti-phase with the voltage at the other terminal. Each terminal provides the rf potential for a pair of opposite rf electrodes. The circuit is driven at its resonance, determined by the total capacitance of the system. A dc voltage can be applied for micromotion compensation via a resistor placed directly before the connection to the trapping electrodes (section 3.1.5). The variable and fixed capacitors behind the dc resistor AC-couple the rf drive and isolate the dc from the rest of the circuit.

The quality factor Q of the resonator, which is a measure of the losses in the rf circuit, is defined as

$$Q = \frac{f}{\Delta f}, \tag{3.1}$$

Where f is the resonance frequency of and Δf is the width of the resonance, defined as

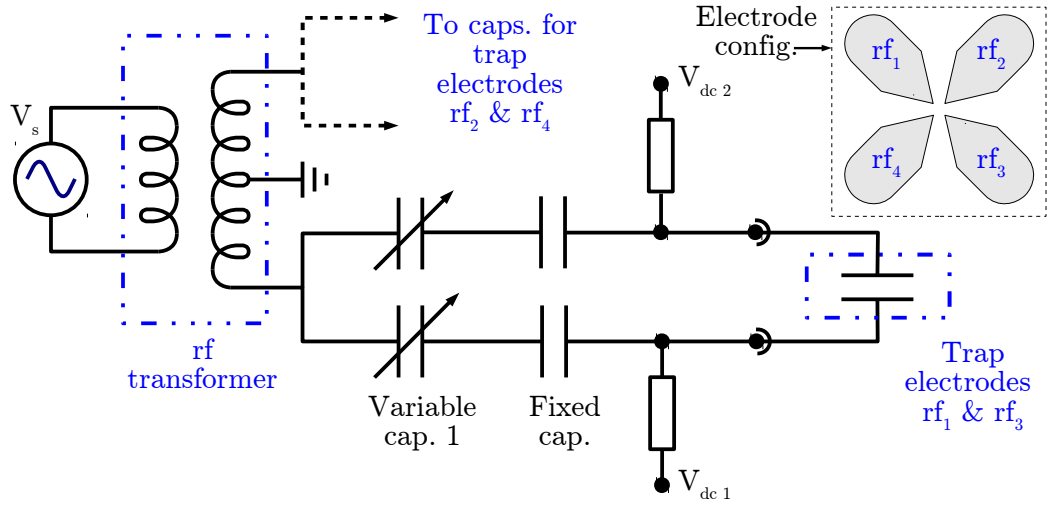

Figure 3.9: Trap resonator schematic. An rf transformer steps up voltage supplied by the source V_s. Variable capacitors in each output arm adjust the load capacitance of the trap electrodes in order to displace the position of the trapping pseudopotential minimum.

the full width at half power. Our resonant circuit setup has $Q = 56$ at the trap operation frequency 16.22 MHz.

The impedance matching of the driving source (50 Ω) with the resonant circuit impedance Z has been approximately optimised by monitoring the power reflected from the circuit (using an rf reflectometer) and adjusting the coupling between the primary and secondary coils of the rf transformer section. Nevertheless, power losses resulting from impedance matching of the driving source with the resonant circuit limit Q in this setup.

The dominant capacitance in the resonator comes from the capacitance of the trap. This has been approximately measured by attaching the rf circuit to a series of different capacitative loads until the resonance frequency matches that of the trap. The measured trap capacitance is $C \sim 25$ pF.

The voltage gain of the rf transformer, taking the approximations that the impedance is $Z = 50\ \Omega$ and that the trap capacitance is $C = 25$ pF, is given by

$$\frac{U_{\mathrm{rf}}}{V_s} = \sqrt{\frac{Q}{\Omega_{\mathrm{rf}} C Z}} = 21, \tag{3.2}$$

where V_s is the peak-to-peak voltage of the driving source. With maximum peak-to-peak voltage $V_s = 2.5$ V, we get $U_{\mathrm{rf}} \sim 52$ V.

In series with each of the four arms of the resonator is a variable and a fixed capacitor. The values of each are large compared to the trap capacitance. The variable capacitor

forms a capacitative voltage divider with the trap capacitance and allows independent adjustment of the rf amplitude on the rf electrode to which it is attached by modification of its capacitative load. It has been demonstrated [24] that by lowering the amplitude of the rf voltage on an electrode, the rf potential minimum can be moved in the direction of that electrode without affecting the harmonic shape of the potential or inducing significant micromotion heating of trapped ions. This mechanism can be used to optimise the overlap of the trap potential minimum with the mode of the optical cavity with precision in the order of micrometers [24]. We have achieved displacements of up to ~ 100 μm in this setup, measured using the imaging system described in section 3.2.5.

The rf centre of the trap can be moved in the horizontal and vertical planes (see Fig. 2.1) by adjusting the appropriate pairs of capacitors in tandem. Care must be taken however, that the rf driving frequency tracks the change in the trap resonance frequency that results from adjustment of the capacitance of the LCR circuit that the trap and transformer system creates.

3.1.5 Micromotion compensation

If we look back at the solutions of the Mathieu equation of the motion of a trapped ion (equations 2.9, 2.8), we are reminded that the radial motion is characterised by two distinct frequencies, ω_{r} and Ω_{rf}. Motion at the latter frequency is driven directly by the rf trapping field and is known as the micromotion. If a constant dc voltage is added to the potential, the minimum of the total potential will shift location. If the shift is, for example, in the x-direction, the equation of motion is modified as the ion is now displaced from the centre of the rf potential by x_{dc}:

$$x(t) = [x_{\mathrm{dc}} + x_0 \cos \omega_{\mathrm{rt}}](1 - q \cos \Omega_{\mathrm{rf}} t). \tag{3.3}$$

Thus even when the amplitude of secular motion x_0 approaches zero, the amplitude of micromotion is still $x_{\mathrm{dc}} q$. This is known as excess micromotion and causes undesired heating of the trapped particle and bad localisation in the radial direction. This shows why attempting to overlap ions with the cavity mode using static fields from the electrodes is problematic, and motivates the design of the rf resonant driving circuit described in the previous section.

In order to compensate stray dc fields from the environment and minimise excess micromotion constant dc voltages must be applied to the rf electrodes. Dc voltages are applied to the individual rf electrodes via resistors placed before the rf feedthrough connections on the rf resonator circuit. A capacitor behind this component acts to decouple this voltage from the rest of the rf resonator (Fig. 3.9). The voltages are supplied by a National Instruments DAC card with a LabVIEW-controlled software interface.

If V_n is the voltage applied to rf electrode n for compensation (Fig. 3.9), then the voltages required to create a horizontal or vertical field are

$$H = (V_1 + V_4) - (V_2 + V_3) \tag{3.4}$$

$$V = (V_1 + V_2) - (V_3 + V_4). \tag{3.5}$$

Furthermore, two additional parameters can be defined. Firstly Q, quantifying the static quadrupole component of the potential

$$Q = (V_1 + V_3) - (V_2 + V_4). \tag{3.6}$$

For a symmetric radial confinement, Q must be set to zero. Secondly S, a common dc offset for all the electrodes

$$S = V_1 + V_2 + V_3 + V_4. \tag{3.7}$$

This parameter modifies the axial confinement by changing the potential difference between the rf and dc electrodes.

The voltages V_1, V_2, V_3 and V_4 are determined by the micromotion compensation software interface according to the desired horizontal and vertical fields and the requirement that Q and S remain zero.

In order to compensate excess micromotion, we must have a way of measuring its effects. When static fields are fully compensated, the ion sits at the rf centre of the trap regardless of the depth of the trapping potential. Static fields push the ion away from the rf centre to an equilibrium position determined by the strength of the static field and the depth of the trapping potential. Thus micromotion can be monitored and coarsely optimised by modulating the rf trapping amplitude and observing the change in the ion's

displacement, as measured by the imaging system described in section 3.2.5. Changing the traps dc micromotion compensation voltages so as to minimise the ion's displacement amplitude is a simple and effective method of rough micromotion compensation.

Micromotion in the vertical plane is caused by static fields with a *horizontal* component in the trapping region. Using the rf amplitude modulation method it can be observed as a displacement in the horizontal plane that is in-phase with trapping amplitude modulation. It is compensated by the parameter H above.

Micromotion in the horizontal plane is caused by a static field component in the *vertical* direction and is thus compensated by V, above. It can be observed as an in-phase change in apparent *size* of the ion as it is displaced in and out of the focal plane of the microscope objective used for imaging.

Finer tuning of the micromotion compensation can be accomplished using rf-photon correlation measurements. Doppler shifts caused by the rf driven micromotion cause modulation of the cooling fluorescence collected by a PMT. A fast time-to-digital conversion card records photon arrival times and measures the cross-correlation with a signal from the rf drive [25]. The hardware that controls the micromotion compensation voltages can be programmed to map the rf-photon correlation amplitude for a range of H and V values in order to determine the setting for minimum micromotion. Since the Doppler shift for a laser in the horizontal plane is zero for ions with motion in the vertical plane, a cooling laser with some component in the vertical plane must be added in order to monitor and compensate micromotion in that plane.

3.2 Ion production and laser cooling

3.2.1 Ionised calcium-40

The ion used in these experiments is positively ionised calcium. ^{40}Ca has no nuclear spin and thus no hyperfine structure. Neutral ^{40}Ca is delivered to the trapping region by a resistively heated calcium oven made from a 20 mm long tantalum tube with 1 mm diameter, crimped closed at one end and filled with powdered calcium.

The oven mount shown in Fig. 3.10 is designed to electrically isolate the current supply used for heating. Large currents (up to 2.0 A) are required to deliver a sufficient flux of calcium for photoionisation in the trapping region.

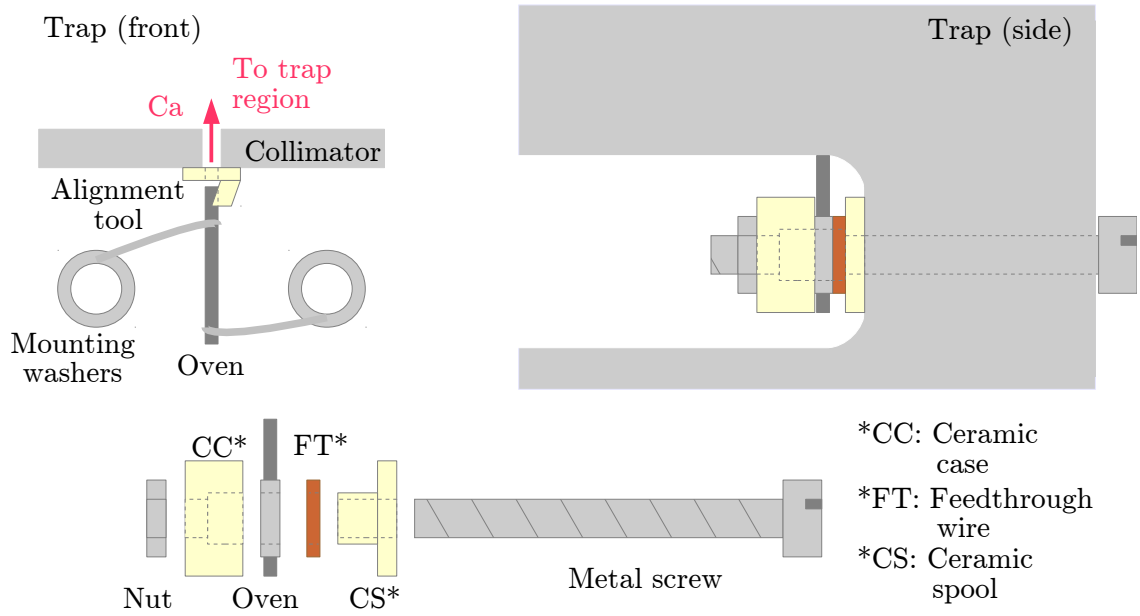

Figure 3.10: Oven mount design. Oven washers are mounted on a ceramic spool and case, which isolate the oven and feedthrough connections from the metal mounting screw and trap body. A metal plate with a 1 mm hole beneath the trapping region collimates the oven effusion. A small ceramic lip is used as an alignment tool to rest the oven tip beneath the collimator hole. Feedthrough wires in direct contact with the oven mounting washers provide up to 2 A current from an external power supply for resistive heating.

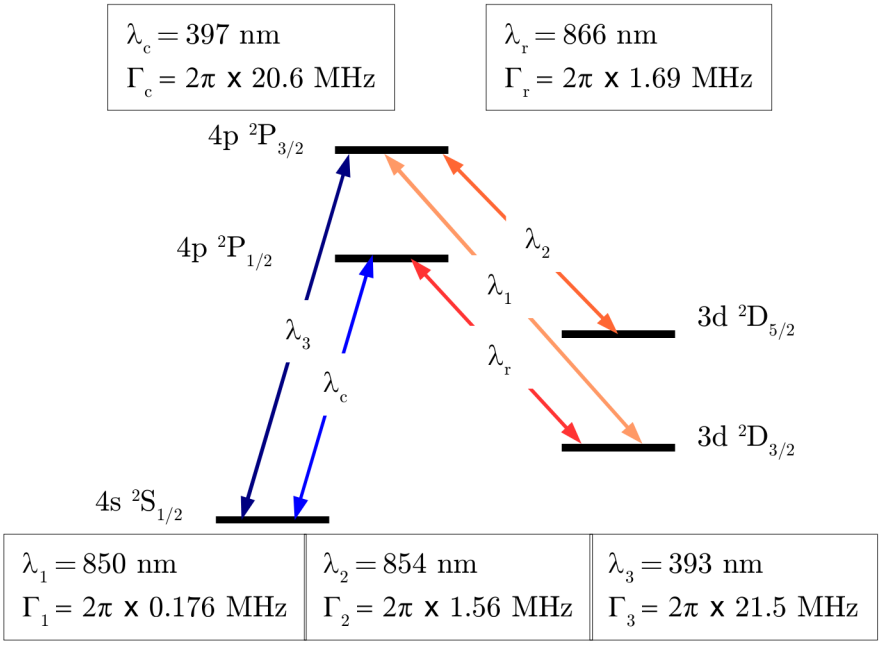

Figure 3.11: The relevant electronic structure of ionised calcium-40 with wavelengths of the transitions and associated decay rates.

Laser	Wavelength /nm	Power /μW
Cooling	396.95905(5)	<250
Repumper	866.45150(5)	< 500
Ionisation #1	422.79165(5)	75
Ionisation #2	$\leq$ 375	200

Table 3.1: Laser wavelengths and powers used for general trapping.

We employ a two-stage photoionisation process in these experiments. Firstly neutral ^{40}Ca is excited from the ground state $4s^2\ ^1S_0$, to the first excited state $4s4p\ ^1P_1$ with a 423 nm laser. The second stage applies a high frequency (<375 nm) laser to non-resonantly excite the electron to the continuum. Breaking down the photoionisation process like this allows us to use readily available laser frequencies and optical fibres, as well as providing isotope selectivity in the tuning of the 423 nm laser.

Ionisation leaves $^{40}Ca^+$, with a single active outer shell electron. The level scheme is shown in Fig. 3.11. The strong dipole transition from $S_{1/2} \rightarrow P_{1/2}$ at $\lambda_c = 397$ nm is used for Doppler cooling and imaging of the ions. However, the $P_{1/2}$ level can also decay into the $D_{3/2}$ state, with a branching ratio of 1:12. The $D_{3/2}$ state is meta-stable, with a lifetime of roughly 1 s, and so an additional laser at 866 nm is required to 'repump' the ion into the $P_{1/2}$ state where it will continue in the cooling cycle.

Potential problems with Rabi splitting and AC stark shift of the $P_{1/2}$ state by the repumping laser can be avoided by using lasers at $\lambda_1 = 850$ nm, which repumps to the $P_{3/2}$ state, and $\lambda_2 = 854$ nm, which repumps to the $P_{3/2}$ state from the $D_{5/2}$ state, should the electron decay there instead of to the ground state. In this way any effect of the repumping process on the $P_{1/2}$ state can be avoided.

The complete laser system for photoionisation and trapping is shown in Fig. 3.12. The laser wavelengths used are shown in table 3.1.

3.2.2 Cooling lasers

All of the lasers used in the experiment are diode lasers. The relevant transitions of the ^{40}Ca-ion are at wavelengths that are easy to obtain using diode lasers on their own or combined with frequency doubling systems.

The Doppler cooling transition of $^{40}Ca^+$ (shown in Fig. 3.11.) has a wavelength of 397 nm. To get laser light at this wavelength we use an infra-red laser (794 nm) and frequency doubling equipment. The diode, doubling crystal and cavity used to generate

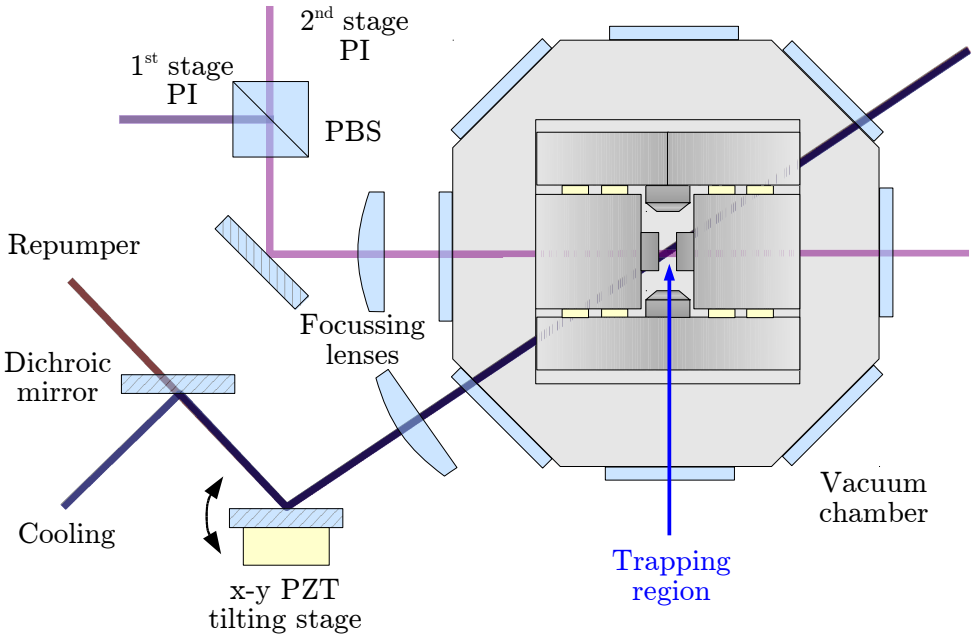

Figure 3.12: Cooling and photoionisation optics setup. 1^{st} and 2^{nd} stage photoionisation lasers are combined using a polarisation beam splitter (PBS) and brought to focus inside the trapping region. Cooling and repumper beams are combined using a dichroic mirror. A beam-steering mirror mounted on a x-y PZT tilting stage gives computer control of the beam direction, so that the trapping region can be systematically scanned for ion fluorescence.

Figure 3.13: Acousto-optic modulator (AOM) setup.

cooling light are provided by the integrated Toptica model "SHG 110", which provides up to 8 mW of 397 nm, linearly polarised light with frequency spectrum linewidth $\sim$ 1 MHz at its output.

After a few hundred microwatts of light is picked off by a glass plate for a wavemeter reading, the output is split into four arms by successive half-wave plate ($\lambda/2$) and polarising beam splitter (PBS) pairs (see "power distribution" in Fig. 3.13). The amount of power picked off per arm is determined by the angle of polarisation of the beam with respect to the axis of the PBS. This angle is determined by the rotation of the wave plate.

The PBS outputs have a polarisation purity of one part in a hundred, meaning that as long as the powers at the outputs are not drastically different, the polarisation of the beams remains approximately linear.

In order to control laser power, acousto-optic modulators (AOMs) on each arm of the cooling and repumper lasers are used. A schematic of the 'double-pass' optical setup for the AOMs is shown in Fig 3.13. This configuration gives an extinction ratio of 70 dB, rise

and fall time of ∼10 ns and response time of 150 ns, controlled with an approximately linear response by a single analog channel voltage between 0 V and 1 V, which in turn controls the rf power of the VCO which drives the AOM. The outgoing light is frequency shifted by 400 MHz, with a tuning range of ±100 MHz (-3 dB limit).

The output light from the AOMs is coupled into single-mode fibres that go directly to the trap setup. Fibres are used to easily get light from one optics table to another, but also have the additional property of spatially filtering the beam close to a Gaussian profile. At the experimental chamber the cooling beam is coupled out of the fibre using a fibre collimation lens and directed via a pair of beam-steering mirrors into the trapping region.

The beam is focussed into the trapping region, either by the fibre-coupling lens or a separate external lens, to minimise scatter from the electrodes or the trap mount.

3.2.3 Repumping laser

The laser used to repump the $D_{3/2} \rightarrow P_{1/2}$ transition is a home-made extended cavity diode laser (ECDL) unit. The extended cavity is formed using a ruled, blazed diffraction grating in the Littrow configuration [26]. The output beam has a linewidth of <1 MHz and a continuous single-mode tuning range of above 1 GHz. Coarse tuning to the atomic transition is achieved using the laser diode current and temperature controls, whilst fine tuning is accomplished via a piezo actuator controlling the grating angle.

The output of the 866 nm laser passes through a Faraday isolator used to prevent optical feedback interference, and a pair of cylindrical lenses for removing astigmatism. Beam power at the experiment is controlled by AOMs as in Fig. 3.13, and coupled to the experiment by a single-mode optical fibre.

The beam is overlapped with the cooling beam (397 nm) through a long-pass dichroic mirror. Precise pointing of the combined beams to the centre of the trap is controlled externally by the voltage applied to a PZT tilting-stage mounted beam-steering mirror. This beam steering mirror can be controlled via Digital-to-Analog Converters (DACs) that are interfaced to a nearby computer, so that the trapping region can be systematically scanned for ion fluorescence, when the trap optics are first being aligned.

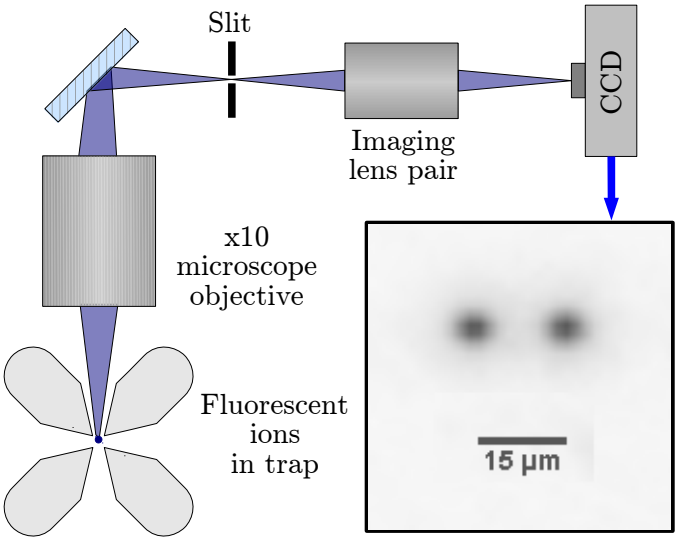

Figure 3.14: Trap imaging system. A x10 magnification microscope objective lens placed 75 mm from the trap centre collects fluorescence from the trapping region. Fluorescence is imaged first at a razor slit that cuts out stray light from outside the focal plane, and then by an imaging lens pair onto the CCD camera. The image shows a pair of trapped ions, separated by 15 μm

3.2.4 Photoionisation lasers

The two lasers used for photoionisation are also lab-made units. The 423 nm laser needs to be tunable and of narrow linewidth in order to avoid loading unwanted isotopes into the trap, and so this one is constructed to the same ECDL design as the repumper. The second stage however is non-resonant and need only have a wavelength shorter than 389 nm, which can be achieved without an extended cavity.

3.2.5 Imaging systems

Ions are detected in the trap by imaging the fluorescence from the Doppler cooling transition. A schematic of the imaging optics is shown in Fig. 3.14.

A x10 magnification microscope objective is used to create an image of the ions above the trap, where a slit formed from four razor blades is placed in order to cut out stray light from outside of the focal plane. The fluorescence is reimaged at the image plane of a high sensitivity CCD camera (Andor "Luca" S) by a lens pair chosen to have x1 magnification. The scale of the image is determined by the separation of the electrodes on the CCD image, and the size of the pixels on the CCD. The spacing of the trap electrodes seen in the CCD image indicates that the width of single pixel corresponds to 1 μm in the object plane.

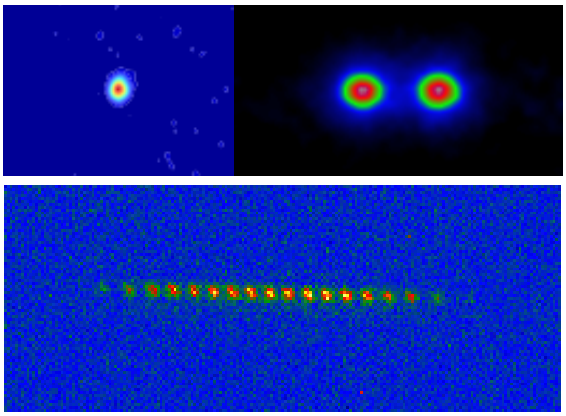

Figure 3.15: A single ion (top-left), a pair of ions (top-right), and a string of many ions (bottom) trapped in the rf trap.

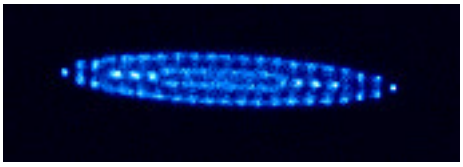

Figure 3.16: A multi-layer ion crystal.

Depending on whether we need to see scatter from photo-ionisation and repumper lasers for alignment purposes, we can choose to install or remove a 397 nm notch filter in the fluorescence path. This filter attenuates scatter from the repumper and photoionisation lasers, only allowing UV fluorescence from the ion to reach the CCD.

3.3 Trapped ions

Ions can routinely be trapped in the trap for long periods of time. Loading a single ion takes less than a minute. Once the oven is warmed up, subsequent ions load within seconds. Figure 3.15 shows a single trapped ion, a pair of trapped ions, and a long string that can be used for multi-ion entanglement.

With a relatively low axial confinement we can make strings up to thirty ions long. By increasing the axial confinement or decreasing the radial confinement we can make multi-layer crystals such as the one shown in Fig. 3.16. Crystals such as this can be loaded within five minutes.

Ion lifetimes vary according to the number of ions in the crystal. A single ion has a lifetime of at least an hour. Strings of up to thirty ions have been trapped for several minutes. The likely mechanism for ion loss is collisions with background contaminants in

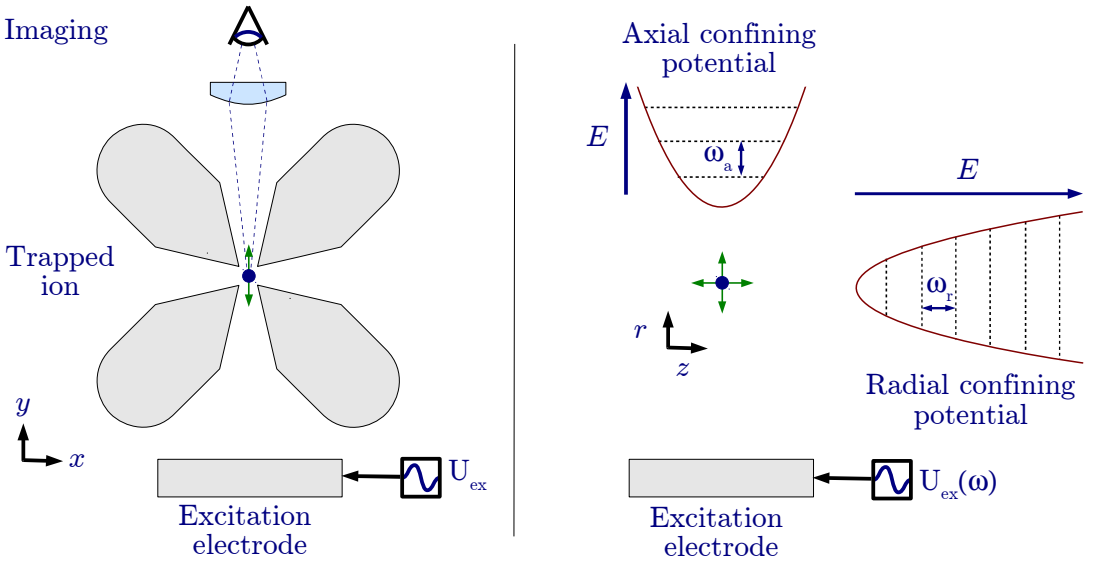

Figure 3.17: Secular frequency measurement setup (left). Fluorescence from the trapped ion is monitored as the frequency of the excitation U_{ex} is scanned. When the excitation is resonant with either radial or axial trapping potential frequencies (right), the ion's motion is resonantly driven, it heats, and fluorescence drops due to Doppler broadening of light seen in the rest-frame of the ion.

the vacuum chamber.

3.4 Secular frequency measurements

Equations 2.10 & 2.14 define the radial and axial secular frequencies of the trap, and equations 2.4 & 2.5 define the q and a parameters. In this experiment $Q = e$, $m = 40$ a.u., $\Omega_{rf} = 2\pi{\cdot}16.35$ MHz and $U_{\mathrm{rf}} = 21 \cdot V_s$, where V_s is the amplitude of the rf drive source.

In the limit that the axial confinement is small compared to the radial confinement, which is the case in our experiments, the radial secular frequency is proportional to V_s. The axial frequency is proportional to $\sqrt{U_{dc}}$.

The secular frequencies of the trap are measured by applying a variable-frequency modulation to the excitation electrode and monitoring the fluorescence from a trapped ion (Fig. 3.17). If the modulation is resonant with the secular motion of the ion, it is significantly heated and is Doppler shifted out of resonance with the cooling laser. This results in reduced fluorescence and delocalisation in the direction of the secular motion. It is possible to distinguish between the axial and radial resonances by the direction of delocalisation as well as by observing the frequency shifts resulting from changes in experimental parameters.

The measured radial and axial secular frequencies ω_r and ω_a are shown as functions of rf source voltage V_s and dc voltage U_{dc} respectively in Fig. 3.18.

The radial frequency plot shows a linear slope as expected. The offset results from the contribution of a at small values of q. Assuming a is small

$$q = \frac{2\sqrt{2}\omega_r}{\Omega_{rf}}, \tag{3.8}$$

The slope of $f_r(V_s)$ is 1.49 MHz/V. This implies

$$q = 0.26 \text{ V}^{-1} \cdot V_s \tag{3.9}$$

Therefore for $V_s = 2.5\ V$ (the maximum available source voltage), $q = 0.66$.

The axial secular frequency is given by Eq 2.14. The axial secular frequency data in Fig. 3.18 gives

$$f_z = \alpha\sqrt{U_{dc}}, \tag{3.10}$$

with $\alpha = 26.7 \text{ kHz}/\sqrt{V}$. This implies $\eta = 0.03$. Combining this with Eq. 2.5, we find

$$a = -1.1 \cdot 10^{-5} \text{ V}^{-1} \cdot U_{dc}. \tag{3.11}$$

The power supply for the axial confinement potential goes up to 150 V. The maximum achievable a is therefore $a = 1.7 \cdot 10^{-3}$.

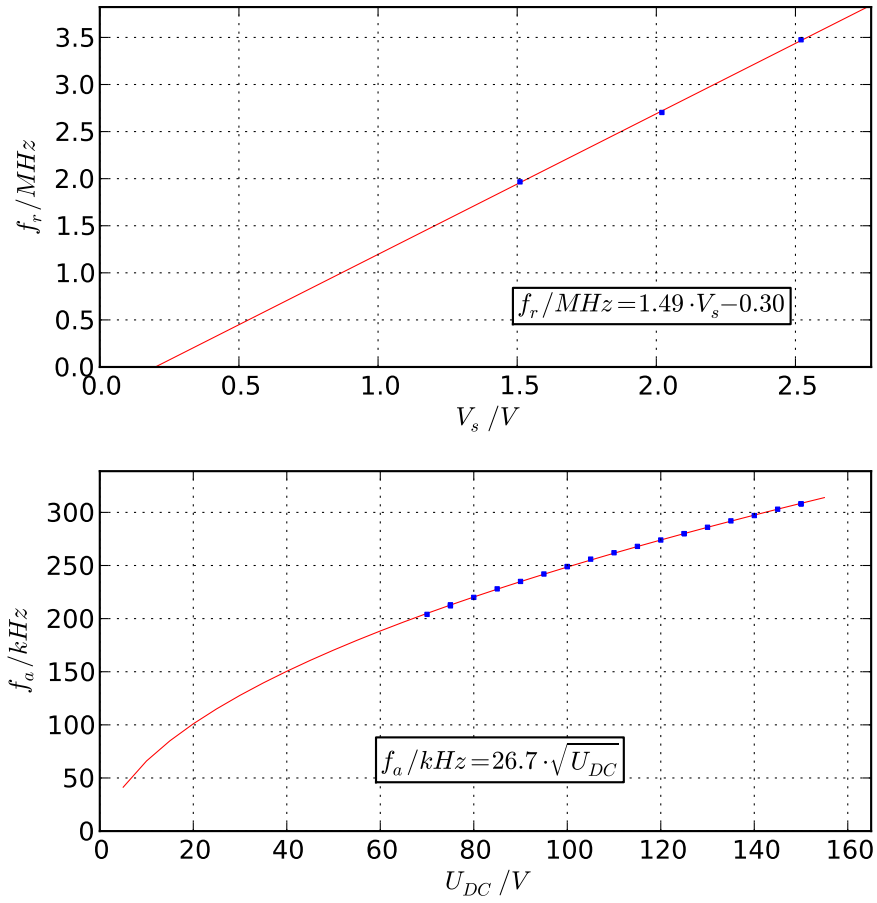

Figure 3.18: Secular frequency measurements with varying potentials V_s (proportional to U_{rf}) and U_{dc}, made by resonant excitation of the secular motion of the ions.

Chapter 4

Atomic frequency reference

All of the laser systems described in section 3.2 must be frequency stabilised to within the linewidth of the transitions they address. This linewidth is typically in the order of megahertz. For initial optimisation of the trap it is usually sufficient to use a wavemeter reading (calibrated using a Helium-Neon reference laser), to feedback to the laser's frequency control and thereby lock the frequency as desired. However the resolution of the wavemeter is low (∼60 M Hz) and feedback bandwidth is generally limited by the slow update rate of the control computers over the internal network (∼2 Hz). Furthermore, experiments with the experimental cavity require that it is stabilised to below the linewdith of the cooling laser (1 MHz) for the cavity assisted Raman transition process on which single photon generation is based.

For these purposes we have developed a frequency-stable diode laser to use as a reference. Using the setups described in chapters 5 & 6, we can lock the other lasers and the experimental cavity to this reference with a high degree of accuracy.

The multi-stage locking scheme for the reference laser is shown schematically in Fig. 4.6. The first stage provides short-term stability by locking the laser to a Fabry-Pérot cavity using the Pound-Drever-Hall technique [27, 28, 29]. The cavity has a linewidth of 1 MHz. By adjusting the length of the cavity, we can tune the laser over a frequency range of several GHz.

Because the cavity length is not stabilised it is subject to long-term frequency drifts. In order to provide absolute frequency stability for the laser, we perform atomic caesium spectroscopy in a vapor cell at room temperature. From this spectroscopy we derive a dispersion signal centred at the D_1 transition of Cs (894 nm). The signal is used to

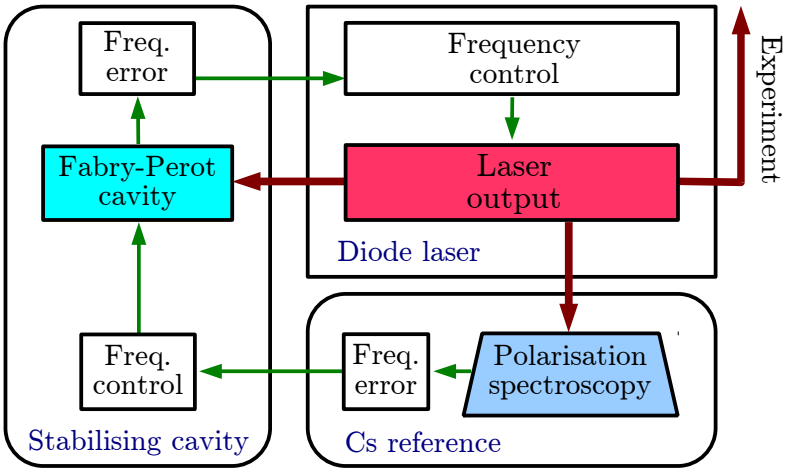

Figure 4.1: Schematic of Cs-laser stabilisation system. The laser's short-term frequency fluctuations are stabilised to the Fabry Pérot cavity, which is also used to tune the laser over a large frequency range. The laser simultaneously probes a Cs-gas cell using the polarisation spectroscopy technique. The frequency error signal derived from this technique is used to lock the laser frequency, via the cavity, to the frequency of the D_1 transition in the gas.

control the length of the Fabry-Pérot cavity and thus, via the first locking stage, the laser frequency, locking it to the atomic reference.

The stabilisation techniques and optical setup are described below, and measurements of the stability of the system are reported.

4.1 Stabilising cavity

The laser is locked to the stabilising cavity using the Pound-Drever-Hall technique: Radiofrequency current modulation of the diode-laser current supply generates frequency sidebands in the spectrum of the output, which are separated from the carrier frequency by the rf modulation frequency. In our experiment this modulation is 10 MHz. If the laser is resonantly coupled to an optical cavity, the sideband components of the spectrum are reflected as long as the rf frequency is higher than the linewidth of the cavity resonance. The beat note of the reflected sidebands and the carrier is monitored by a photodiode. The photodiode output is electronically mixed with the rf oscillator signal (that is used to create the sidebands) to give an output that is linear with the phase-difference between the beatnote and the oscillator. The phase of the beatnote is determined by the complex cavity reflection function. Close to resonance, the phase has a linear relationship with the laser detuning (see Fig 4.2). This provides an error signal that is fed back to the laser

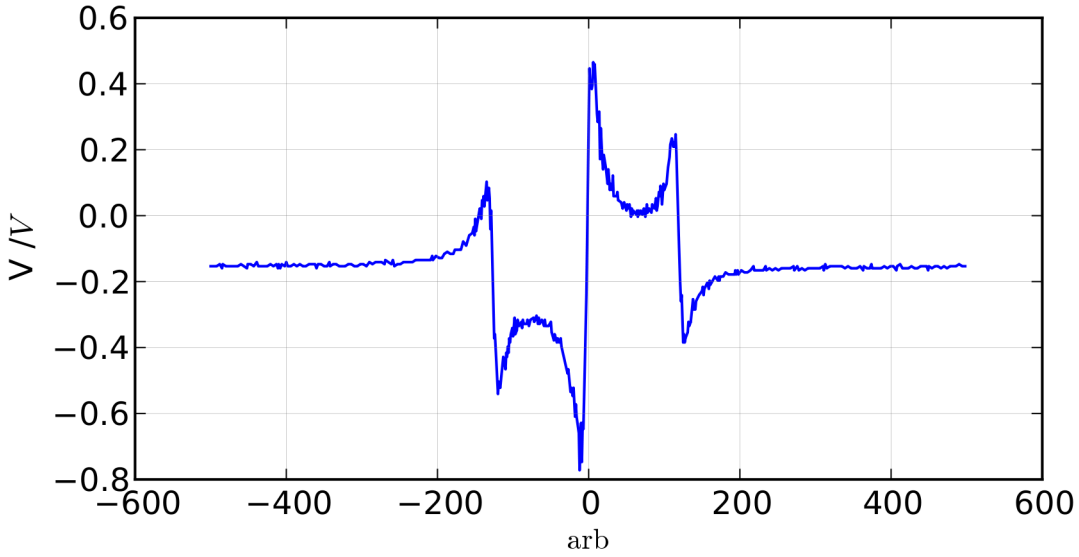

Figure 4.2: Pound-Drever-Hall error signal. The signal has a large linear slope around the resonance (zero on the horizontal axis above).

frequency control in order to keep it on resonance with the cavity.

4.1.1 Feedback electronics

All the feedback controls of the atomic reference system are provided by analogue electronics. The Pound-Drever-Hall error signal is sent to a proportional-integral-differential (PID) feedback circuit, shown in Fig. 4.3, used to lock the laser to the cavity.

Proportional feedback has high bandwidth and feeds the error signal directly back to the frequency control after amplification. This is insufficient for accurate locking on its own since by definition the feedback signal is small when the laser is close to resonance – this usually results in a lock with fixed offset from the desired locking point.

Integral feedback has low bandwidth and gain that increases logarithmically at low frequencies. Long term offsets and drifts, such as those resulting in proportional-only feedback, are compensated by properly tuned integral feedback.

Differential feedback works only on the high frequency components of the error signal. There is typically a constant time delay between error detection and feedback actuation, accrued as the signal propagates through electronic components of the system. Resultant phase delays in PI feedback signals can cause locking instabilities at high frequencies. The phase response of differential feedback as a function of frequency can compensate this to some extent, and allow for higher total (PID) locking bandwidth.

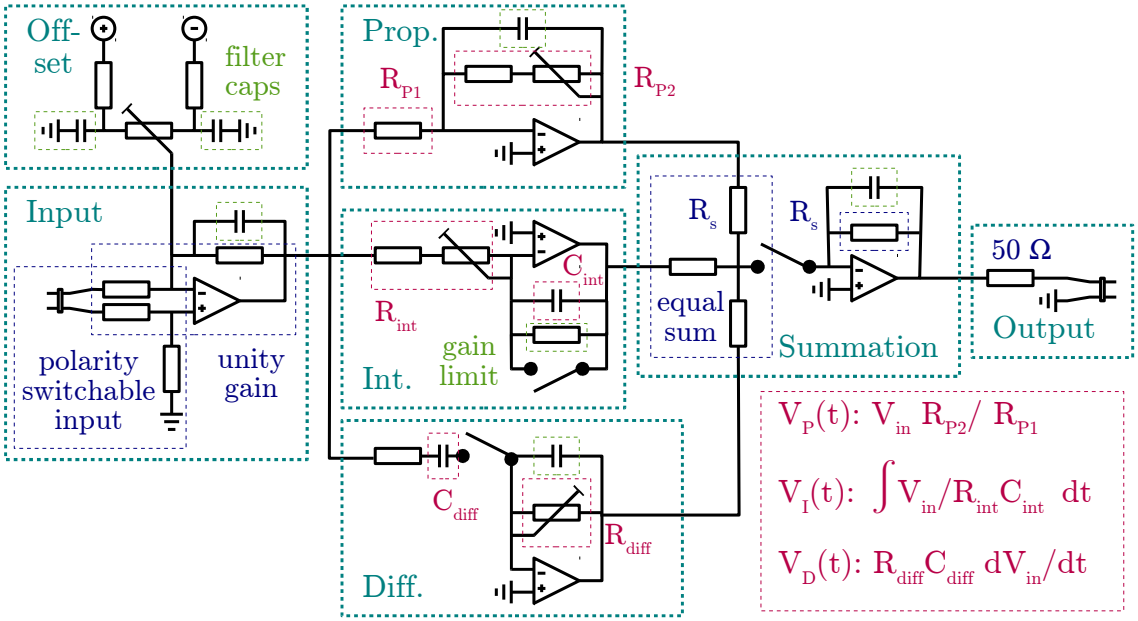

Figure 4.3: Circuit schematic for proportional (Prop.), integral (Int.) and differential (Diff.) feedback control (also known as PID). The Offset circuit allows for manual compensation of error signal offsets from the PDH technique.

4.2 Atomic spectroscopy

The method used to generate the locking signal from the caesium transition is known as polarisation spectroscopy. Our implementation of this technique is based on the setup demonstrated by C P Pearman et. al. [30], with a few modifications. It is a form of sub-Doppler spectroscopy that relies on optical pumping to induce birefringence in the medium. The absorption characteristics of this induced birefringence are frequency dependent, and interrogated by a weak, counter-propagating probe beam. Counter-propagation of pump and probe beams ensures that only atoms that have zero velocity component in the direction of the beams contribute to the signal, eliminating the effects of first order Doppler broadening.

The linearly polarised probe beam passes through the medium. The direction of its polarisation is then analysed with a polarising Wollaston prism, oriented in a way that the original probe beam is split into two orthogonally polarised beams of equal intensity. The intensities are measured with a pair of photodiodes and subtracted from each other, giving an output value of zero for a probe beam passing through a medium that is not pumped.

In the absence of the circularly polarised pump beam the medium has no birefringence.

Birefringence can be induced in the medium by 'optical pumping' with the σ_- circularly polarised pump beam. The polarisation of the pump beam only allows transitions to upper states in the D_1 transition with $\Delta m_F = +1$. Although a spontaneous transition may have $\Delta m_F = -1, 0, +1$, if the pump is strong enough the entire population will trapped the highest m_F states of the upper and lower levels. Once optically pumped in such a way, the atoms can no longer absorb σ_- polarised photons, because there is no higher m_F state to populate. Thus, the medium becomes effectively transparent to the σ_- component of the probe beam, whilst still being absorptive for the σ_+ component.

The frequency dependent phase delay acquired by the σ_+ component of the probe beam after passing through the optically pumped medium is characterised by the Kramers-Kronig dispersion relation. This relation states that the profile of the phase delay is proportional to the differential of the absorption profile of the transition being probed. The net effect on the total polarisation of the probe beam is that the axis of linear polarisation is rotated by a small angle, that follows the dispersion profile of the atomic transition.

The resultant signal after subtracting the two linear components of the probe beam separated at the output prism is a dispersion curve, approximated by [30]

$$I_{signal} = -I_0 e^{-\alpha L} \left(L \Delta\alpha_0 \frac{x}{1+x^2} \right). \tag{4.1}$$

Here, $\alpha = \frac{1}{2}(\alpha_+ + \alpha_-)$, where $\alpha_\pm$ are the corresponding absorption coefficients for $\sigma_\pm$ polarisations, L is the length of the Cs gas cell, $\Delta\alpha_0$ is the maxiumum difference in absorption of the two polarisations (at the line centre) and $x = \frac{\omega_0 - \omega}{\Gamma/2}$ is the linewidth-scaled detuning. The profile is shown in Fig. 4.4, with a cavity spectrum signal for frequency scale (10 MHz sidebands are seen on the carrier frequency). It is ideal for use as a feedback signal for laser frequency locking – i.e. linear within the region of the centre of the line frequency.

4.2.1 Feedback electronics

The electronics used to tune the laser, via the PDH cavity, into lock with the caesium reference frequency are outlined in Fig. 4.5. This system is a simplified version of the electronics shown in Fig. 4.3 that uses only integral feedback and electronics to manually null any offset of the error signal coming from the signal generating circuit. Only the

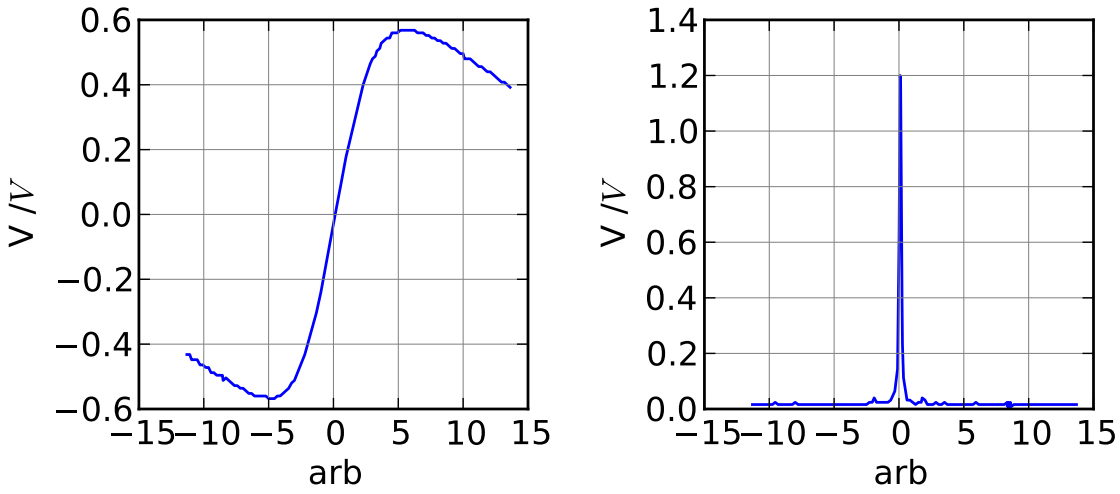

Figure 4.4: Polarisation spectroscopy (left) and stabilising cavity transmission (right) signals, recorded simultaneously during a scan of the laser frequency. Frequency sidebands seen in the laser spectrum at 10 MHz are used to convert the spectroscopy signal amplitude to a frequency scale for analysing the quality of locking.

integral part is used because we only need feedback on a long timescale, and depend on the PDH cavity for stability at higher frequencies.

4.3 Optical setup

The optical setup for the complete reference system is shown in Fig. 4.6. A Faraday isolator ensures that minimal light is reflected from the optics back to the laser, preventing undesired optical feedback and frequency noise. A glass plate is placed directly after the isolator to pick off a small amount of power for frequency monitoring by a wavemeter. All but the top left polarising beam splitters (PBS) are paired with half-waveplates ($\lambda/2$) to allow the user to divert the power from one output arm of the PBS to the other as required, by rotating the incoming polarisation with the waveplate.

The deflected output of the PBSs has a quoted polarisation purity of one part in a hundred. It has been observed that when the ratio of output intensities is of the order of 1:100, the polarisation of the deflected beam has a large, random and drifting component. In the case of the PBS that selects the probe beam power this ratio is large and without any further manipulation the polarisation dependent signal has a large long term drift associated with that random component. To eliminate this effect, we add a nano-particle linear film polariser with one part in ten-thousand polarisation purity at the output to

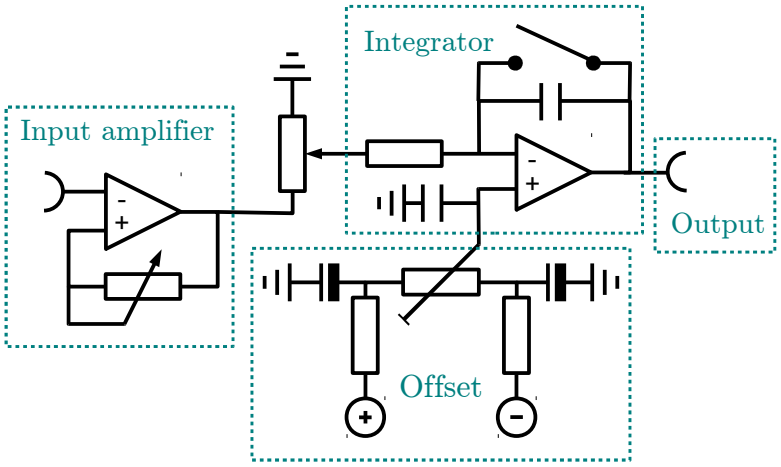

Figure 4.5: Feedback electronics for locking the laser-cavity to the polarisation spectroscopy signal. This system incorporates only integral feedback for long-term stabilisation, and a circuit for manually compensating any offset of the error signal.

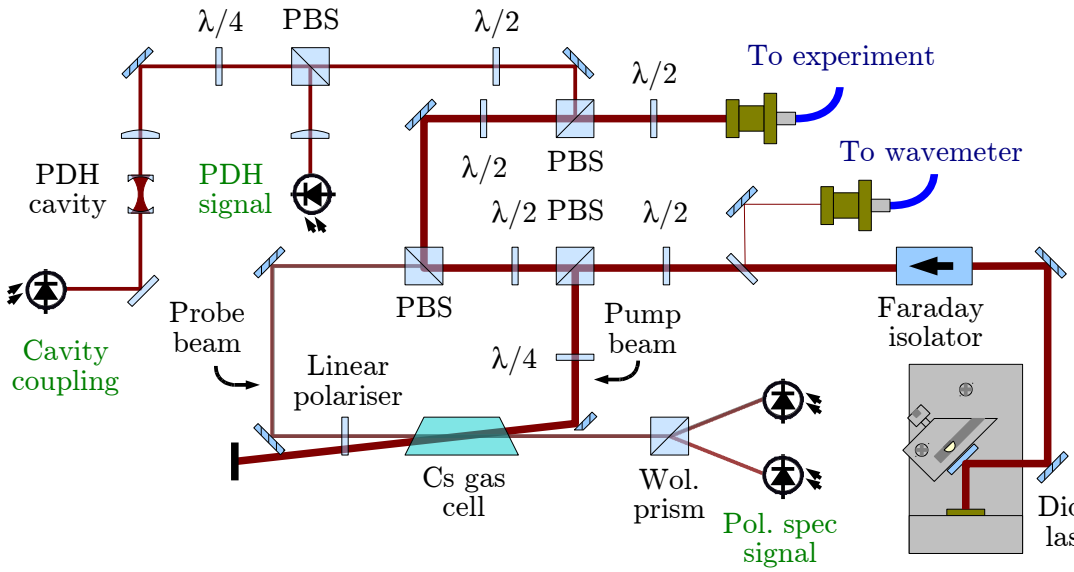

Figure 4.6: Optical setup for the atomic reference laser. Pump and probe beam powers are adjusted using half-waveplate and PBS pairs. The pump and probe beams are at a small angle with respect to each other, but overlap well within the gas cell. Another half-waveplate and PBS pair adjust the proportion of power that goes to the experiment. The remaining power is used to lock to the PDH cavity.

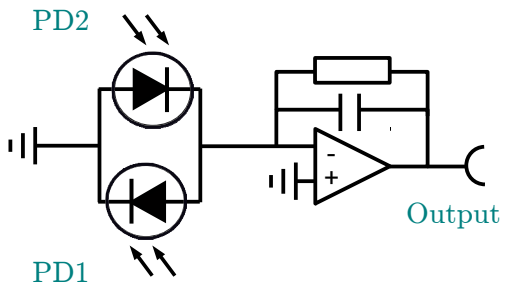

Figure 4.7: Polarisation spectroscopy detector electronics. The circuit is designed so that the difference between the intensity at the two photodiodes is amplified at the output. A capacitor in parallel with the feedback resistor limits the bandwidth of the detector to a few hundred hertz, to limit electronic noise.

precisely define the polarisation of the probe beam. Polarisation fluctuations at the initial PBS still cause amplitude drift in the probe beam but if the polarisation angle with respect to the detector is well balanced this translates only as an amplitude drift in the error signal.

Due to similar polarisation purity concerns in the polarisation spectroscopy signal detection setup, we have replaced the detector PBS that was used in Ref. [30] with a polarising Wollaston prism. The deflection angle of this beam splitter is less than ninety degrees but the polarisation purity in the two arms of this prism is one part in ten-thousand.

A quarter waveplate transforms the linearly polarised pump beam into circular polarisation for optical pumping.

The polarisation spectroscopy signal is generated by the circuit shown in Fig. 4.7. It subtracts the signals from identical, large area photodiodes placed so that they measure the intensity of the two linear components of polarisation coming from the Wollaston prism.

The Cs gas cell is a quartz reference cell from Thorlabs, 75 mm long, with angled windows to avoid offsets on the detectors from internal reflections in the cell.

The final PBS and half-waveplate pair (top-left) belong to the PDH setup and are set up so that all of the incoming beam power passes through the PBS. The beam then passes through a quarter waveplate to convert the polarisation into circular. The component of the beam that is reflected from the cavity for the PDH signal (section 4.1) passes through the quarter waveplate once more, being converted back to linear polarisation at 90° from the incoming beam polarisation. It is therefore reflected from the PBS onto the PDH photodiode for mixing with the local oscillator signal. A photodiode is placed at the

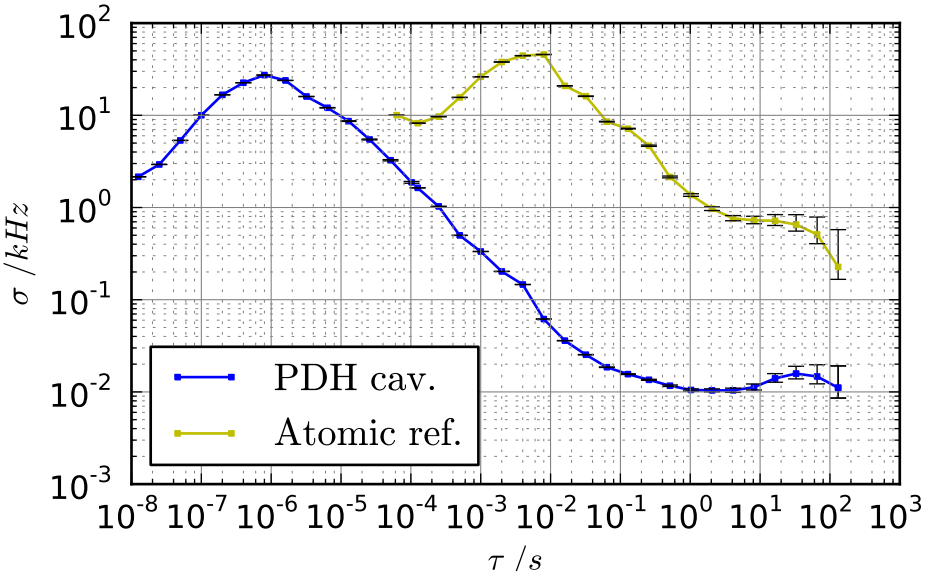

Figure 4.8: Scaled Allan variance stability measurements for the Pound-Drever-Hall lock (blue) and polarisation spectroscopy (yellow) error signals. The data shows stability under 100 Hz on timescales larger than 10 ms.

transmission output of the cavity in order to monitor and optimise the coupling of the laser to the cavity mode.

The PBS (top-right) before the PDH setup picks off the majority of the beam power, to be coupled by fibre to the experiments that require the atomic reference signal.

4.4 Frequency stability measurements

In order to ascertain whether the stability of the locked frequency reference system is sufficient for locking the experimental cavity, measurements have been made to characterise the locking systems.

The data is presented in Fig. 4.8 as a plot of the scaled 'Allan variance' σ of the PDH and polarisation spectroscopy error signals. The Allan variance is defined as follows:

$$\sigma_y^2(\tau) = \frac{1}{2}\langle(\Delta y)^2\rangle. \tag{4.2}$$

The variance is taken over a set of normalised data y. The expectation value of the difference between adjacent (in time) measurements Δy is calculated to give the Allan variance for a range of time intervals τ. The advantage of this variance over the classical variance is that we can see the stability over the different time-scales that are relevant to different locking mechanisms.

The PDH data shown in Fig. 4.8 shows the quality of locking between the laser and stabilising cavity. The maximum variance is 30 kHz at $\tau = 10^{-6}$ s. The stability at long timescales is as small as 20 Hz for $\tau = 30$ s. The peak seen at this value of τ corresponds directly in amplitude to the quoted long-term stability of the voltage regulator used to define the locking point of the error signal in the PID box (Fig. 4.3). This drift is expected to average out over longer timescales.

The short-term stability of our reference laser only needs to be less than the linewidth of the experimental cavity, which is typically about 500 kHz. The PDH stability measurements above indicate that we are well within this margin.

The quality of lock data for the polarisation spectroscopy signal shows absolute levels of stability similar to the PDH data. The data indicates that for timescales within the bandwidth of the polarisation spectroscopy lock ($\tau > 10^{-2}$ s) the stability of the complete system is limited by noise of the spectroscopy signal. We obtain a maximum variance of 40 kHz and long-term stability of at least 200 Hz.

Chapter 5

Fast scanning cavity offset lock

The level diagram in Fig. 3.11 shows that our experiment requires a potentially large number of frequency stabilised laser sources. Depending on the re-pumping scheme or later photon generation and entanglement operations, we require locking of up to five lasers between 794 nm (the fundamental frequency of the frequency doubled cooling laser) and 866 nm to sub-megahertz linewidths, with similar long-term stabilities.

A typical technique for transferring the stability of a master frequency reference to another laser is to lock the length of a stabilising optical cavity to the master (using for instance the PDH technique described in section 4.1), and then to lock the slave laser to that cavity by tuning it to resonance with the cavity using an acousto-optic modulator. This method can achieve sub-hertz stability but is expensive to extend to multiple lasers, as each new laser requires a cavity and locking electronics system.

A more viable alternative for the moderate stability requirements of our experiment is to use a single cavity, to which the experiment's lasers are coupled, and to scan the length of the cavity and register the transmission peaks of each of the lasers in turn at the output. The lasers can be locked to each other by stabilising the relative position of their transmission peaks in the scan. If one of these lasers is a master frequency reference, then its stability is transferred to all of the slave lasers at once.

To this end, a scanning cavity offset locking system has been built at the lab according to a new design [31] that improves on previous implementations [32, 33, 34, 35, 36].

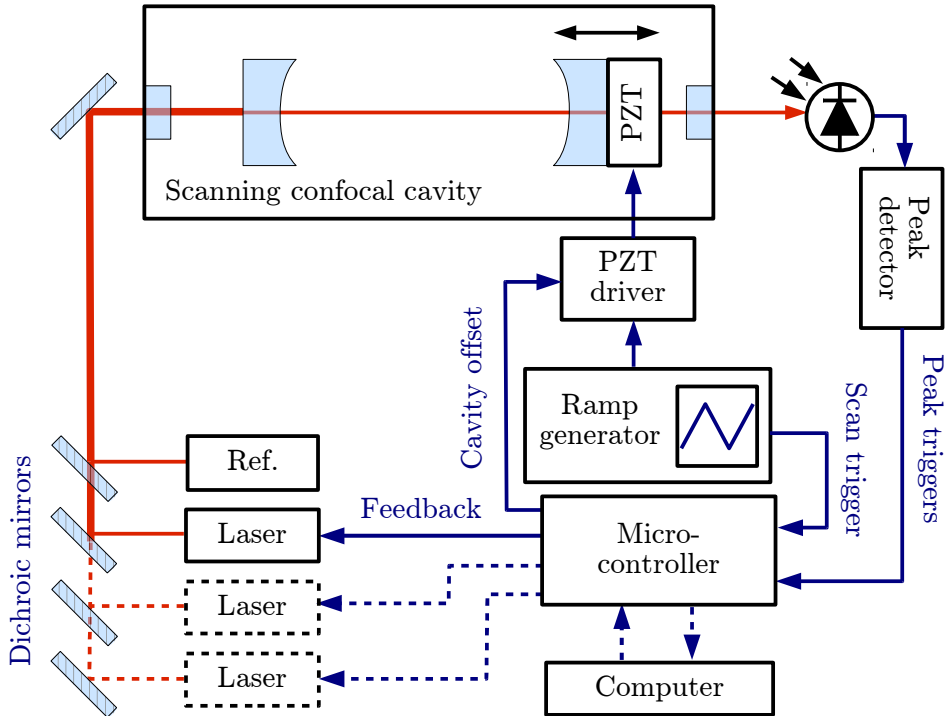

Figure 5.1: Schematic of the scanning cavity offset lock. As the cavity length is scanned, a photodiode detects the optical resonance peaks of the in-coupled lasers. A peak-detection circuit generates the timing signals from which a feedback signal is derived by a fast microcontroller. The computer is used only for monitoring the lock status and setting the lock points.

5.1 Setup

The scanning optical cavity is a confocal Fabry-Pérot resonator with curved mirrors of radius $R = 250$ mm. The confocal condition requires that the mirrors are spaced at distance $L = R$ from each other. Under this condition the frequency of all even and odd transverse modes are degenerate, and the even and odd mode groups are separated by half the free spectral range (FSR). This leads to an effective FSR of $c/4L = 300$ MHz. This degeneracy simplifies the mode-matching conditions for the input lasers and makes the system robust against long-term drifts of their alignment.

The mirrors are coated for a wavelength range of 780 nm - 894 nm with finesse $\mathcal{F}$ between 70 and 120. For scanning and adjustment of the cavity length, one of the mirrors is mounted on a PZT. A ramp generator drives the PZTs via a high current piezo-amplifier, linearly scanning the length of the cavity at a rate of 3 kHz.

Master and slave laser beams are superimposed with dichroic mirrors and polarising beam splitters, and then coupled to the cavity. The cavity transmission intensity is monitored by a photodiode with 10 MHz bandwidth. A schematic of the lock setup is shown in

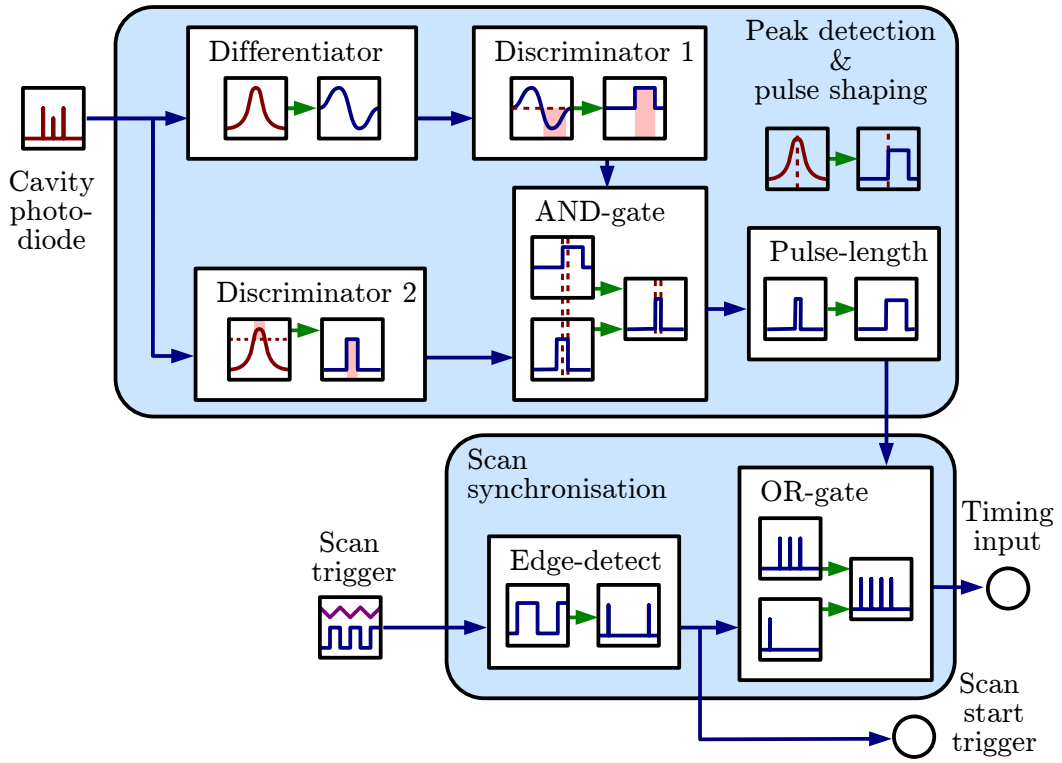

Figure 5.2: Schematic of peak detection circuit. The differentiator and discriminator 1 provide a TTL pulse at the fringe peak. Discriminator 2 suppresses triggering from noise in the wings of the fringe. The microcontroller registers peak times with respect to the start-of-scan trigger.

Fig. 5.1. As the cavity length is scanned over one FSR, a transmission peak is registered for each laser at a cavity length equal to a quarter integer multiple of the laser wavelength. A microcontroller adjusts the frequency of each slave laser so as to maintain a constant distance in the scan between its transmission peak and the peak corresponding to the master laser. In this way, the frequency interval between the two lasers is stabilised and thus the frequency stability of the master laser is transferred to the slave. The target for the interval between the two peaks can be set by the user to lock the slave laser at the desired frequency or scan it over a range of frequencies. The set points are uploaded to the microcontroller via a computer link, which is also used to obtain information on the lock status.

5.1.1 The peak detector

Information on the frequency of a laser is obtained from the time at which a transmission peak occurs in the scan. Peak times are measured using a peak detector that generates a transistor-transistor logic (TTL) pulse at the peak of a transmission fringe. The peak

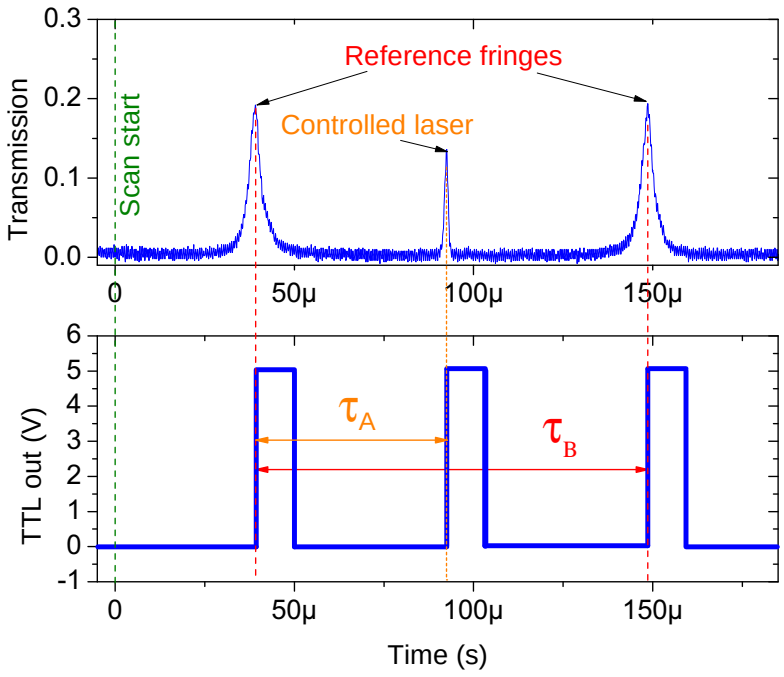

Figure 5.3: Cavity transmission (top) and output of the peak detector (bottom). The ratio τ_A/τ_B is stabilised by feedback to the slave laser frequency control.

detection circuit is outlined in Fig. 5.2. The cavity transmission signal is split into two paths. One path differentiates the output signal of the photodiode to obtain a zero-crossing at the top of the fringe. At the zero-crossing, a TTL pulse is generated via a fast discriminator. In order to suppress laser-noise induced triggering, the second path provides a TTL pulse for a short period before and after the center of the fringe by discriminating at a voltage slightly below the peak. The pulses of the first and second path are combined with an AND-gate, providing a trigger at the peak of the photodiode signal. A monostable multivibrator stage allows the user to adjust the length of the output TTL pulse.

This type of peak detector was chosen due to its robustness with respect to intensity fluctuations of the lasers. A typical transmission signal for two lasers coupled to the cavity, a master and a slave laser, is shown in Fig. 5.3, together with the output of the peak detector.

5.1.2 Feedback control

The pulses generated by the peak detector are referenced to the start of the cavity scan with the help of an edge-detector connected to the trigger output of the ramp generator. The start-of-scan signal is combined with the peak pulses and sent to a low-latency mi-

crocontroller for further processing. The microcontroller measures the arrival times of the pulses by referencing them with its internal clock with a time resolution of 25 ns. When the scan is finished (i.e. the system has registered the expected number of trigger pulses), the microcontroller calculates the time intervals between the peak of the master laser and the peaks of the lasers to be stabilised. In order to account for any change of slope of the ramp over time, the cavity is scanned over a whole FSR and the stabilisation signal is calculated as the ratio of the time τ_A of the slave laser peak and the measured FSR τ of the master laser (Fig. 5.3). The microcontroller calculates a feedback signal designed to minimise the deviation

$$\Delta r = \left| \frac{\tau_A}{\tau_B} - r_0 \right| \tag{5.1}$$

from a user-supplied target ratio r_0. A standard digital proportional, integral, and differential feedback algorithm can be used, and the user can also choose to program their own digital filter for optimal locking. The feedback signal is converted to a voltage using on-board 16-bit digital-to-analog converters and sent to the frequency control of the slave laser.

The number of lasers that can be stabilised in this way is only limited by the number of peaks that can be resolved by the peak detector within one FSR. We have simultaneously stabilised three lasers, with room for at least two more.

5.1.3 Microcontroller programming

A flow diagram outlining the operation of the microcontroller program that records peak detection times and calculates feedback is shown in Fig. 5.4. With reference to this diagram, the program operates as follows:

0. The microcontroller begins and ends in a state of idleness, waiting passively for a trigger from the peak detector.

1. An event is triggered by TTL from the peak detector to the 'Event trigger' input of the microcontroller. Simultaneously one of the on-board counters is incremented in order to keep track of the number of triggers encountered during the scan.

2. A timestamp of the event is read out from the on-board clock and stored into a

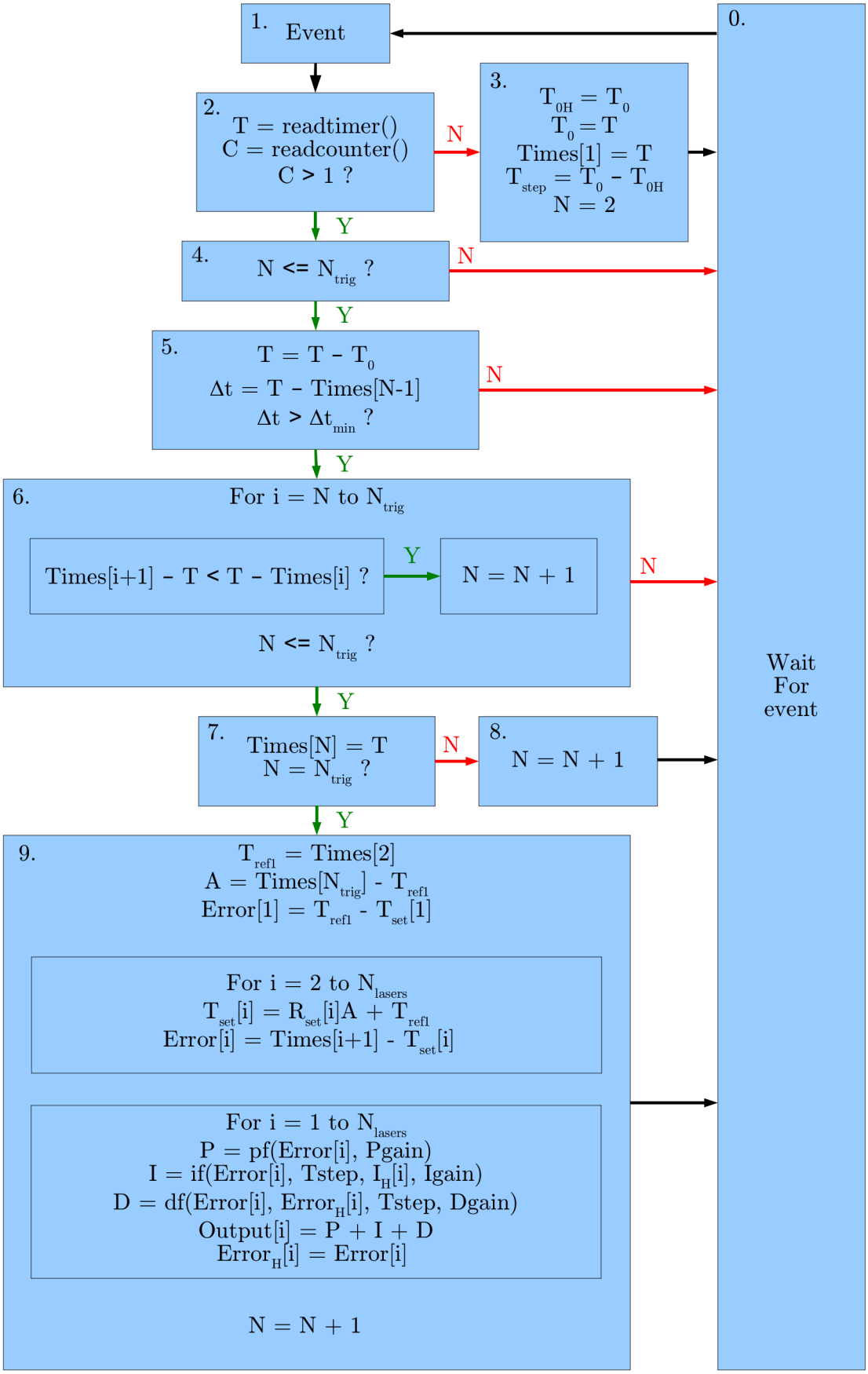

Figure 5.4: Flow diagram of the microcontroller program operation.

variable T. The counter is externally reset to zero at the beginning of every scan (using a purpose counter-reset input on the microcontroller). The trigger counter is read out; If, after incrementing in the latter stage, the counter reads 1 then the counter has just been reset and the event trigger corresponds to the beginning of the scan, and the program progresses to stage 3. If the counter is higher than 1, then the event trigger corresponds to a peak detection event and the program progresses to stage 4.

3. A history variable T_{0H} is used to store the time at which the previous scan started. The new scan start time is stored as the variable T_0 for ease of reading, and in an array that stores the timing of all triggers for use in the feedback algorithms. The time between scans T_{step} is calculated from these values, and a trigger tracking variable N, that independently tracks confirmed (not erroneous) event triggers, is set to 2, pre-empting the next event trigger.

4. The trigger counter indicates that this event is not the 'start of scan' trigger. The trigger tracking variable N is checked: If the value is less than the expected total number of triggers for a single scan $N_{trig} = N_{lasers} + 2$, then the program progresses to stage 5. Otherwise the trigger is assumed to be a peak encountered on the reverse direction of the scan. The microcontroller ignores such triggers and returns to state 0. and begins to wait for the next trigger or start of scan.

5. The event is assumed to be a peak detection trigger. The time since the start of the scan is calculated. If the time since the last peak detection trigger Δt, is less than a user-set value Δt_{min} (approximately the time taken to pass over a single peak in the scan), then it is assumed that the system has 'double-triggered' on a single peak due to photodiode or laser noise. The event is ignored, the microcontroller returns to state 0 and continues to wait for the next trigger or start of scan.

6. The event trigger time is checked against all of the recorded times of peak triggers in the last scan of the system. If the trigger time is closer to the peak timing of a different peak in the last scan, it is assumed that the peak that was expected has been blocked or otherwise disengaged from the scanning cavity system. The trigger tracking variable N increments in order to assume the value of the closest peak during the last scan. In practice this is a working safeguard against unexpected

beam blockages that allows the scanning cavity lock to continue locking those lasers that are still coupled to the cavity, whilst maintaining feedback to the blocked beams for their last known offset. If, after these checks N is still less than the expected number of peak triggers, then the program progresses to stage 7. Otherwise the microcontroller returns to state 0 and waits for the next trigger or start of scan.

7. The time of this event is stored in the iterable array of confirmed trigger times $Times[]$. If the event is the final expected event in the scan (the second reference peak), then the program progresses to stage 9. Otherwise the program progresses to stage 8.

8. The trigger tracking variable N is incremented by one, representing a single confirmed and recorded peak trigger time.

9. The time of the last trigger is subtracted from the time of the first reference trigger. This value is τ_B in Fig. 5.3. Error values for each peak trigger are calculated, representing the deviation of the trigger timing from a user set time or ratio with regards to the value τ_B. Feedback voltages are calculated for each laser using digital proportional, integral and differential functions, and applied to the on-board DACs outputs. All of the error values are then stored in a history array $Error_H[]$ for calculation of the next set of feedback voltages. The trigger tracking variable N is reset to 1, and the microcontroller returns to state 0, waiting for the next start of scan.

Some initialisation of history variables is required for the first scan of the system, and there are facilities for resetting DAC outputs and re-initialising history variables in the event of an un-checked error.

5.1.4 Scanning frequency

The frequency f_s of the triangular cavity ramp determines the feedback bandwidth of the system. Every scan of the cavity transmission produces a snapshot of the laser frequencies. The scanning frequency is therefore the limit of the rate at which information on the lasers' behaviour is gathered. According to the Nyquist sampling theorem, in ideal conditions this allows us to probe laser noise at frequencies less than $f_s/2$. Furthermore, the feedback

signal derived from this information can only be effective at frequencies below $f_s/4$, where noise at that frequency undergoes a 90° phase shift during the sample-to-feedback interval.

A well controlled laser lock therefore requires that f_s should be significantly higher than the highest frequency component of the noise spectrum of the laser that we wish to reduce.

The frequency resolution Δf of the digital system implemented here is limited by the time resolution Δt =25 ns of the microcontroller (see section 5.2.1) and the speed of the scan:

$$\Delta f = 2 \text{ SR } \cdot f_s \cdot \Delta t, \tag{5.2}$$

where SR =330 MHz is the scanning range, chosen to be slightly larger than one FSR. The factor of 2 in Eq. (5.2) is due to the fact that only the scan in the upward direction is used for evaluating the peak positions. In this way complications resulting from hysteresis of the PZTs are avoided. In this implementation of the lock, a scan frequency of 3 kHz was used to achieve Δf =50 kHz laser frequency resolution and a bandiwdth of 380 Hz.

5.1.5 Drift compensation

Transferring frequency stability from master to slave lasers requires keeping the ratio of time intervals τ_A/τ_B constant. Absolute changes of the refractive index, together with the thermal expansion of the cavity, may lead to a drift of the optical path length large enough to shift the monitored resonances out of the scan range. To avoid this, we stabilise the cavity length with respect to the master laser.

We achieve this by measuring the time between the start of the scan and the first peak of the master laser and keeping it constant by feeding back a variable DC offset to the PZT-mirror assembly. During the course of a day, this DC offset may change by tens of volts. Care must be taken not to let the DC offset grow too large, as in this case the linearity of the PZT ramp may be affected. However, with a maximum thermal drift of the cavity of 5 MHz/h this has not been a problem.

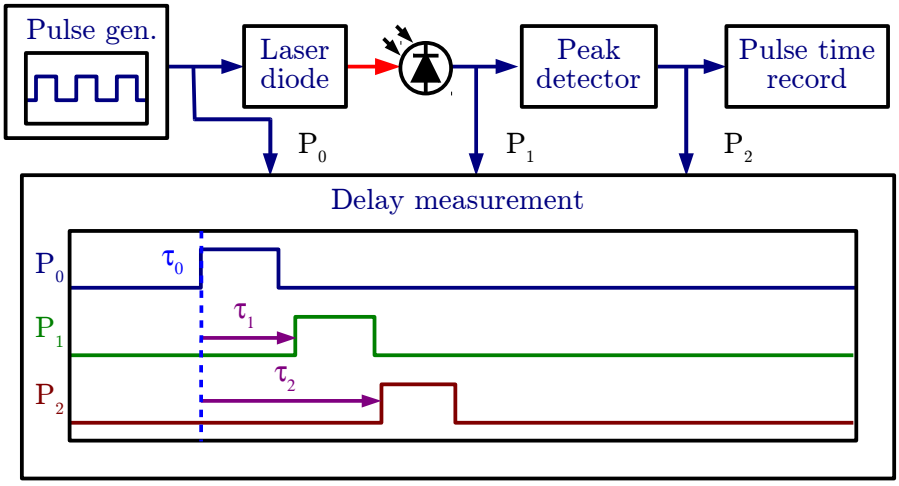

Figure 5.5: Setup for the measurement of timing accuracy. The peak detector analyses periodic pulses from a laser diode, registered by a photodiode. The variance of pulse times at different points in the system is measured by an oscilloscope.

5.2 Test of System Performance

5.2.1 System timing accuracy

An attribute of fundamental importance for the performance of the system is the accuracy of timing the appearance of cavity transmission peaks. To measure this property independently of laser frequency noise, the cavity photodiode is directly fed periodic pulses of constant amplitude from a laser diode controlled by a pulse generator. The corresponding test setup is illustrated in Fig. 5.5.

The pulse signal is monitored before and after the peak detector and the time delay with respect to the initial pulse is measured by an Agilent oscilloscope's [37] delay measurement function as shown in Fig. 5.5. The variance of the measured delay times is a measure for the timing uncertainty.

The jitter of the detected peak times was measured to be around 10 ns, which is a factor of 2.5 smaller than the timing resolution of the micro-controller system. Thus the timing accuracy Δt used in Eq. (5.2) is, indeed, limited by the clock speed of the micro-controller, rather than the peak detection circuit.

5.2.2 Feedback bandwidth

An important measure of lock performance is the feedback bandwidth. It determines the upper limit of noise frequencies that can be effectively suppressed by the system.

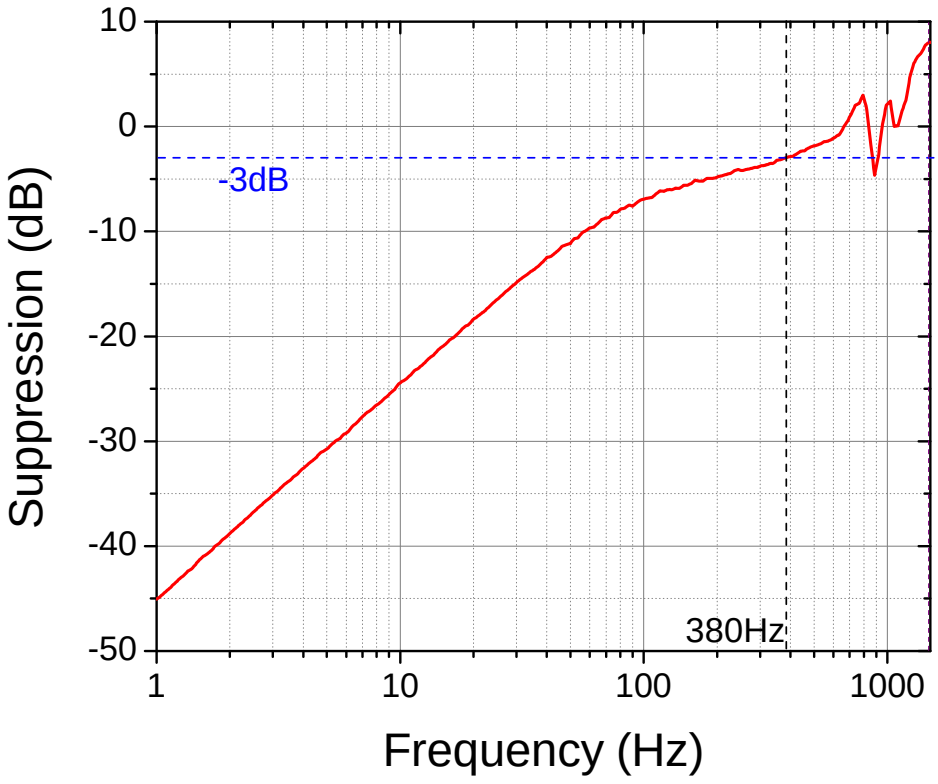

Figure 5.6: Measurement of lock gain as a function of frequency, from 1 Hz to 1.5 kHz (half the scanning frequency).

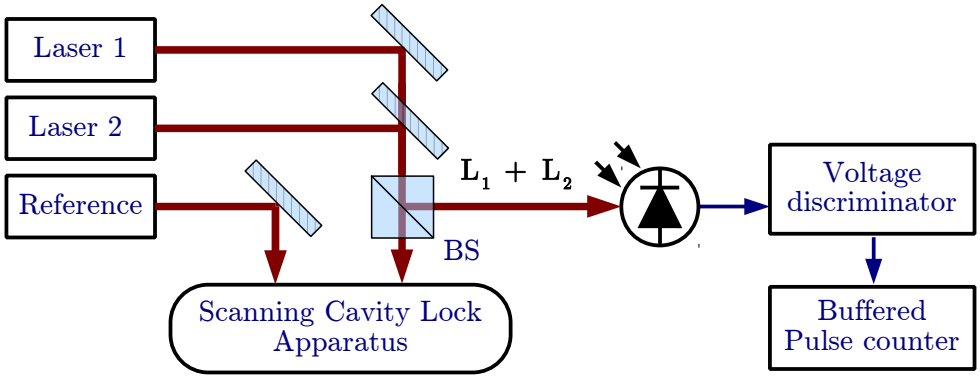

Figure 5.7: Schematic of the setup for beat note measurement. Lasers 1 and 2 are independently locked to the reference laser via the scanning cavity. Part of the of the overlapped beam is picked off for the beat note frequency measurement.

Figure 5.6 shows a measurement of the noise suppression as a function of frequency. It was obtained by sinusoidally modulating the frequency control of the locked slave laser. The modulation frequency is swept and the error signal is monitored by a frequency response analyser [38]. The same analysis is applied to the unlocked laser in order to measure the response of the laser frequency control. The suppression of external influences provided by the stabilisation system is the ratio of the locked and unlocked responses, and is shown in Fig. 5.6. The data shows a -3 dB bandwidth of 380 Hz, with noise suppression of -45 dB at a noise frequency of 1 Hz.

5.2.3 Stability

In order to characterise the stability of the locked system over a range of timescales, we measured the Allan deviation [39] $\sigma(\tau)$. Figure 5.7 illustrates the setup used to measure the stability of the locking system. The beams from two identical lasers (laser 1 and laser 2) with frequency difference Δ are overlapped and independently locked to the reference laser using the scanning cavity lock. A fraction of the overlapped beams is picked off by a beamsplitter and directed onto a photodiode. The resulting beat note is measured using a fast voltage discriminator and buffered pulse counter.

Through the beat note frequency, we obtain a measure of the relative frequency stability of lasers 1 and 2. As both lasers are identical and independently locked to the reference, the stability of each slave laser relative to the master laser is expected to be better by a factor of $\sqrt{2}$. Figure 5.8 shows the Allan deviation of the beat note measured for two lasers with an offset frequency of about 30 MHz, locked to a reference laser stabilised to

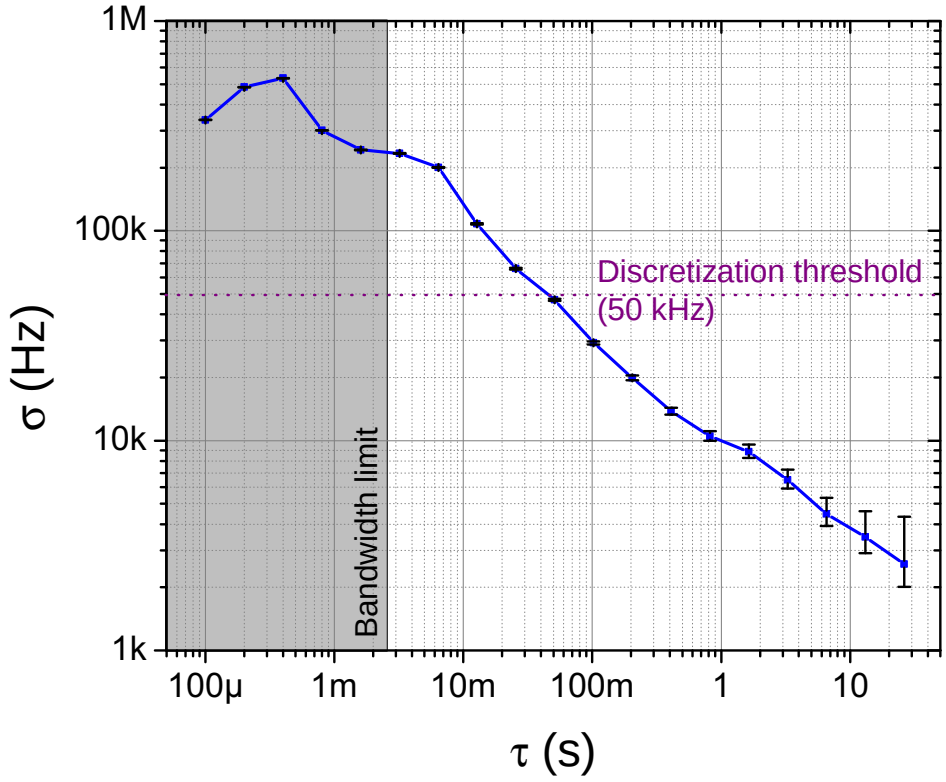

Figure 5.8: Allan deviation σ of beat note frequency measurements for two lasers independently locked to the scanning cavity with an offset of 30 MHz.

the caesium D_1-line.

The grey region of the graph is outside the $-3\ dB$ bandwidth of the lock (see section 5.2.2). At time scales longer than τ ~50 ms, the stability is improved to deviations below the frequency resolution Δf of the micro-controller given by Eq. 5.2 (the "discretization threshold" ~50 kHz). This is due to long-term stochastic averaging of noise on the error signal. At times longer than 1 second, the Allan deviation drops below 10 kHz.

This measurement represents the ultimate achievable performance of the system, as the two lasers are at (almost) the same wavelength, and therefore unaffected by environmental refractive index changes.

5.3 Updates

Since the measurements in section 5.2 were taken, the design of the scanning cavity has been modified in order to improve performance. The previous iteration of the cavity used an invar spacer of fixed length, designed to hold the mirrors in place at the confocal

condition. However, machining tolerances and the thickness of spacers used to compensate for these tolerances can leave the cavity slightly non-confocal. This lifts the degeneracy of higher order modes by a small amount, effectively broadening the linewidth of the cavity.

To avoid this problem, the cavity spacer has been split into two pieces that are screwed together using an ultra-fine threaded bore and screw combination. Careful adjustment of the cavity length in order to minimise the linewidth results in a significant improvement of the finesse of the cavity from 120 to 220.

Compensation for long-term cavity length drift can cause the scanning piezo to run up against its voltage limit. In this case the scanning cavity can malfunction, as the scan becomes distorted or clipped. For this reason a second piezo has been installed into the system. The piezo is placed behind the second mirror, and the feedback that stabilises the cavity cavity length with respect to the master laser is handled by it.

The quality of lock to the master laser depends on the differential change of the intra-cavity refractive index for the slave laser with respect to the master laser [40]. In order to be totally independent of environmental fluctuations such as air pressure, temperature, and humidity, the scanning cavity can be operated in vacuum, in particular for slave lasers with substantially different wavelengths. In this particular implementation however, all lasers are in the near infra-red, and so the system has not been placed under vacuum.

Chapter 6

The experimental cavity

The high-Q optical cavity used for this experiment has a length of 7 mm and mirrors with radius of curvature $r = 1$ cm. The mirrors have a transmissivity of 5 ppm and 150 ppm at 866 nm. This forms an asymmetric cavity so that photons exit the cavity in the direction of the higher transmissivity mirror with a probability of 96 %. The finesse is $\mathcal{F} \sim 10,000$, and thus, the cavity decay rate is $\kappa = 1.0 \cdot 2\pi$ MHz. The TEM_{00} mode waist size is $w_0 = 36$ μm. The configuration is deliberately non-confocal, so that we can be sure to have several non-degenerate higher order cavity modes with which to lock the cavity length so that it is resonant with the ions. The mirrors were chosen to address the near infra-red transition of the ion (as opposed to the UV) because scattering losses in the substrate are lower in the infra-red spectrum, resulting in higher quality mirrors.

The calculated cavity-ion coupling parameter $g = 1.1 \cdot 2\pi$ MHz, at the centre of the cavity mode, is of the same order as the cavity decay, but smaller than the rate of spontaneous emission from the $P_{1/2}$ state of the ion, $\Gamma = 22.3 \cdot 2\pi$ MHz. This intermediate coupling regime is sufficient for single photon generation using a cavity-assisted Raman transition, and for probabilistic entanglement.

6.1 Ion-cavity overlap

In order to optimise the rate of coherent interactions between the ion and the cavity field, optimal overlap between the ion and the cavity mode is essential. The coupling g is dependent on the mode function of the resonant field (Eqn. 2.42): for optimal coupling the ion or ion string must be overlapped with the maximum of the transverse field mode.

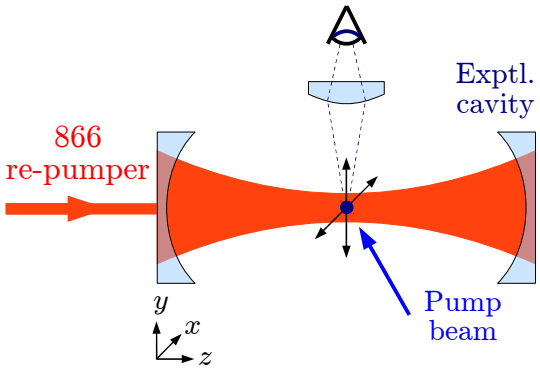

Figure 6.1: Scheme for optimising cavity-ion overlap using cavity-field repumping. The cavity field is probed by observing fluorescence as the ion/s are moved in the x-y plane.

The trap machining process and the cavity mounting methods give us a good chance to be well overlapped from the outset, but some further optimisation of the overlap is also necessary after initial trapping.

If the initial overlap is good, the coupling can be optimised by looking directly at cavity-assisted photon emission rates, but if the ions are too far from the cavity centre then the rate of photons may be too small to measure. The simplest way to optimise the coupling when the ions are further from the cavity centre is by repumping the ions using the field generated inside the cavity by a laser tuned to the repumping transition and coupled to the TEM_{00} mode (see Fig. 6.1). Since the intensity of the field inside the cavity is also proportional to the mode function (equation 2.36), moving the ions into the region of the cavity with the strongest repumping intensity effectively optimises the ion-cavity coupling. The region of highest intensity can be determined by looking at the cooling fluorescence from the ions as a function of position.

6.1.1 Cavity-mode repumped ion-fluorescence profile

In order to locate the center of the cavity intensity distribution from ion fluorescence, we must first take into account the effects of the cavity enhanced intracavity field on the ion's cooling transition. Figure 3.11 shows the level diagram of $^{40}Ca^{+}$ for reference. If only the cooling laser ($S_{1/2} \rightarrow P_{1/2}$) is on, the ion will eventually decay to $D_{3/2}$ (with a branching ratio of 1:12) and be shelved for the lifetime of this meta-stable state ($\tau \sim 1$ s), causing fluorescence and cooling to end. Thus a repumper field is employed to recycle the population into the cooling transition states.

Because of the build up of the light field inside the high-Q resonant cavity, the intensity of in-coupled light is greatly enhanced within the cavity mirrors. The intensity of the intracavity field I_{cav} is determined by the reflectivity and absorption losses, R_i and A_i of the mirrors M_i (see Fig. 2.4). For our cavity arrangement the steady-state intensity of the resonant intracavity field is given by

$$I_{cav} = \frac{2T_1}{(T_1 + T_2 + A)} I_0, \tag{6.1}$$

where I_0 is the intensity of the light at the input mirror, $T_i = 1 - R_i$, $i = 1, 2$ are the transmissivities of the mirrors and $A = A_1 + A_2$ are the total absorption losses. Assuming absorption losses of 5 ppm per mirror (quoted by the manufacturer), the resonant intracavity field is enhanced by a factor of 19,000. With such a high intensity of repumper light in the cavity, we must be sure to take into account its effects on the populations of the cooling transition states.

The rate-equation model provides a simplified set of equations used to describe the system and calculate the population of the $P_{1/2}$ state. Since cooling fluorescence results from spontaneous decay of the $P_{1/2}$ state, the rate of fluorescence is determined by the population of this state. In this model the rate equations for the S and D states are

$$\frac{d\sigma_1}{dt} = T_{13}(\sigma_3 - \sigma_1) + \Gamma_{31}\sigma_3, \tag{6.2}$$

$$\frac{d\sigma_2}{dt} = T_{23}(\sigma_3 - \sigma_2) + \Gamma_{32}\sigma_2, \tag{6.3}$$

with subscripts $1 \rightarrow S_{1/2}$, $2 \rightarrow D_{3/2}$ and $3 \rightarrow P_{1/2}$, σ_i are the populations of the state, T_{ij} are the transition probabilities between states $i \rightarrow j$ and Γ_{ij} are the spontaneous decay rates. The steady state solution for the population of the $P_{1/2}$ state is [41]

$$\sigma_3 = \frac{1}{3 + \Gamma_{31}/T_{13} + \Gamma_{32}/T_{32}}. \tag{6.4}$$

From this equation we can already see that adding a third level reduces the maximum population of the $P_{1/2}$ state from $\frac{1}{2}$ (two-level system) to $\frac{1}{3}$, reducing maximum fluorescence. With the transition probabilities from the semi-classical treatment of the atom-light

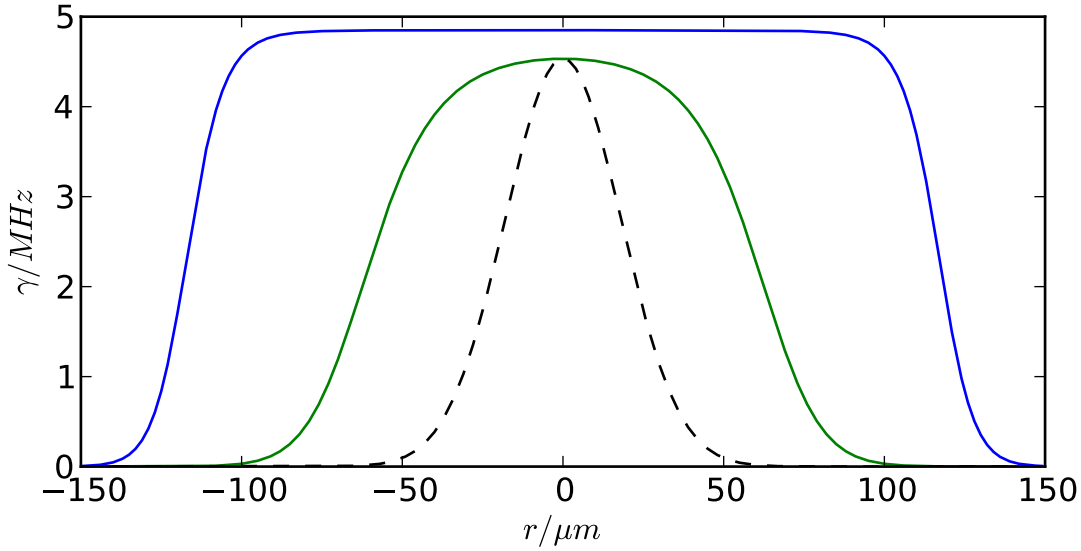

Figure 6.2: Theoretical cavity fluorescence profile as a function of distance r from the centre of the cavity mode using the rate equation model for a three level system. The dashed black line shows the cavity intensity profile. The green and blue lines show successively more saturated fluorescence profiles from higher cavity repumper intensities.

interaction

$$T_{13} = \frac{\Omega_C^2 \Gamma}{4\Delta_C^2 + \Gamma^2}, \tag{6.5}$$

$$T_{23} = \frac{\Omega_R^2 \Gamma}{4\Delta_R^2 + \Gamma^2}, \tag{6.6}$$

the population of the $P_{1/2}$ state becomes

$$\sigma_3 = \frac{\Omega_R^2(1+k)}{4\Delta_R^2 + \Gamma + 3(1+k)\Omega_r^2 + k(4\Delta_C^2 + \Gamma^2)\Omega_R^2/\Omega_C^2}, \tag{6.7}$$

where Ω_R and Ω_C are the Rabi frequencies of the repumping and cooling transitions respectively, Δ's are laser detunings from resonance, $\Gamma = \Gamma_{31} + \Gamma_{32}$ and $k = \Gamma_{31}/\Gamma_{32}$. The rate of cooling fluorescence γ is given by $\Gamma_{31}\sigma_3$. The cavity mode fluorescence profile that we would expect using this model is shown in Fig. 6.2 for different values of the cavity field intensity. The profile shows a broadening 'plateu' of fluorescence intensity caused by increasing saturation of the $P_{1/2}$ state.

However, this model does not include mixed quantum states and coherences. In order to predict the dynamics of the state populations more accurately, we must use the density matrix and the optical Bloch equations. The three level Bloch equations lead to the

result [41]

$$\rho_{33} = \frac{4(\Delta_C - \Delta_R)^2 \Omega_C^2 \Omega_R^2 \Gamma}{Z}, \tag{6.8}$$

where ρ_{33} is the population of the P state, and

$$\begin{aligned} Z \equiv\ & 8(\Delta_C - \Delta_R)^2 \Omega_C^2 \Omega_R^2 \Gamma + 4(\Delta_C - \Delta_R)^2 \Gamma^2 Y \\ & + 16(\Delta_C - \Delta_R)^2 [\Delta_C^2 \Omega_R^2 \Gamma_{31} + \Delta_R^2 \Omega_C^2 \Gamma_{32}] \\ & - 8\Delta_C(\Delta_C - \Delta_R)\Omega_R^4 \Gamma_{31} + 8\Delta_R(\Delta_C - \Delta_R)\Omega_C^4 \Gamma_{32} \\ & + (\Omega_C^2 + \Omega_R^2)^2 Y, \end{aligned} \tag{6.9}$$

$$Y \equiv \Omega_C^2 \Gamma_{32} + \Omega_R^2 \Gamma_{31}. \tag{6.10}$$

Equation 6.8 immediately highlights a phenomenon known as the 'two-photon', or 'dark' resonance, under the condition $\Delta_C = \Delta_R$. Under this condition the population of the $P_{1/2}$ state is zero and thus the rate of fluorescence and cooling is zero. Importantly for the case of very strong repumping fields, the width of this resonance is dependent on the repumper intensity, as illustrated in Fig. 6.3; a theoretical cooling fluorescence spectrum of the three-level system in $^{40}Ca^{+}$, for variable cooling laser detuning Δ_c, variable repumper Rabi frequency (green and blue lines), and fixed repumper detuning of Δ_R = -10 MHz.

At high repumper intensity, power broadening of the repumping transition causes broadening of the two-photon resonance to the point where it can overlap with the cooling laser resonance, and can reduce or entirely suppress fluorescence and cooling. Figure 6.4 illustrates the effect of increasing repumper Rabi frequency for an ion cooled with fixed Δ_C and Ω_C, showing the eventual decrease in fluorescence at high Ω_R. The amount of intensity inside the high finesse optical cavity used in our experiment is sufficient to observe this effect.

The revised cavity fluorescence profile – including the dynamics of the dark-resonance – is shown in Fig. 6.5, for different values of the cavity intensity. Here we can see that for a sufficiently intense cavity field we have close to zero fluorescence in a large region surrounding the cavity mode centre, as the dark resonance broadens to overlap with the cooling laser detuning.

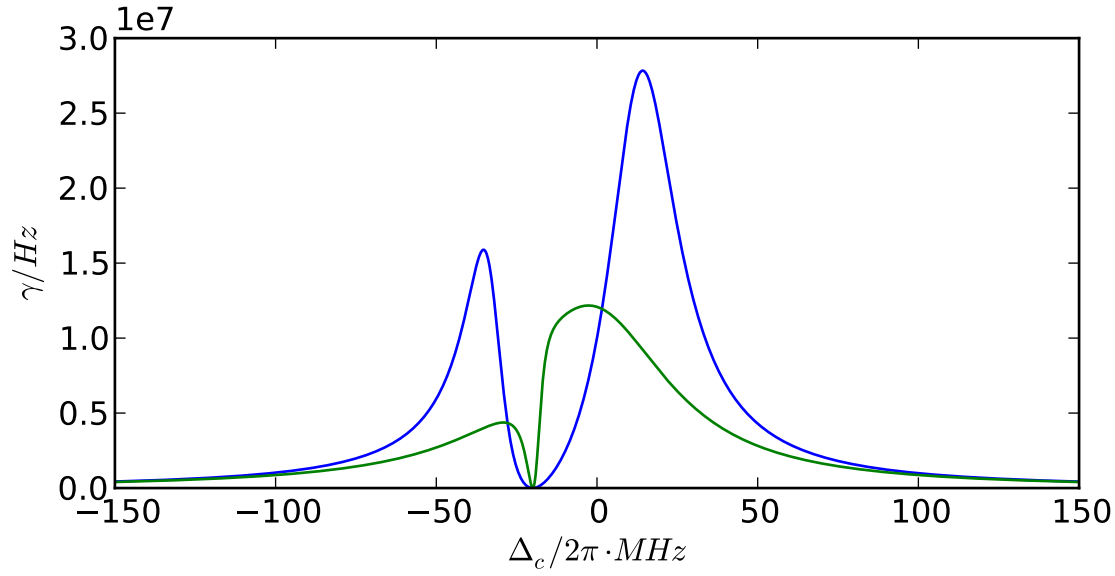

Figure 6.3: Theoretical cooling fluorescence spectrum of the $^{40}Ca^{+}$ lambda-type level system. The green and blue lines represent spectra at different repumper intensities ($\Omega_R = 4.2 \cdot 2\pi$ MHz and $\Omega_R = 42 \cdot 2\pi$ MHz respectively). The two-photon resonance is seen to widen for the higher intensity.

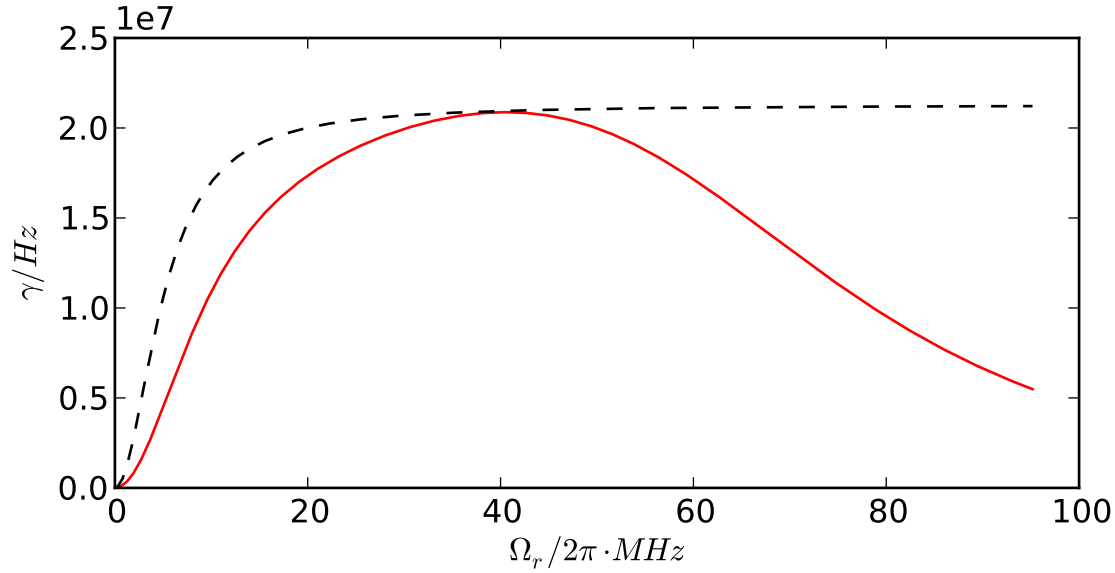

Figure 6.4: Ion fluorescence as a function of repumper Rabi frequency using the three-level optical Bloch equations (Eqn 6.8) for fixed cooling laser detuning. The black dashed line represents the fluorescence for the rate equation model (Eqn 6.4).

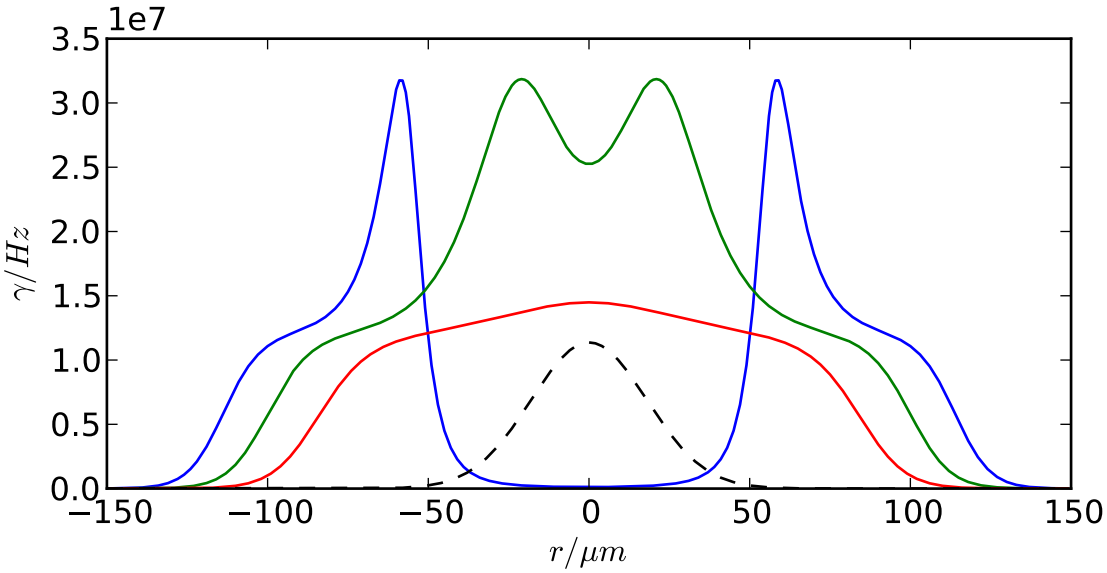

Figure 6.5: Theoretical cavity fluorescence profile as a function of distance r from the centre of the cavity mode for variable, large cavity repumper Rabi frequency and fixed cooling laser detuning. The red line ($\Omega_R = 92 \cdot 2\pi$ MHz) shows the saturation effects. The green line ($\Omega_R = 290 \cdot 2\pi$ MHz) shows a fluorescence dip due to the broadened two-photon resonance effect. The blue line ($\Omega_R = 920 \cdot 2\pi$ MHz) shows the flattened fluorescence profile we expect from typical Rabi frequencies encountered in the cavity. The dashed black line shows the cavity intensity distribution.

6.1.2 Cavity-ion overlap in the horizontal plane

With knowledge of how the intensity of cavity repumper field effects the fluorescence of the ions, we can use medium sized three-dimensional crystals to probe the cavity field and locate the centre of the mode. The crystals can be moved using the micromotion compensation electronics, or by adjusting the position of the rf-centre of the trap.

For this measurement, we repump only with the cavity mode, and move the crystal away from the trap centre in the horizontal plane. The optics used for coupling a repumper laser to the cavity are shown in Fig. 6.6. As predicted in the previous section, we observe higher fluorescence and thus more stable ions in the wings of the cavity mode. This works in both directions, as we would expect due to the radial symmetry of the cavity field. Figure 6.7 shows an ion crystal trapped in the region of stability away from the rf-centre of the trap ($y = 250\mu$m), and the less stable ion cloud that results from trapping near the cavity centre, where the two-photon resonance effect dominates over fluorescence.

As we move the crystal further it passes over the peak in brightness and the fluorescence sharply drops again. Figure 6.8 shows another pair of crystals moved to these regions on either side of the cavity mode. We can use these bands of peak fluorescence to estimate

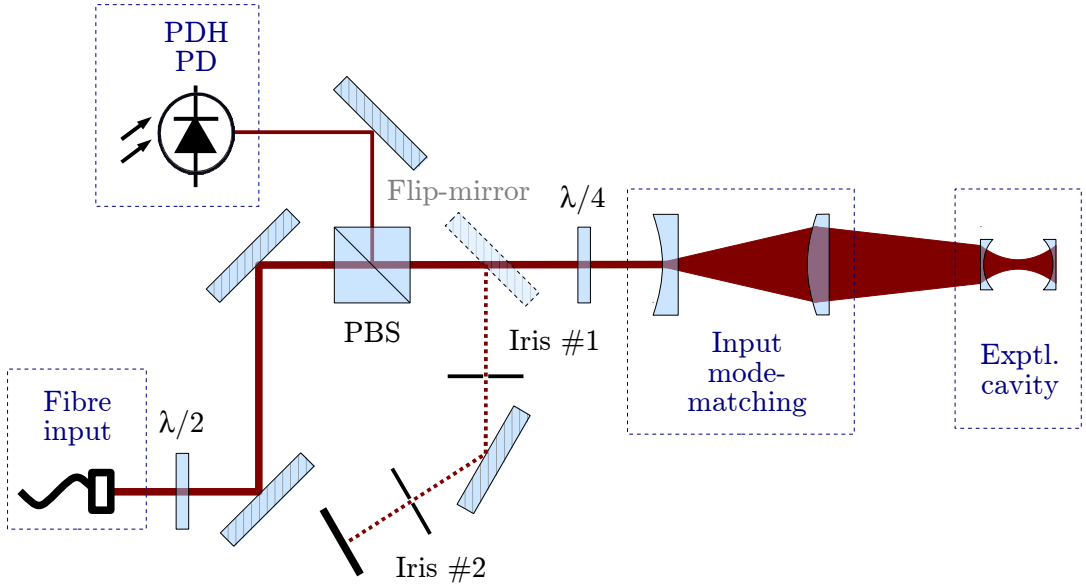

Figure 6.6: Optical setup for the experimental cavity laser input. This setup allows the cavity to be locked to either 866 nm laser for cavity field ion repumping, or Cs reference locking (section 6.3), using the PDH technique. Mode-matching lenses give optimal cavity coupling of the input laser to the cavity mode. A retractable flipper mirror allows for quick re-alignment to the cavity mode by directing the beam through a pair of iris pin-holes.

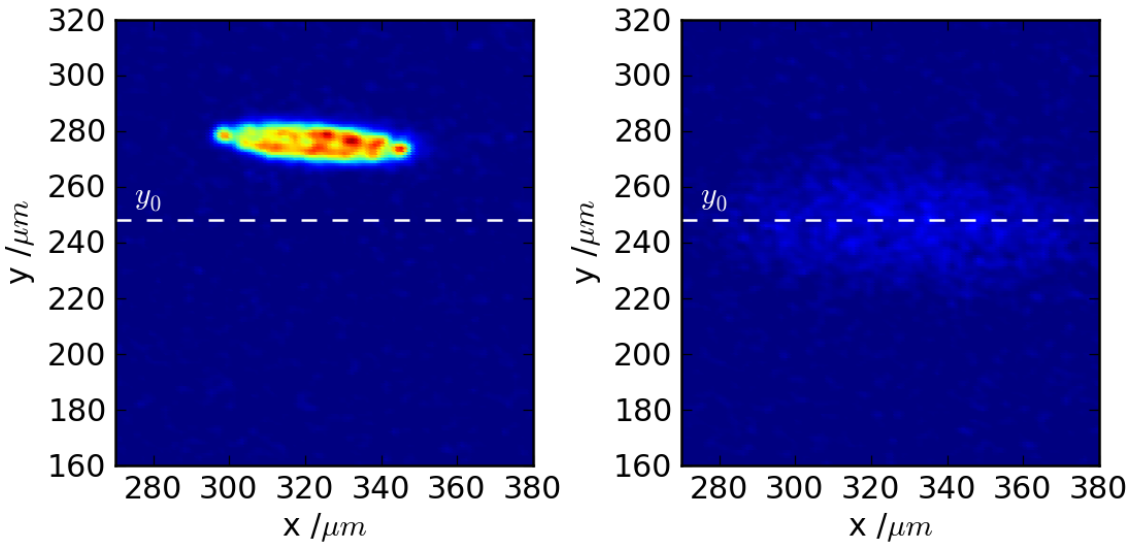

Figure 6.7: Ion crystal trapped away from the rf-centre ($y_0 = 248$ μm) (left). The crystal has been moved using the micromotion compensation voltages to the region of brightest fluorescence. When trapped close to the rf centre the crystal is unstable and becomes a diffuse cloud (right) due to two-photon resonance effects caused by the cavity mode. This indicates the cavity mode is close to the rf-centre in the horizontal plane.

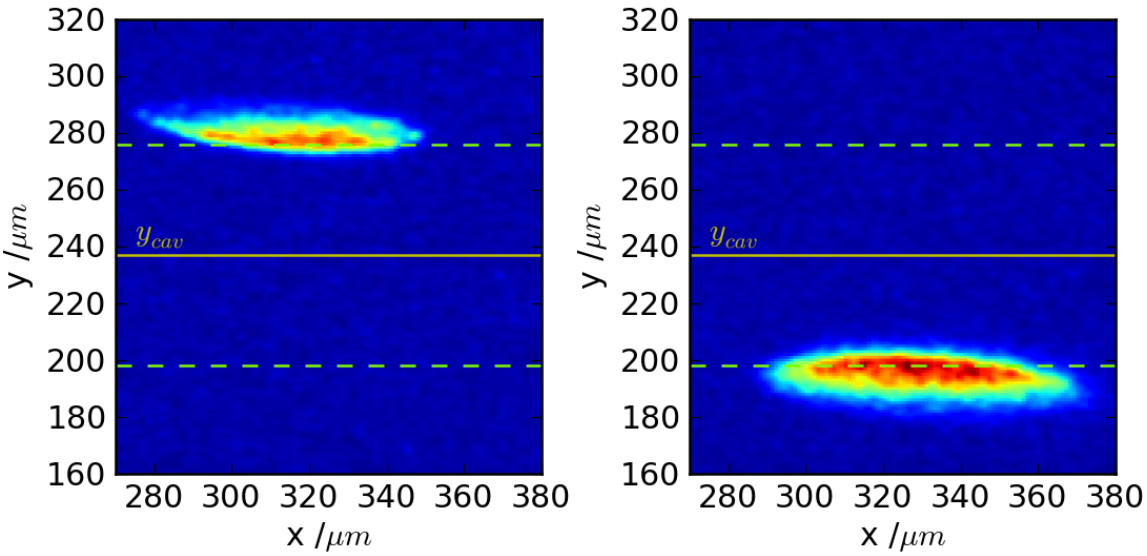

Figure 6.8: Ion crystals trapped further out from the rf-centre and cavity axis in both directions. We see a distinct drop of fluorescence within the boundary of the crystal. The regions where this drop occurs, marked by red dashed lines, frame the centre of the cavity mode in the horizontal plane ($y_{cav} \sim 237$ μm).

the position of the centre of the cavity mode, then manually move the rf-centre of the trap so that the ions overlap optimally with the cavity in this plane.

The data shown in Fig. 6.8 indicates that the psuedopotential is close to being well overlapped with the cavity mode in the horizontal plane. After moving the rf-centre of the trap to the centre of the cavity mode, we predict that the ions are overlapped within 5 μm of the cavity centre, based on an estimate of the accuracy of determining the brightest point of the crystal fluorescence. Further optimisation of the overlap is expected from observation of cavity-assisted photon emission rates.

Although some of the parameters during this measurement are not well known (most notably the mode-matching of the external cavity input beam to the cavity mode, and the cavity absorption losses), we can make some estimates in order to fit the theoretical curves described in section 6.1.1 to the peak intensity of the ions in crystals trapped at different distances from the cavity centre. A potential theoretical fit to the power inside the cavity mode is shown in Fig. 6.9, implying a cavity field Rabi frequency of $\Omega_R = 460 \cdot 2\pi$ MHz, and cavity mode coupling efficiency of roughly 20 %, for $\Delta_R = 0$, $\Omega_C = 90 \cdot 2\pi$ MHz, $\Delta_C = 140 \cdot 2\pi$ MHz, and the given values of T_n and A of our cavity.

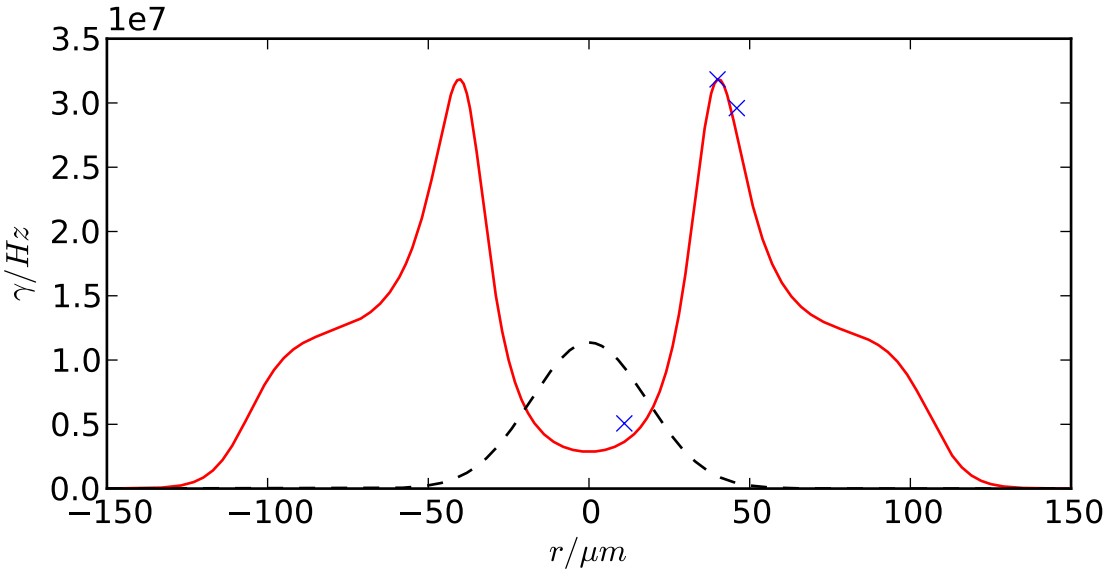

Figure 6.9: A theoretical fit to maximum crystal intensity data implying $\Omega_{cav} = 460 \cdot 2\pi$ MHz. Inherent instability of crystals in this strong repumping regime made it difficult to take large sets of data for crystals with constant ion number.

6.1.3 Cavity-ion overlap in the vertical plane

Looking for fluorescence changes and saturation effects in the vertical plane (parallel to the line of sight of the camera), is more involved than looking in the horizontal plane. A significant problem with using the micromotion compensation voltages to move the ions and probe the cavity field is that a crystal will not remain stable when moved in the vertical direction by more than a 0.3 V change in V (defined in section 3.1.5). By comparison, a crystal can be moved by the full 10 V of the DACs in the horizontal direction without de-crystallising into a cloud. The reason for this instability is Doppler broadening of the cooling transition as micromotion in the direction of the cooling beam increases (the direction of micromotion oscillation is perpendicular to the electric field from the compensation voltages). This broadening causes trapping instabilities and ultimately rules out the use of micromotion compensation voltages for the cavity mode search in the vertical direction.

This leaves the variable rf-capacitors to move the rf-centre of the trap, and with it the stable crystal, in order to find the overlap with the cavity in the vertical direction. However, a complication of using this method to observe the saturation effects described in the previous section is that it is difficult to keep stability of crystals during adjustment of the rf capacitors – changing the capacitance changes the resonance frequency of rf-

resonator circuit so that the trapping field is no longer resonantly driven. This causes the depth of the pseudopotential to fall rapidly until the driving frequency is adjusted to the new resonance. Furthermore, one must make sure that significant ion movement in this plane is compensated by re-focussing the camera as well as redirecting the cooling and repumping beams to track the crystal position.

These factors, combined with weak cooling caused by the intense cavity field close to the centre of the mode means that frequent reloading and optimisation are required, causing this method to become un-feasible.

Luckily, we can avoid these problems and bypass the strong cavity field effect by repumping with both the cavity and a relatively weak free-space beam, pointing at an angle to the cavity mode. This generates fluorescence from the ion at a background level equal to the fluorescence from free-space repumping only, plus a level that is approximately proportional to the cavity intensity. This effect was discovered only after the measurements made in the latter section. It's not entirely clear where this effect originates, but it could be linked to the fact that the model used in section 6.1.1 does not take into account the Zeeman sub-levels of the system. Since the cavity repumper has fixed polarisation, two-photon dark resonances will likely occur between specific Zeeman sub-levels of the $S_{1/2}$ and $D_{3/2}$ states. The weak free-space repumper, with a different polarisation and orientation to the cavity field, could act as another stage of repumping, releasing the population from non power-broadened sub-levels populated via spontaneous emission from the $P_{1/2}$ state.

The fluorescence data shown in Fig. 6.10 are readings taken using this 'double-repumping' method, using the rf capacitors to move the ion crystal in the vertical direction. The peak fluorescence of small, fixed-number ion crystals trapped at different positions in the vertical plane are plotted against the trap resonance frequency for those positions. The distance moved by the ions for a given change in resonance frequency is approximated as linear for small deviations from the natural rf centre. By moving the crystal in the plane of the camera it is estimated that to move the crystal 46 μm one must change the rf frequency by 1 MHz.

The data outlines an approximately Gaussian distribution of fluorescence, centered slightly out from the natural rf centre of the trap, with width $w = (42 \pm 10)$ μm. This is close enough to the estimated cavity waist $w_{cav} = 36\mu$m to assume that the cavity mode shape is the major contribution in this fluorescence profile. The change in rf frequency

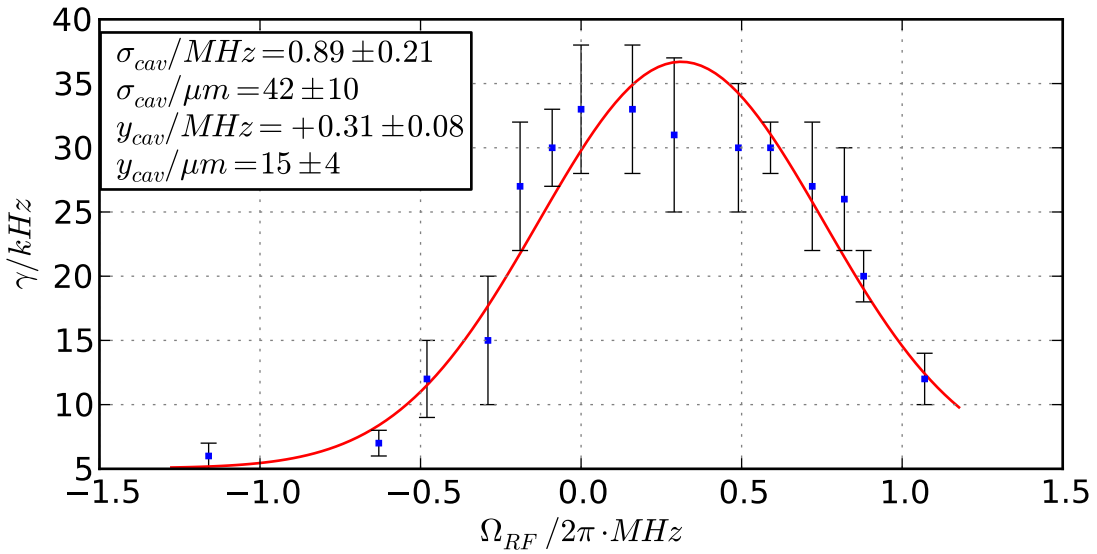

Figure 6.10: Peak fluorescence γ of ion crystals trapped in different positions in the vertical plane of the cavity mode. Ω_{rf} is the trap resonance frequency reading at those positions in the vertical plane, determined by rf resonator capacitors used to move to move the ions. A Gaussian profile has been fit to the data (red). The values for σ_{cav} and y_{cav} are deduced from measurements of rf displacement vs. resonator frequency.

was used to estimate that the cavity mode centre is located $\sim 15 \pm 4$ μm from the natural rf centre of the trap.

6.2 Cavity-assisted ion fluorescence

The information gathered in section 6.1 allows us to adjust the trap axis in order to overlap with the cavity mode to within 7 μm. We can fine-tune the cavity-ion coupling further by looking for photons generated in the cavity using a small alteration to the scheme outlined in section 2.3.4.

The altered scheme is shown in Fig. 6.11. The modification consists of adding a continuous, weak free-space repumper field, used to recycle the population from the $D_{3/2}$ state to the $S_{1/2}$ state after a single photon has been emitted by the atom. This creates a continous stream of cavity-assisted photon emissions at a rate R:

$$R = \rho_{33} \cdot \Gamma_{\mathrm{cav}}, \tag{6.11}$$

where ρ_{33} is the population of the excited state ($P_{1/2}$), and Γ_{cav} is equivalent to the rate

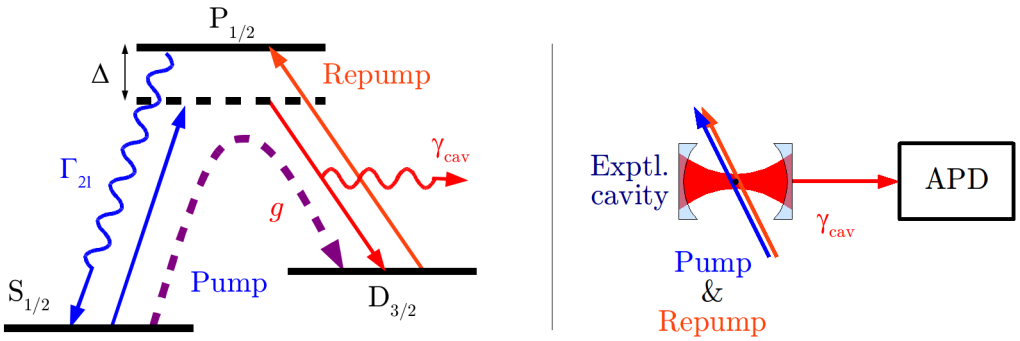

Figure 6.11: Continuous cavity photon generation scheme. A cavity-assisted Raman transition deposits a photon into the cavity mode, which then escapes to the detection setup. The continuous free-space repumper immediately recycles the population back to the $S_{1/2}$ state to begin the process again.

of spontaneous decay into the cavity mode [42]

$$\Gamma_{\text{cav}} = \frac{g^2}{\kappa} \cdot \frac{1}{1 + 2\left(\frac{\Delta}{\kappa}\right)^2}. \tag{6.12}$$

By coupling large numbers of cooled ions in a crystal to the cavity mode, we can multiply this cavity-photon emission rate and improve the signal-to-noise ratio to fine-tune the cavity ion coupling.

6.2.1 Single-photon counting avalanche photodiodes

The detector setup used to monitor cavity-photon emission is shown schematically in Fig. 6.12. The setup is arranged in the Hanbury Brown Twiss configuration [43] for later single-photon generation experiments.

Outside the vacuum chamber, at the output of the experimental cavity, a pair of 'mode-matching' lenses matches the focus, waist and curvature of the Gaussian cavity output mode to that of the single-mode optical fibre that guides photons to the detectors. This optimises the collection efficiency of the detector setup.

The photodetectors are a pair of Perkin-Elmer "photon counting module" Avalanche PhotoDiodes (APDs)with 25 Hz dark-count rate. 50 mm focal length lenses focus the output of cavity the coupled optical fibres onto the active surface of the photodiodes through a pair of notch filters with 10^{-4} extinction at 894 nm and 85 % transmission at 866 nm.

The cavity coupled fibres are aligned to the cavity by a two-stage process. First of all 866 nm light is coupled into the cavity in the reverse direction (from the APD end

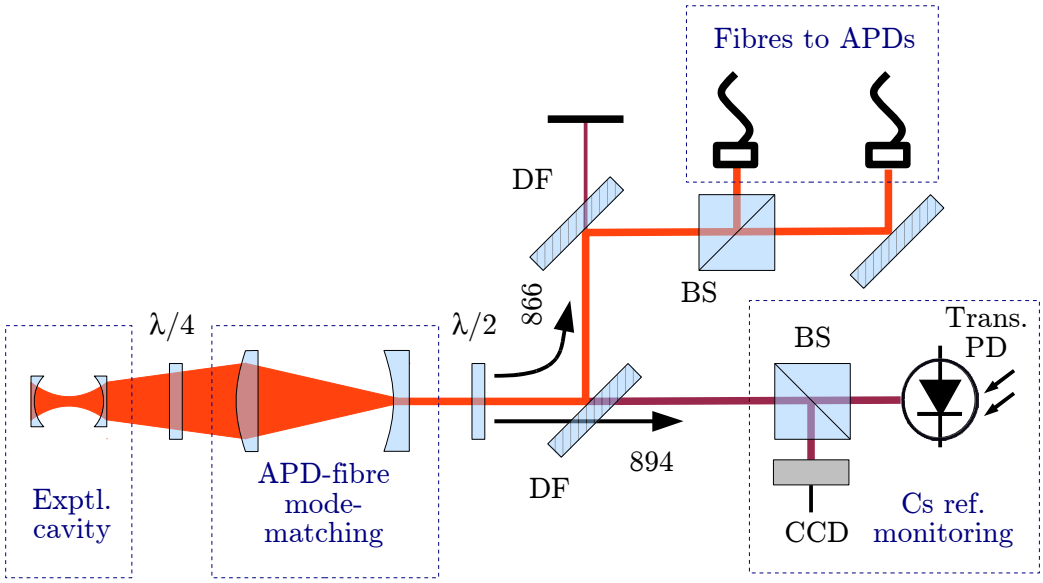

Figure 6.12: Cavity output optics. Mode-matching lenses on the right hand side match the outgoing 866 nm ion-cavity emission into two fibres coupled directly to a pair of avalanche photo-diodes (APDs). Light is coupled into this fibre via two long-pass dichroic filters (DF), which filter out 894 nm light coming from the PDH lock. The light filtered out is monitored by photo-diode and CCD camera. The beam splitter and two outputs are part of the Hanbury Brown Twiss configuration [43] that will be used to confirm single photon generation.

into the cavity). The coupling is optimised by monitoring the transmission intensity at the other side, using a flip mirror and photo-diode or CCD. Then, for fine-tuning, we can couple 866 nm light in from the input direction (via the 894 nm input fibre, Fig. 6.6), and scan over the resonance, monitoring and optimising the intensity at the output fibre on the APD end. We must be sure to couple to the TEM_{00} mode because it has the smallest mode volume and best overlap with the ions when they are centered on the cavity axis. Both of these properties result in a higher cavity-ion coupling (section 2.3.2). We can check which mode we are coupled to during the first stage of the process by replacing the transmission photodiode with a CCD camera.

The photodiode and CCD shown in the Fig. 6.12 are part of the cavity locking setup implemented later and explained in section 6.3.

6.2.2 Cavity-ion resonance detection

Using the scheme described above, a large cavity-ion resonance signal can be observed by the APDs when medium to large crystals are trapped.

Figure 6.13 shows the count rate at one of the APDs during this measurement. The

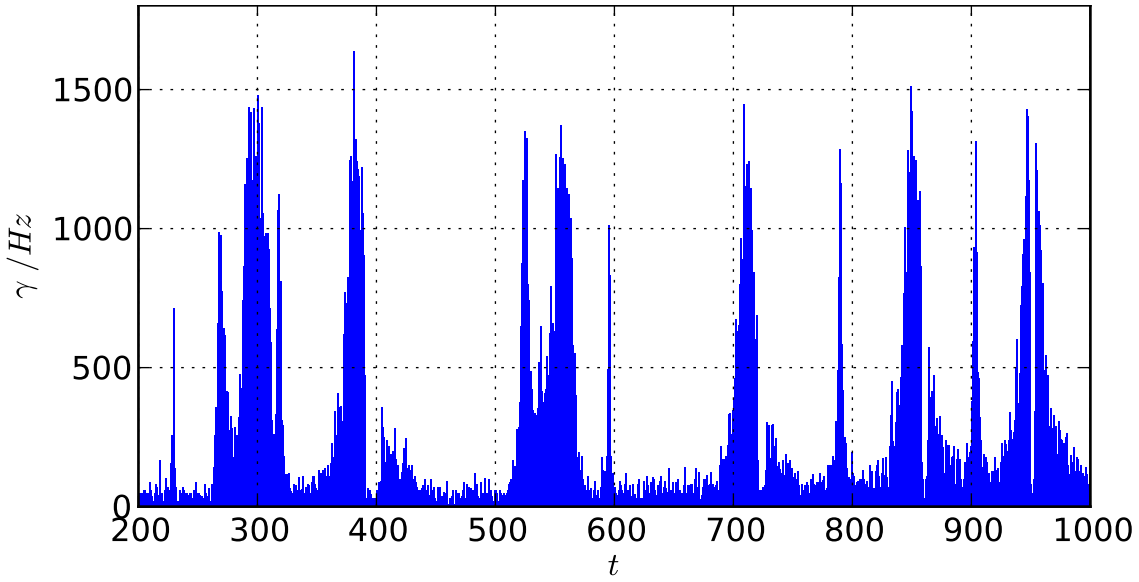

Figure 6.13: APD count rate γ measured whilst attempting to manually hold the cavity length at resonance with a large 397 nm pumped ion crystal. Thermal and acoustic fluctuations in the cavity length cause fluctuations in the APD rate as the cavity drifts in and out of resonance.

cavity is manually held around resonance with the Raman transition using the cavity-PZT control. Thermal and acoustic fluctuations in the cavity length cause the cavity to drift in and out of resonance, which is observed as sharp fluctuations in the APD count rate over time.

In order to distinguish cavity-resonance APD counts from stray photons being scattered off electrodes from the free-space repumper field, we can manually block and un-block the pump (397 nm) beam. With no pump beam, the ions decay into and remain in the ground state, and no more cavity fluorescence is possible. This effect is demonstrated in figures 6.14 & 6.15, which are close-ups of the trace shown in Fig. 6.13. The traces show peaks in fluorescence as the cavity drifts over resonance with the Raman transition. The peak profile is interrupted in places by sharp dips where the fluorescence drops to the background level as the pump beam is momentarily blocked by hand.

The fluorescence is differentiated from spontaneous emission from the ion into free space by noting the frequency difference Δ between the Raman resonance and the $P_{1/2} \rightarrow D_{3/2}$ transition. The frequency of the latter transition is identified by tuning the free-space repumping laser to the transition and then tuning the cavity to measure scatter from this laser into the mode. So long as Δ is larger than the cavity linewidth, the Raman resonant fluorescence will not be found at the same cavity length.

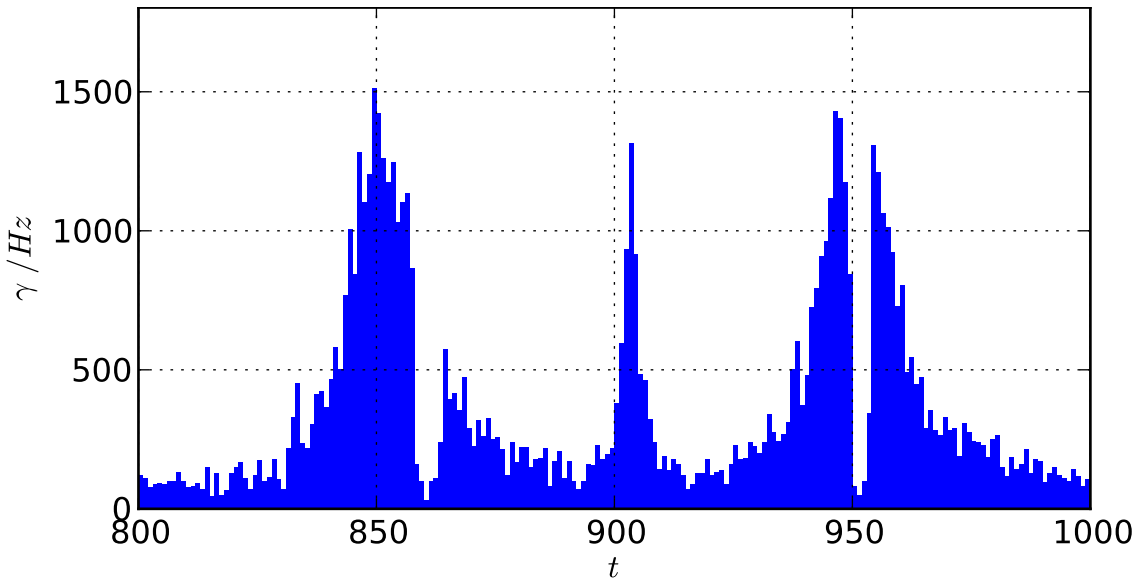

Figure 6.14: Close-up of a region in Fig. 6.13 where cavity-ion resonances are clearly seen. Notches in the first and third peak are caused by manually blocking the pump beam in order to confirm that this is a cavity-ion effect and not scatter from the free-space repumping field.

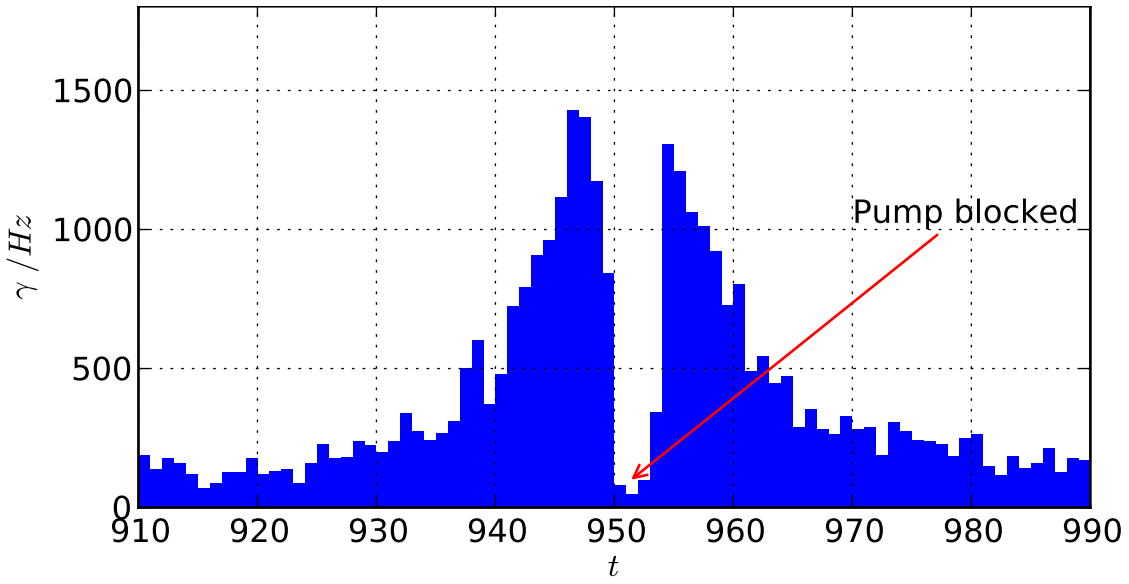

Figure 6.15: Close-up of the third resonance peak in Fig. 6.14, showing the sharp cavity fluorescence dip caused by pump blocking.

6.3 Experimental cavity lock

As the ion crystal used above is reduced in size the signal from the APDs drops sharply. This indicates that the trap and cavity axes are not quite optimally aligned. The thermal and acoustic fluctuations that cause the cavity to drift in and out of resonance make it difficult to fine-tune the cavity-ion coupling further. To suppress these fluctuations the experimental cavity length must be locked into resonance with the Raman transition so that the cavity fluorescence output will remain constant (for a given crystal position). Then the fluorescence can be optimised by moving the rf-centre of the trap into optimal overlap with the mode.

The experimental cavity length can be locked using the same PDH technique described in chapter 4. However, the cavity cannot be locked to a laser tuned directly to the Raman resonance since transmission light from the lock would reach the APDs and the signal from cavity-ion resonance would not be distinguishable from this background.

Instead, the cavity length must be locked to a frequency reference at a different wavelength. Transmission light from this laser can then be filtered out of the system using dichroic filters and 'notch' filters. The frequency reference chosen in this experiment is the atomic frequency reference laser described in chapter 4. The optical setup for the PDH lock is shown in Fig. 6.6 and the output filtering and monitoring setup is shown in Fig. 6.12.

For the experimental cavity lock, we cannot simply use the 10 MHz current modulation already on the laser, because this method of frequency modulation causes significant amplitude modulation of the laser output. This modulation generates an offset in the PDH error signal which is proportional to the signal amplitude detected by the PDH photodiode. This causes a problem for the experimental cavity lock because the laser-coupling optics for the system are decoupled from the trap and cavity by rubber feet that isolate the setup from acoustic vibration. Although this protects the cavity from acoustic fluctuations in its length, it leaves the cavity-laser coupling sensitive to vibrations of the coupling-optics. This acoustic noise in the cavity coupling causes fluctuations in the PDH error offset that cannot be compensated.

We work around this problem by applying modulation at 13 MHz with a fibre-coupled EOM; There is relatively small amplitude modulation associated with the electro-optic

modulation process. This means that the resulting offset is relatively small and its drift can be neglected.

On top of the lock modulation a second, higher frequency (50 MHz to 1 GHz) modulation is applied to the EOM, by combining the two modulation signals with a rf combiner. In order to maximise the first order sidebands associated with the second modulation, it is applied with a large modulation depth (+3 dBm compared to -7 dBm of the lock modulation). These sidebands still carry the PDH lock frequency modulation and so a PDH error signal can be generated when it is resonant with the cavity. Because the second modulation can be adjusted up to 1 GHz, this gives us a cavity lock with 1 GHz tuning range with respect to the base carrier frequency. This is essential for overlapping a longitudinal/transverse mode of the atomic reference with the TEM_{00} mode of the cavity Raman resonance (section 6.3.1).

The electronics for cavity locking are shown in Fig. 6.16. This setup follows along the same principle as that shown in Fig 4.5, and described in chapter 4. The input amplifier has been upgraded to an instrumental amplifier with very low output impedance and very high common-mode rejection ratio, for high fidelity and low noise amplification. The components used to provide signal offset have also been upgraded from voltage regulators to a voltage reference with very high voltage stability. This simplified PI feedback design was chosen over the PID shown in Fig. 4.3 because difficulties with acoustic noise and possible mechanical resonances make a low feedback-bandwidth system optimal for this setup, as long as acoustic and mechanical vibrations from the environment are minimised.

6.3.1 Cavity tuning

In order to find a resonance mode of the atomic reference laser which is within 1 GHz of the Raman resonance we can use an 866 nm laser tuned to a known two-photon resonance frequency. The two-photon resonance condition is equivalent to the Raman resonance condition, i.e. the repumper laser (or cavity) must be detuned from the repumping transition by the same Δ as the cooling laser. The exact repumper wavelength for a given detuning has been determined using cooling fluorescence spectroscopy in a separate trap, by Alex Wilson, Hiroki Takahashi and Andrew Riley-Watson. With the wavelength fixed, we couple the two-photon frequency laser into the cavity from the detector side using one of the APD fibres (Fig 6.12). We monitor the power reflected from the cavity by placing

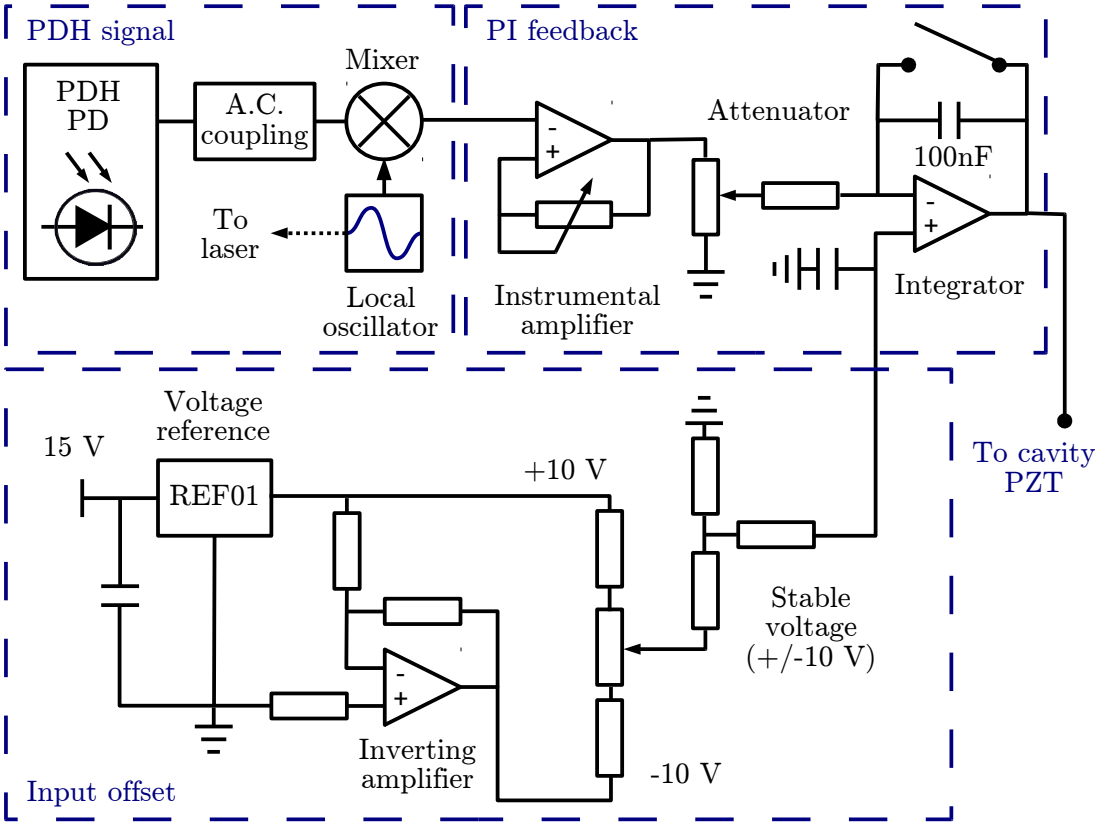

Figure 6.16: Experimental cavity PDH and feedback electronics. This system uses only low frequency integral feedback to avoid activation of mechanical resonances. A precision voltage reference provides a low-drift signal for PDH signal offset compensation.

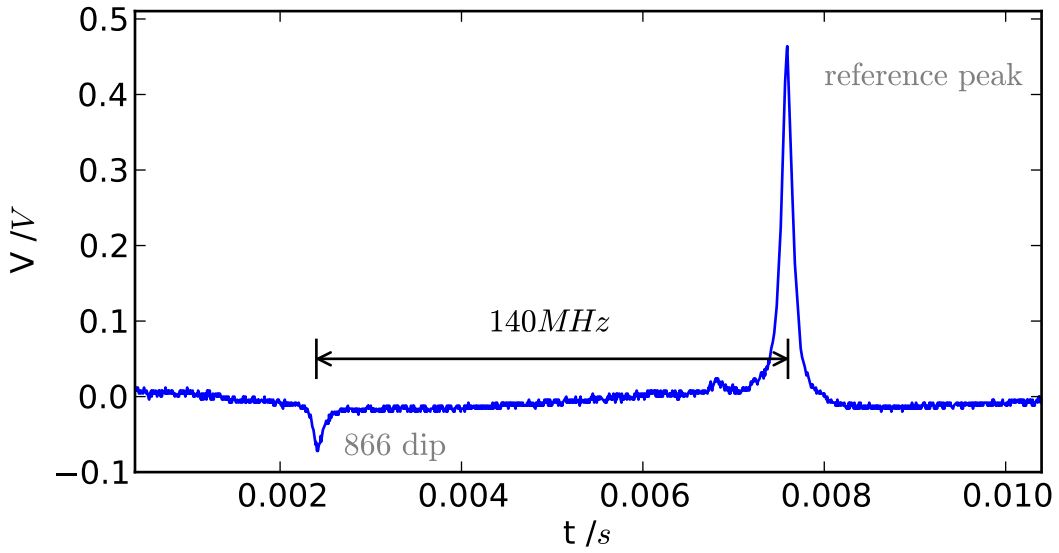

Figure 6.17: Overlapping the resonances of the reference locking laser and dark-resonance tuned 866 nm laser. The Cs reference peak shown is the carrier frequency (895 nm). Sidebands generated from this carrier can be tuned over 1 GHz.

a photodiode at the unused 50:50 beam splitter output. At the same time, we can couple the atomic reference laser to the cavity from the standard input direction. By rotating the polarisation of the 894 nm output using a half-waveplate, we can ensure that a significant portion of its intensity is reflected off the dichroic mirrors (rather than passed, as during normal operation of the lock), and into the monitored branch of the beam splitter output. From there we can look for a reference-laser mode transmission peak that overlaps within 1 GHz of the cavity-resonant reflection dip of the two-photon frequency laser (see Fig. 6.17).

Because the cavity is non-confocal, there are several well-spaced high order modes that can be to locked to. Our chances of overlapping the cavity with the resonance are further increased when we consider that we have several longitudinal modes to work with; The cavity PZTs scan over ∼50 V per FSR, and have 360 V total scan range – a total of seven free spectral ranges. As a bonus related to higher order modes, the transmission fields of these modes that get through to the output fibre, despite the dichroic filter, will be worse coupled to the APD fibre and will therefore give us a lower background photon count at the APDs.

In this trap-cavity setup the slightly non-degenerate TEM_{20} and TEM_{02} modes come closest to overlap with Raman resonance. The mode used to lock the cavity is a superposition of TEM_{20} and TEM_{02} modes (see Fig. 6.18), in between the latter two Gaussian

Figure 6.18: Cavity mode used for locking the cavity to overlap with the cavity-ion resonance (centre). Left and right Gaussian modes appear within 10 MHz of the centre mode.

modes, separated from each by 20 MHz. The superposed mode was chosen as the lock mode because it can be coupled with optimal suppression of the neighbouring Gaussian modes. Overlap with 866 nm laser tuned to the two-photon resonance is found by locking to the EOM-generated sideband of this mode at roughly 140 MHz in the direction of increasing voltage on the piezo controller, at a free spectral range that is roughly at the centre of the total scan range of both cavity-length PZTs.

The total background count when the cavity is locked is minimised by reducing the 894 power going into the cavity. The background count with 894 lock on is ∼25 Hz. This is sufficiently low to observe single photons at the expected rate of 1 kHz (based on the rate of the system developed by Keller et al. [23]).

Chapter 7

Conclusion

In this thesis, a co-linear trap-cavity system has been set up and succesfully tested, demonstrating that it is suitable for investigating atom-cavity interactions. Single ions can be trapped for at least an hour and long ion strings can trapped stably for minutes. Overlap with the cavity mode is within 7 μm of the centre. Cavity assisted photon emission has been demonstrated. This is a significant milestone towards single-photon generation and the implementation of the probabilistic entanglement scheme. The experimental optical cavity can be locked to resonance with the ion and pump laser, and laser systems with stability better than 100 kHz on time scales longer than 10 ms which are required for this scheme to have been set up.

The setup is very close to the stage where it is possible to generate single photons on demand. A few small experimental tasks remain.

Final optimisation of the ion-cavity overlap has to be achieved by locking the experimental cavity into Raman resonance with the pump laser, and maximising the rate of photons emitted from the cavity output mirror.

A particular sequence of repumping and cooling pulses must be applied to the ion in order to generate single photons using the scheme outlined in section 2.3.4. This is achieved using AOM switching of the two beams. The pulse sequence includes a cooling phase, during which the ions are fully exposed to cooling and repump lasers, followed by state preparation, where the cooling beam is switched off and the repumper prepares the ion in the ground state. Finally, a single photon generation pump pulse from the cooling laser generates the single photon.

A Hanbury Brown Twiss (HBT) [43] setup is already in place to confirm single-photon

production. The signals from the photon-counting APDs will be recorded by a time-to-digital converter, and the $g^2(\tau)$ correlation-function will be calculated from the data.

Once single-photon generation is confirmed, it's a relatively small step to produce single photons with a predetermined polarisation state. Magnetic field coils have been constructed and are ready for installation around the trap. With their help, the Zeeman sub-levels of the ion can be split, so that only photons with a certain polarisation are generated in a resonant process. Polarisation detection requires only that we replace the beam splitter in the HBT setup (Fig. 6.12) with a quarter-waveplate and polariser.

Strings of ions have already been trapped in this setup, so the probabilistic entanglement scheme only requires individual ion addressing to be implemented.

Bibliography

[1] D. Leibfried, E. Knill, S. Seidelin, J. Britton, R. B. Blakestad, J. Chiaverini, D. B. Hume, W. M. Itano, J. D. Jost, C. Langer, R. Ozeri, R. Reichle, and D. J. Wineland. Creation of a six-atom 'Schrödinger cat' state. *Nature*, 438:639–642, 2005.

[2] J. P. Home, M. J. McDonnell, D. M. Lucas, G. Imreh, B. C. Keitch, D. J. Szwer, N. R. Thomas, S. C. Webster, D. N. Stacey, and A. M. Steane. Deterministic entanglement and tomography of ionspin qubits. *New J. Phys.*, 8:188, 2006.

[3] M. J. McDonnell, J. P. Home, D. M. Lucas, G. Imreh, B. C. Keitch, D. J. Szwer, N. R. Thomas, S. C. Webster, D. N. Stacey, and A. M. Steane. Long-lived mesoscopic entanglement outside the Lamb-Dicke regime. *Phys. Rev. Lett.*, 98:063603, 2007.

[4] D. L. Moehring, P. Maunz, S. Olmschenk, K. C. Younge, D. N. Matsukevich, L.-M. Duan, and C. Monroe. Entanglement of single-atom quantum bits at a distance. *Nature*, 449:68–71, 2007.

[5] Wei-Bo Gao, Chao-Yang Lu, Xing-Can Yao, Ping Xu, Otfried Gühne, Alexander Goebel, Yu-Ao Chen, Cheng-Zhi Peng, Zeng-Bing Chen, and Jian-Wei Pan. Experimental demonstration of a hyper-entangled ten-qubit Schrödinger cat state. *Nature Phys.*, 6:331–335, 2010.

[6] T. Monz, P. Schindler, J. T. Barreiro, M. Chwalla, D. Nigg, W. A. Coish, M. Harlander, W. Hänsel, M. Hennrich, and R. Blatt. 14-qubit entanglement: Creation and coherence. *Phys. Rev. Lett.*, 106:130506, 2011.

[7] M. Riebe, K. Kim, P. Schindler, T. Monz, P. O. Schmidt, T. K. Koerber, W. Hänsel, H. Häffner, C. F. Roos, and R. Blatt. Process tomography of ion trap quantum gates. *Phys. Rev. Lett.*, 97:220407, 2006.

[8] T. Monz, K. Kim, A. S. Villar, P. Schindler, M. Chwalla, M. Riebe, C. F. Roos, H. Häffner, W. Hänsel, M. Hennrich, and R. Blatt. Realization of universal ion-trap quantum computation with decoherence-free qubits. *Phys. Rev. Lett.*, 103:200503, 2009.

[9] P. Schindler, J. T. Barreiro, T. Monz, V. Nebendahl, D.Nigg, M. Chwalla, M.Hennrich, and R. Blatt. Experimental repetitive quantum error correction. *Science*, 332:1059–1061, 2011.

[10] J. Chiaverini, D. Leibfried, T. Schaetz, M. D. Barrett, R. B. Blakestad, J. Britton, W. M. Itano, J. D. Jost, E. Knill, C. Langer, R. Ozeri, and D. J. Wineland. Realization of quantum error correction. *Nature*, 432:602–605, 2004.

[11] D. P. DiVincenzo. The physical implementation of quantum computation. *Fortschr. Phys.*, 48:771–783, 2000.

[12] A. Kuhn, M. Hennrich, and G. Rempe. Deterministic single-photon source for distributed quantum networking. *Phys. Rev. Lett.*, 89:067901, 2002.

[13] J. McKeever, A. Boca, A. D. Boozer, R. Miller, J. R. Buck, A. Kuzmich, and H. J. Kimble. Deterministic generation of single photons from one atom trapped in a cavity. *Science*, 303:1992–1994, 2004.

[14] P. F. Herskind, A. Dantan, J. P. Marler, M. Albert, and M. Drewsen. Realization of collective strong coupling with ion coulomb crystals in an optical cavity. *Nat. Phys.*, 6:494–498, 2009.

[15] L.-M. Duan and H. J. Kimble. Efficient engineering of multiatom entanglement through single-photon detections. *Phys. Rev. Lett.*, 90:253601, 2003.

[16] D. E. Browne and T. Rudolph. Efficient engineering of multiatom entanglement through single-photon detections. *Phys. Rev. Lett.*, 90:253601, 2003.

[17] R. Raussendorf and H. J. Briegel. A one-way quantum computer. *Phys. Rev. Lett.*, 86:5188, 2001.

[18] A. Mortensen. *Aspects of Ion Coulomb Crystal based Quantum Memory for Light.* PhD thesis, 2005.

[19] F. L. Kien and K. Hakuta. Density operator and applications in nonlinear optics, 2004. Lecture course.

[20] H. Kogelnik and T. Li. Laser beams and resonators. *Appl. Opt.*, 5:1550–1567, 1966.

[21] A. Kuhn and D. Ljunggren. Cavity-based single-photon sources. *Contemporary Physics*, 51:289–313, 2010.

[22] C. K. Law and H. J. Kimble. Deterministic generation of a bit-stream of single-photon pulses. *Journal of Modern Optics*, 44:11-12:2067–2074, 1997.

[23] M. Keller, B. Lange, K. Hayasaka, W. Lange, and H. Walther. Continuous generation of single photons with controlled waveform in an ion-trap cavity system. *Nature*, 431:1075, 2004.

[24] P. F. Herskind, A. Dantan, M. Alber, J. P. Marler, and M. Drewsen. Positioning of the rf potential minimum line of a linear paul trap with micrometer precision. *J. Phys. B: At. Mol. Opt. Phys*, 42:154008, 2009.

[25] K. Dholakia, G. Zs. K. Horvath, D. M. Segal, and R. C. Thompson. Photon-correlation detection of ion-oscillation frequencies in quadrupole ion traps. *Phys. Rev. A*, 47:441–448, 1993.

[26] C. J. Hawthorn, K. P. Weber, and R. E. Scholten. Littrow configuration tunable external cavity diode laser with fixed direction output beam. *Rev. Sci. Instrum.*, 72:4477–4479, 2001.

[27] R. W. P. Drever, J. L. Hall, F. V. Kowalski, J. Hough, G. M. Ford, A. J. Munley, and H. Ward. ˙ *Appl. Phys. B: Photophys. Laser Chem.*, 31:97, 1983.

[28] M. Zhu and J.L. Hall. ˙ *J. Opt. Soc. Am. B*, 10:802, 1993.

[29] C. Salomon, D. Hils, and J. L. Hall. ˙ *J. Opt. Soc. Am. B*, 5:1576, 1988.

[30] C. P. Pearman, C. S. Adams, S. G. Cox, P. F. Griffin, D. A. Smith, and I. G. Hughes. Polarization spectroscopy of a closed atomic transition: applications to laser frequency locking. *J. Phys. B: At. Mol. Opt. Phys*, 35:5141–5151, 2002.

[31] N. Seymour-Smith, P. Blythe, M. Keller, and W. Lange. Fast scanning cavity offset lock for laser frequency drift stabilization. *Rev. Sci. Instrum.*, 81:075109, 2010.

[32] S. M. Jaffe, M. Rochon, and W. M. Yen. Increasing the stability of single-frequency lasers. *Rev. Sci. Instrum.*, 64:2475, 1993.

[33] W. Z. Zhao, J. E. Simsarian, L. A. Orozco, and G. D. Sprouse. A computer-based digital feedback control of frequency drift of multiple lasers. *Rev. Sci. Instrum.*, 69:3737, 1998.

[34] K. Matsubara, S. Uetake, H. Ito, K. Hayasaka Y. Li, and M. Hosokawa. Precise frequency-drift measurement of extended-cavity diode laser stabilized with scanning transfer cavity. *Jpn. J. Appl. Phys.*, 44:229, 2005.

[35] A. A. Tonyushkin, A. D. Light, and M. D. Di Rosa. Phase-locked scanning interferometer for frequency stabilization of multiple lasers. *Rev. Sci. Instrum.*, 78:123103, 2007.

[36] J. H. T. Burke, O. Garcia, J. K. Hughes, B. Livedalen, and C. A. Sackett. Compact implementation of a scanning transfer cavity lock. *Rev. Sci. Instrum.*, 76:116105, 2005.

[37] Model MSO6054A.

[38] Model 3562A Dynamic signal analyser in swept-sine modulation frequency response mode.

[39] D.B. Sullivan, D.W. Allan, D.A. Howe, and F.L. Walls. Characterization of clocks and oscillators. *NIST Tech Note 1337 (BIN: 868)*, 1990.

[40] S. Uetake, K. Matsubara, H. Ito, K. Hayasaka, and M. Hosokawa. Frequency stability measurement of a transfer-cavity-stabilized diode laser by using an optical frequency comb. *Appl. Phys. B*, 97:413, 2009.

[41] G. Janik, W. Nagourney, and H. Dehmelt. Doppler-free optical spectroscopy on the Ba+ mono-ion oscillator. *J. Opt. Soc. Am. B*, 2:1251, 1985.

[42] P. Meystre and M. Sargent. *Elements of quantum optics*. Springer, 1999.

[43] H. Kimble, M. Dagenais, and L. Mandel. Photon antibunching in resonance fluorescence. *Phys. Rev. Lett.*, 39:691.